Physics-based Simulations of Large Earthquake Rupture Processes

by

Marlon D. Ramos

A dissertation submitted in partial fulfillment
of the requirements for the degree of
Doctor of Philosophy
(Earth and Environmental Sciences)
in the University of Michigan
2021

Doctoral Committee:

Assistant Professor Yihe Huang, Chair
Associate Professor Jeremy Bassis
Associate Professor Eric Hetland
Professor Jeroen Ritsema
Professor Ben van der Pluijm

Marlon D. Ramos
ramosmd@umich.edu
ORCID ID: 0000-0003-4449-8624

ACKNOWLEDGMENTS

My path leading up to the PhD has been fraught with unexpected twists, turns, and setbacks. Looking back I realize this work is not only the culmination of nearly a decade of formal academic training, but it is reflective of a larger, collective effort from my friends, colleagues, family and luck. First and foremost I express my sincere gratitude to my doctoral research mentor, Yihe Huang. Her guidance, patience, and seismological knowledge encouraged me to deliver my best and also showed me how to approach science carefully. I also extend my thanks to Professors Eric Hetland, Jeroen Ritsema, Ben van der Pluijm, Jeremy Bassis, Larry Ruff, Naomi Levin, Marin Clark, and Nathan Niemi for serving on my committee or having taught me something during my time at Michigan. Also, my growth as a dynamic rupture modeler would not have been nearly as impressive without the expertise and patience from Alice-Agnes Gabriel, Duo Li and Thomas Ulrich at LMU München. I am grateful for the years of help from Anne Hudon, Paula Frank and Mike Messina. I am indebted to the support from my partner João, STR, my cohort (Prithvi T., Maria A., Elizabeth C., Sooyeon K., Molly R., Brie, Guolei H.), my dog (Chippy/Buddy B.), and an abridged list of rockstars in the EARTH department including Ross M., Sam H., Juliana M., Meichen L., Meredith C., Jing-Ci, Amir S., Kirk T., Billy M., Nik M., Olivia H., Mark R., Meg V., Phoebe A. and my GSM-team (Becca D. and Madelyn C.). This research was enabled by a National Science Foundation PREEVENTS grant (No. 1663769) awarded to Yihe Huang and support from the Rackham Merit Fellowship.

TABLE OF CONTENTS

Acknowledgments . . . . . **ii**

List of Figures . . . . . **v**

Abstract . . . . . **x**

Chapter

I Introduction **1**

1.0.1 Modeling the Earthquake Rupture Process 1
1.0.2 Research objectives 2
1.0.3 Outline 4

II How the transition region along the Cascadia megathrust influences coseismic behavior: Insights from 2-D dynamic rupture simulations **6**

2.1 Introduction 6
2.2 Methodology 8
2.2.1 Model Geometry and Friction Law 8
2.2.2 Constraints on Cascadia Megathrust Stress Conditions 9
2.2.3 Hypocenter Locations and Nucleation Procedure 10
2.3 Results 11
2.3.1 Northern Cascadia Simulations 11
2.3.2 Southern Cascadia Simulations 12
2.4 Discussion and Conclusions 13
2.5 Figures - Chapter 2 16

III Assessing Margin-Wide Rupture Behaviors along the Cascadia Megathrust with 3-D Dynamic Rupture Simulations **19**

3.1 Introduction 20
3.1.1 Geological and Geophysical Inferences on the State of Megathrust Segmentation 20
3.1.2 Cascadia Earthquake Source Models 21
3.2 Methodology 23
3.2.1 Constraining Dynamic Rupture with Geodetic Coupling Models . 24
3.2.2 Material Properties and Fault Strength 24
3.2.3 Fault friction law 25
3.2.4 Rupture Initiation 26
3.3 Results 27

3.3.1 Translating 2-D rupture simulations to 3-D . . . 27
3.3.2 Uniform Gaussian and Gamma coupling models . . . 28
3.3.3 Segmented Gaussian and Gamma coupling models . . . 28
3.3.4 Effect of up-dip frictional behavior . . . 30
3.3.5 Effect of down-dip locking depth . . . 30
3.3.6 Fitting 1700 A.D. subsidence measurements . . . 31
3.4 Discussion . . . 32
3.4.1 What allows large earthquakes to develop along the Cascadia megathrust? . . . 32
3.4.2 Explaining 1700 A.D. subsidence patterns with Dynamic Rupture Simulations . . . 33
3.4.3 The Potential of Heterogeneous Down-dip Frictional Properties . 34
3.4.4 Limitations and Future Directions . . . 34
3.5 Conclusions . . . 35
3.6 Figures - Chapter 3 . . . 37

IV Stress Changes on the Garlock Fault during and after the 2019 Ridgecrest Sequence . . . 52

4.1 Introduction . . . 53
4.2 Methodology . . . 54
4.2.1 Kinematic slip inversion . . . 54
4.2.2 Static model: Coulomb stress change . . . 55
4.2.3 Dynamic model: Initial conditions and constraints . . . 55
4.3 Results . . . 57
4.3.1 Kinematic slip inversion . . . 57
4.3.2 Static stress change . . . 58
4.3.3 Dynamic earthquake rupture model . . . 59
4.3.4 Temporal stress changes on the Garlock fault . . . 60
4.4 Discussion and Conclusion . . . 61
4.5 Figures - Chapter 4 . . . 66

V Conclusions . . . 75

5.0.1 Future Research Directions . . . 76

Bibliography . . . 79

LIST OF FIGURES

2.1 The Cascadia subduction zone. (a) Map of nonvolcanic tremor (normalized) density along the Cascadia megathrust from 2009 to 2018. Plate interface depths are given by the bold black lines in 10 km intervals. Major continental and oceanic are denoted as NA, PA, JdF, and Gorda. (b) 2-D rupture model setup across northern Cascadia showing the locked (solid teal line), gap (dashed black line), and ETS (solid red line) megathrust regions. (c) 2-D rupture model setup across southern Cascadia. (d) Schematic drawing of the two downdip rupture scenarios that highlight how if rupture can penetrate into the gap, seismic waves are brought closer to populated areas, extending the length of the earthquake source model. ETS = episodic tremor and slow-slip; NA = North America; PA = Pacific; JdF = Juan de Fuca. 16

2.2 Dynamic rupture simulations for northern and southern Cascadia. The heavy dashed black lines partition the fault into the locked, gap, and ETS regions. Alongdip stresses, S-ratio, and resulting spatiotemporal rupture histories are shown for each model. (a) Northern Cascadia model assuming an initial shear stress asperity at the base ofthe locked region of the fault, a negative shear stress rate amplitude of $\sim$2.5 kPa/year in the gap, and the entire fault is assumed slip-weakening. (b) A northern Cascadia model assuming a dynamic friction coefficient level of 0.6 and an approximately $\sim$2.5 kPa/year shear stress rate in the gap. This model generates multiple downdip supershear daughter-cracks (white dotted lines). (c) Southern Cascadia model incorporating heterogeneous τ_o and σ_n perturbations to represent a rougher fault. ETS = episodic tremor and slow-slip. 17

2.3 Final along-fault slip distributions for all rupture models and the effect of downdip supershear on synthetic waveforms. "No-fsr" models have the free-surface reflection suppressed by assuming slip-neutral friction in the upper 5 km of the fault. (a) Coseismic slip for northern Cascadia rupture models where the light blue and red regions signify the locked and ETS regions of the fault, respectively. The gap region is left unshaded. (b) Coseismic slip for southern Cascadia models. (c) Horizontal (top) and vertical (bottom) component seismograms for a station located at x = 120 km, immediately above the downdip edge of the modeled northern Cascadia megathrust. The wave pulses resulting from supershear rupture are indicated. 18

3.1 Cascadia subduction zone study area. A) Megathrust segmentation (segments are separated by red lines) suggested from offshore turbidite deposits with corresponding estimated segment recurrence intervals in years. Primary morphotectonic regions are superposed (blue dashed lines). B) Gaussian and C) Gamma coupling models projected onto the Slab2 megathrust geometry. The Gaussian coupling model assumes interseismic creep at shallow megathrust depths whereas the Gamma model assumes high strain accumulation. The inferred region of the creeping segment is denoted by a yellow box. Magenta stars denote rupture initiation locations in our dynamic rupture models. Thick white lines are megathrust depth contours (kilometers). JdF = Juan de Fuca plate. 37
3.2 Material properties, stress, and frictional conditions for dynamic rupture simulations. A) Smoothed 1-D CVM velocity model for Cascadia [**?**]]Stephenson2017. B) Effective normal stress. C) Dynamic and static frictional coefficients with depth. D) Frictional cohesion for the Gaussian and Gamma coupling models. . 38
3.3 Dynamic rupture simulation results when stress and strength conditions from Ramos & Huang (2019) are extrapolated along-strike. A) Along-strike dynamic stress-drop and epicenter location. B) Final megathrust slip-distribution and moment-magnitude. The black dashed lines indicate the 10 and 20 km depth contours to highlight the extent of down-dip rupture. C) Coseismic uplift (red) and subsidence (blue) along the Cascadia margin. Squares signify the coastline whereas the triangles denote the deformation front. D) Model predicted (black squares; same as panel as C) and paleoseismic observations of estimated subsidence during the 1700 A.D. rupture. 39
3.4 Slip at the deformation front for smooth model presented in Figure 3. 40
3.5 Snapshots of the rupture-front velocity at certain times. The downdip rupture front is due to dynamic wave triggering and from up-dip. This feature is possible because of the incredibly low fault strength in the ETS region (0.6 MPa and 0.1 MPa for the static and dynamic strengths, respectively). 41
3.6 Comparison between Gaussian and Gamma dynamic stress-drop distributions and the resultant subsidence patterns assuming the maximum strain accumulation time (T) of 320 years (i.e., time since the last great earthquake in 1700 A.D.) A) Dynamic stress-drop distribution for the Gaussian coupling model. B) Dynamic stress-drop distribution for the Gamma coupling model. Both ruptures are nucleated in northern Cascadia (magenta star). C) model predicted subsidence along the coastline compared to 1700 A.D. measurements. 42
3.7 Example along-dip shear stress gradients between smooth and coupling models (left) and typical subsidence amplitudes predicted for each stress gradient (right). Distance is measured from the deformation-front and the location of the coastline is shown for reference. 43

3.8 Gaussian and Gamma dynamic rupture simulations nucleated in northern or southern Cascadia (colored star). In each plot, the line length corresponds to the along-strike rupture extent. The line style corresponds to the variable segment location. A) Gaussian ruptures where the width of the central segment (also contains the nucleation asperity) is varied until margin-wide slip no longer occurs. The T levels (relative dynamic stress-drop) remains constant for each simulation. B) Same idea as A but for Gamma rupture simulations. The higher stress-drop at shallower depths provides enough energy for ruptures to easily span the entire Cascadia margin. Moment-magnitude is plotted along the x-axis on all plots. C) and D) show Gaussian and Gamma ruptures nucleated in southern Cascadia, respectively. For each subfigure, the Northern (N), central (C), or southern (S) segment regions are denoted. 44
3.9 Slow rupture speed of Gamma models. A) Snapshots of the slip-rate at 25 second increments. Black box denotes zoom-in shown in B. B) Rupture velocity at the last two time steps to show how the rupture can dramatically slow down in the central Cascadia region. 45
3.10 Gaussian coupling models with variable sediment frictional behavior in the upper 5 km of the megathrust. A) Along-strike rupture lengths (colored lines) as function of dynamic friction coefficient. B) Slip at the deformation-front for each scenario shown in A. 46
3.11 Effect of down-dip locking depth on coseismic slip distribution and uplift/subsidence patterns. A) Final slip distributions for the Gaussian coupling model nucleated in northern Cascadia. The earthquake is nucleated at the red star and a profile of uplift/subsidence at the free-surface is plotted in figure B (black line through red star). In each panel, the locking depth is systematically deepened by 2 km. B) Model-predicted coseismic subsidence and uplift for the range of locking depths studied. The coastline is plotted for reference near 250 km from the deformation front. Each solid line represents the coseismic hingeline and is colored by its respective locking depth. We also show a shallower locking depth (15 km) in yellow to illustrate how such an assumption changes the amplitude and gradient of coseismic deformation. 47
3.12 Gaussian and Gamma coupling models with shallow locking depth (15 km) that match coastal 1700 A.D. subsidence measurements to first order. A) Ruptures nucleated in northern Cascadia. B) Ruptures nucleated in southern Cascadia. C) comparison of predicted coastal subsidence from simulations shown in A and B. 48
3.13 Deeper locking depth (20 km) alternative to fitting 1700 A.D. subsidence. A) Gamma coupling model dynamic stress-drop distribution. B) Final slip distribution. C) Predicted uplift and subsidence. D) Along-strike subsidence comparison between modeled (black) and 1700 A.D. observations (blue). . . . 49

3.14 Comparison between dynamic rupture simulations with and without high dynamic stress-drop subevents positioned near the down-dip edge of locking ($\sim$15 km) along-strike. A) Gaussian dynamic stress-drop distribution without subevents. White triangle denotes synthetic seismogram receiver. B) Gaussian dynamic stress-drop distribution with superposed $\sim$15 – 20 MPa subevents. C) Coastal subsidence for both models with 1700 A.D. observations for comparison. D), F), and E) show the raw spectral amplitudes of the x-, y-, and z-components, respectively. The influence of the subevents is to increase the high-frequency amplitudes recorded (bold colored lines). D) and E) show (normalized) synthetic seismograms near the epicenter for dynamic rupture models excluding and including high stress-drop subevents. 50
3.15 Effect of heterogeneous Dc at some seiesmic stations along the coast. 51

4.1 2019 Ridgecrest earthquake sequence. (a) Study area with foreshock and mainshock fault planes denoted by solid lines. The approximate region of the central Garlock fault that experienced creep during this sequence is indicated by the box. (b) Mainshock slip-inversion results in which we determine a hypocenter depth of 3 km and a peak slip amplitude of 4.7 m that is immediately northwest (NW) of the hypocenter. (c) Foreshock slip-inversion results. Foreshock planes parallel and perpendicular to the mainshock fault plane are denoted as plane 1 and plane 2, respectively. Note that an NW–southeast (SE) fault orientation is the same for the mainshock and foreshock fault planes. Stars indicate (a) epicenter or (b,c) hypocenter locations. 66
4.2 Coulomb stress change (ΔCFS) due to foreshock planes 1 and 2 on the mainshock fault plane calculated at a depth of 5 km and with a friction coefficient of 0.6. (a) The combined effect of both aftershock fault plane slip on the mainshock. (b) The ΔCFS from plane 1, which is parallel to the main fault plane. (c) ΔCFS from plane 2, which is the northeast–southwest-striking cross fault. The aftershocks depicted are the earthquakes that occurred after the foreshock and do not include those induced from mainshock stress changes. GF, Garlock fault. 67
4.3 ΔCFS of the mainshock on a receiver fault of 70° strike and 90° dip, approximating the leftmost part of the Garlock fault in this figure. (Top) ΔCFS results for a 5 km depth source at friction coefficients of (left to right) 0.2, 0.4, and 0.6. (Bottom) ΔCFS results for a 10 km depth source with the same friction coefficients. 68
4.4 (a) Static stress drop and (b) initial shear stress along the mainshock fault plane. Static stress drop is calculated assuming a homogeneous Poisson medium and initial shear stress is computed using the complete stress-drop assumption. We select an initial shear stress profile through the main asperity at 3 km depth (dashed line) for our 2D dynamic rupture models. 69

4.5 (a) Along-fault slip distribution resolved by the kinematic slip inversion (solid line) and that calculated from the dynamic rupture model (dashed line). The x-axis measures distance from where the earthquake is nucleated in our model. (b) Dynamic stress drop along the fault. Location shown in Figure 4. (c) Spatiotemporal and bilateral rupture history predicted by the dynamic rupture model. Solid lines signify average rupture-front speed. Both rupture fronts propagate at sub-Rayleigh wavespeed. 70
4.6 Static stress-change field in the modeling domain rotated to the strike of the Garlock fault. (a) Normal stress and (b) shear stress. Garlock fault trace (dashed line) and Ridgecrest mainshock fault (solid line) are superimposed onto the figure. Box denotes approximate location of the creeping region. Inset study area map gives stress- change spatial orientation for Figures 6–8. . . . 71
4.7 Normal stress changes (σ_{yy}) at various moments in time on the central Garlock fault during coseismic rupture of the mainshock. A point on the Garlock is selected to visualize the stress amplitude variability (solid circle). (a–e) represent σ_{yy} from 17.5 to 50 s during rupture propagation. (f) The time history of yy in which (a–e) the blue squares denote the amplitude change at each of the normal stress snapshots. 72
4.8 Similar to Figure 9, but shear stress changes (σ_{xy}) during coseismic rupture. (a–e) σ_{xy} from 17.5 to 50 s during rupture propagation. (f) The time history of σ_{xy} showing three distinct peaks in stress change on the Garlock fault at $\sim$28, 38, and 50 s. 73
4.9 Stress-change evolution on a section of the Garlock fault during the entire Ridgecrest earthquake simulation. (a) Normal (σ_{yy}) and shear (σ_{xy}) stress change. (b) Temporal ΔCFS for friction coefficient levels assessed in the static stress-change analysis. Note that we plot the temporal stress change starting at 10 s because this is when the artificial nucleation procedure ceases. 74

ABSTRACT

A complete description of how an earthquake occurs can be achieved with a physically self-consistent modeling framework where wave propagation is combined with fracture mechanics to simulate the initiation, growth, and arrest of fault motion. To this end, dynamic rupture simulations are used to reproduce or predict dynamic and static deformations through time and space and give insight into the frequency-dependent rupture process. This dissertation assessed the rupture dynamics of large earthquakes in two separate tectonic environments using two different approaches. The major contribution of this work is the use of high-resolution geophysical data to constrain rupture dynamics and uncover controls on future seismic hazard in subduction or strike-slip fault systems.

In chapter 2 I developed 2-D dynamic rupture simulations focused on the transition zone region between the locked and creeping regions of the Cascadia megathrust. I used geodetic inversions for shear stress-rate to constrain possible dynamic stress-drop amplitudes within the locked and transition regions. While the initial conditions suggested an energetically unfavorable condition for deeper rupture, my models captured the exact opposite. Deeper rupture at speeds exceeding the shear-wave velocity (supershear) is possible given the geodetic inversion results, unless the transition region has a dynamic frictional behavior that strongly increases in response to slip. This study suggested the possibility of a wider Cascadia earthquake source model and that one possible mechanism for high-frequency energy radiation down-dip might be when the there is a supershear rupture transition.

In chapter 3 I extended the 2-D simulation framework and developed the first fully dynamic 3-D rupture simulations for the Cascadia subduction zone. I developed an approach to estimate dynamic stress-drop along the Cascadia megathrust using geodetic coupling models of slip-rate deficit. I found that the relative dynamic stress-drop amplitude in the

central Cascadia region exerts the greatest influence on whether or not margin-wide ruptures can develop. I also showed several non-unique simulations that can provide a close match to subsidence data from the last Cascadia megathrust event in 1700 A.D. - underscoring the importance of offshore geodetic data to rule out competing ideas of interseismic strain accumulation offshore.

Finally, chapter 4 investigated elastic stresses radiated from the 2019 Ridgecrest Sequence mainshock using 2-D dynamic rupture simulations. I focused on the dynamic stress changes experienced by the Garlock fault, a major strike-slip fault in the Eastern California Shear zone, during the coseismic rupture phase. I found that peak Coulomb stresses arrive at the Garlock $<$ 1 minute from the mainshock nucleation. The simulations resolved key kinematic rupture parameters such as low mainshock rupture speeds ($\leq$ 2.0 km/s) and slip amplitudes through the hypocenter.

CHAPTER I

Introduction

Earthquakes represent immense tectonic stress release occurring near regions of weakness in the Earth's crust and mantle (faults). As slip develops on a fault, elastic seismic waves are radiated and can be modulated in response to stress and strength on the fault, or as they pass through different geological materials. Seismic, geodetic, and geologic observations before, during, and after earthquake rupture have increased our understanding of how they evolve in space and time. But modern geophysical observations are limited to the last ~60 years and high-resolution, broadband instrument recordings are especially lacking for large ruptures before 1980 (*Bilek and Lay*, 2018) and offshore (*Wang and Tréhu*, 2016). A crucial question for seismic hazards analysis is then how to best estimate the seismic source area before an event occurs? If we cannot predict when a great earthquake will occur, can we use numerical tools to assess how it could occur, given sufficient information (or reasonable assumptions) on the state of fault stress and friction? How can different datasets be harnessed to inform physics-based simulation of the earthquake rupture process?

1.0.1 Modeling the Earthquake Rupture Process

There are two ways to model an earthquake. The first is the kinematic approach, whereby displacements at the source are prescribed a-priori and parameters controlling rupture propagation (e.g., rise-time, rupture speed, slip) are likewise assigned across a discretized fault surface (*Hartzell and Heaton*, 1983). Kinematic rupture models are commonplace due to the straightforward relationship between fault slip and the recorded elastic displacement field once the Green's functions are known, allowing these types of models to be run at lower computational cost. In contrast, the second approach describes the earthquake rupture process dynamically, accounting for the initiation, propagation, and arrest of fault motion in response to stress conditions and a constitutive friction law (*Madariaga, R. and Olsen*, 2002). Specifying the fault stress (normal and shear) as well as friction levels (static and dynamic) requires constraints from coseismic observation or laboratory experiment,

which is why some dynamic rupture simulations come after kinematic source observations to gain insight into the first order physics.

To initialize the tectonic shear stress on the fault, one can estimate the stress drop from a kinematic slip inversion (e.g., *Ripperger and Mai*, 2004), or if the orientation of the maximum compressive stress field is well constrained, the initial shear stress tensor may be calculated assuming an Andersonian state of stress (e.g., *Aochi, Hideo, Madariaga*, 2003; *Ulrich et al.*, 2019). The selection of realistic static and dynamic friction levels on the fault are key ingredients of the constitutive fault friction law that will ultimately control slip (namely, slip-weakening or rate-and-state friction laws). Physically permissible fault friction laws allow for a nonsingular relation between the static and dynamic friction near the rupture tip (*Ida*, 1972; *Palmer*, 1973). In slip-weakening or fast velocity-weakening friction laws, typical values of the static friction range from 0.6 - 0.4 whereas dynamic friction can be ≤ 0.1 if exceptional weakening occurs (e.g., *Andrews*, 1976; *Byerlee*, 1978; *Cochard, A., Madariaga*, 1996; *Daub and Carlson*, 2010; *Di Toro et al.*, 2011; *Reches and Lockner*, 2010).

Advances in computational infrastructure have made high-resolution forward modeling of the earthquake process feasible and allow one to understand what might be causing specific rupture characteristics (e.g., slip distribution, rupture speed and length, crack or pulse-like propagation style). For subduction zones in which there are no modern geophysical recordings of earthquake rupture (i.e., Cascadia), geodetic coupling models (e.g., *Burgette et al.*, 2009; *Li et al.*, 2018; *Schmalzle et al.*, 2014) can be used to constrain dynamic rupture simulations. Using geodetic coupling models to reproduce fault slip estimates from observation or inform future earthquake scenarios is beginning to be explored (e.g., *Yang et al.*, 2019a; *Yao and Yang*, 2020).

1.0.2 Research objectives

The primary objective of this work is to use dynamic rupture simulations to predict final rupture extent or stress changes and consequently, inform earthquake hazard analysis. Two separate tectonic environments are studied: the Cascadia subduction zone and the Eastern California shear zone. Despite the stark contrast in geologic history and available datasets in these regions, dynamic rupture simulations are developed to test end-member hypotheses of interseismic strain accumulation (i.e., Cascadia), or to explain first-order kinematic rupture features and resolve dynamic stresses on a nearby major fault system (i.e., 2019 Ridgecrest Sequence). The numerical methods used include the spectral element method and the Discontinuous-Galerkin method, a high-order finite element method (*Ampuero*,

2009; *De La Puente et al.*, 2009; *Pelties et al.*, 2012). These methods are used because in dynamic rupture problems, there can be specific requirements to solve for fault boundary conditions while also honoring realistic fault and free-surface geometries. While computationally demanding, fully dynamic rupture simulations are useful tools to investigate which factors contribute most to the rupture history and to test potential mechanisms behind geophysical observations.

Cascadia

The potential earthquake and tsunami hazard to the U.S. Pacific Northwest coast is dominated by megathrust events from the Cascadia subduction zone. However, given the absence of modern seismic recordings of megathrust earthquakes and the fact that a majority of the seismogenic portion of the fault most likely lies offshore, there are outstanding unknowns regarding how the next megathrust event will behave. Complicating simulation efforts are distinct zones at depth along the Cascadia megathrust (i.e., the locked, transition, and episodic tremor and slow-slip regions) that have unique friction and stress conditions. While episodic tremor and slow-slip (ETS) is generally confined to 30 - 40 km depth along-strike (e.g., *Dragert*, 2001; *Wech and Creager*, 2011; *Hyndman*, 2013), these incredibly slow earthquakes have not been definitively detected at shallower depths, and thus an apparent gap exists between the locked and ETS regions. This feature brings into question whether or not slow-slip can penetrate the gap and transmit stresses to the locked region (e.g., *Segall and Bradley*, 2012; *Bruhat and Segall*, 2017) or if megathrust earthquakes can rupture into the ETS region (*Ramos and Huang*, 2019; *Lin et al.*, 2020). Given the incredibly low fault strength conditions ($\sim$1 MPa effective normal stress) that may exist in the ETS region, it is informative to see what dynamic rupture simulations predict as rupture encounters this portion of the fault. Note that an inferred low fault strength in this region is supported by several geophysical studies on low-frequency earthquakes, tremor, and stress inversion (i.e., *Gao et al.*, 2012; *Newton and Thomas*, 2020; *Rubinstein*, 2007; *Royer et al.*, 2015).

Another important aspect of the Cascadia megathrust revealed by many geological and geophysical studies is an apparent temporal and physical segmentation in interseismic slip behavior, geologic structure, or earthquake inferred recurrence interval (e.g., *Brudzinski and Allen*, 2007; *Goldfinger et al.*, 2017; *Watt and Brothers*, 2020; *Wells et al.*, 2003). Major differences in megathrust coupling and ETS partitions the megathrust into the northern, central and southern regions (*Brudzinski and Allen*, 2007; *Schmalzle et al.*, 2014). Present-day patterns in the interseismic velocity field may be indicative of temporal variations in strain-release suggested in the offshore paleoseismic record (e.g., *Goldfinger et al.*, 2003; *Wells et al.*, 2017). These systematic and along-strike changes in interplate slip processes

or upper plate expressions may hold clues about future coseismic rupture patterns.

Taking into account these observations about Cascadia, I seek to uncover how fault friction and stress conditions in the locked, gap, and ETS regions may control along-dip and along-strike rupture evolution and present a modest range of simulations to account for uncertainty in the true state of fault stress and friction levels. Developing future rupture scenarios in this manner has application to other global subduction zones that, like Cascadia, may have a dearth of seismic observations but are rich in other datasets (e.g., GPS geodesy, paleoseismology). These complementary observations can be harnessed to explore hypotheses about how megathrust strain accumulation may control the evolution of future event. Both 2-D and 3-D dynamic rupture simulations are generated for the Cascadia subduction zone.

2019 Ridgecrest Sequence

How dynamic stresses from seismic waves during rupture are transmitted from the source to nearby faults can tell us something about triggered fault creep, aftershocks, or a lack thereof. The recent 2019 Ridgecrest earthquake sequence in southern California jostled the seismological community by revealing a complex and cascading foreshock series that culminated in a M7.1 mainshock. But the central Garlock fault, despite being located immediately south of this sequence, did not fail. Instead, the Garlock fault underwent postseismic creep and exhibited a sizable earthquake swarm (e.g., *Barnhart et al.*, 2019; *Xu et al.*, 2020). I develop 2-D dynamic rupture simulations constructed from a kinematic slip-inversion model of the M7.1 event to explore how elastic stresses changed through time on the section of the Garlock fault. Moreover, I provide a thorough comparison between static and dynamic stress-changes from the Ridgecrest mainshock and discuss how this earthquake sequence affected the local stress-field in the Eastern California Shear Zone.

1.0.3 Outline

In Chapter 2, I draw upon recent geodetic models for shear stress-rate based on the joint inversion of GPS and vertical tide-gauge data (*Bruhat and Segall*, 2016, 2017). These inversions suggest an abrupt stress gradient near the inferred downdip limit of the locked zone in northern Cascadia. While the initial conditions suggested an energetically unfavorable condition for deeper rupture propagation, my models captured the exact opposite. Deeper rupture at faster speeds (supershear) is possible given the geodetic data, unless the transition region has a dynamic frictional behavior that strongly increases in response to slip or the strength of the megathrust in the ETS region is much higher than assumed. This study suggested the possibility of a wider Cascadia source zone model and a possible mechanism

for high-frequency energy radiation down-dip (i.e., when the rupture speed transitions to supershear).

Chapter 3 uses geodetic coupling models to inform shear stress distribution on the Cascadia megathrust that is used as input for 3-D dynamic rupture simulations. Besides being the first-ever 3-D dynamic rupture simulations for Cascadia, these models are constrained by observations unique to this subduction zone. This study highlights the importance of segmentation and dynamic stress-drop in the central Cascadia region (which is inferred to be creeping) to permit margin-wide ruptures to develop. I show that geodetic coupling models with a high slip deficit to the top of the Cascadia megathrust tend to generate margin-wide rupture, regardless of where rupture is initiated. Moreover, I provided a close fit to the 1700 A.D. subsidence measurements without invoking wide areas of high slip (high relative dynamic stress-drop) patches along-strike, which is in contrast to previous kinematic rupture studies (e.g., *Frankel et al.*, 2018; *Wirth et al.*, 2018; *Wirth and Frankel*, 2019). Results suggests that in the absence of margin-perpendicular (paleo)geodetic measurements, there are multiple ways to fit coastal subsidence data and several datasets must be used jointly to inform dynamic rupture models.

In chapter 4 I generate a physically consistent dynamic rupture model showing stress interactions vis-à-vis the Garlock fault during and after the Ridgecrest sequence using a slip-inversion model (*Ramos, M.D., Neo, J.C., Thakur, P., Huang, Y., Shengji*, 2020). I demonstrated that positive Coulomb stress changes impacted a section of the Garlock fault that was imaged from satellite data to have creeped for nearly 30 km. This result suggests that creep could have been induced on this section of the Garlock fault $<$ 1 minute into mainshock rupture. My models were successful in reproducing first-order inferences from kinematic inversions that suggested low mainshock rupture speeds ($\leq$ 2 km/s).

The overall contribution of this work is to inform seismic hazard with dynamic rupture simulations that are constrained by geologic, seismic, and geodetic observations. I am among the first to develop models of megathrust earthquakes in Cascadia that account for source dynamics. My Ridgecrest study fills in the missing link between foreshock and aftershock periods and shows the temporal nature of stress interactions near the Garlock fault, which has slipped in its past but did not in 2019.

CHAPTER II

How the transition region along the Cascadia megathrust influences coseismic behavior: Insights from 2-D dynamic rupture simulations *

Abstract

There is a strong need to model potential rupture behaviors for the next Cascadia megathrust earthquake. However, there exists significant uncertainty regarding the extent of downdip rupture and rupture speed. To address this problem, we study how the transition region (i.e., the gap), which separates the locked from slow-slip regions, influences coseismic rupture propagation using 2-D dynamic rupture simulations governed by a slip-weakening friction law. We show that rupture propagation through the gap is strongly controlled by the amount of accumulated tectonic initial shear stress and gap friction level. A large amplitude negative dynamic stress drop is needed to arrest downdip rupture. We also observe downdip supershear rupture when the gradient in effective normal stress from the locked to slow-slip regions is dramatic. Our results justify kinematic rupture models that extend below the gap and suggests the possibility of high-frequency energy radiation during the next Cascadia megathrust earthquake.

2.1 Introduction

Anticipating potential rupture behaviors during the next great earthquake from the Cascadia subduction zone (CSZ) is of paramount importance to the northwestern United States coast (*Wang and Tréhu*, 2016). Paleoseismic studies have uncovered the potential of the CSZ to generate magnitude 9 earthquakes through the mapping and dating of abruptly submerged coastal sediments (*Atwater*, 1987; *Kelsey et al.*, 2002), characterization of marine turbidite deposits (*Goldfinger et al.*, 2012, 2017), and paleo-tsunami records and modeling

*Chapter II is published in *Geophysical Research Letters*: Ramos, M.D and Huang, Y. "How the transition region along the Cascadia megathrust influences coseismic behavior: Insights from 2-D dynamic rupture simulations." Geophysical Research Letters 46.23 (2019). https://doi.org/ 10.1029/2018GL080812

(*Satake et al.*, 1996). Together these observations document repeated episodes of coseismic subsidence and tsunamigenesis. Models of the 1700 CE CSZ megathrust earthquake show temporal (*Goldfinger et al.*, 2003; *Priest et al.*, 2010) and spatial (*Leonard et al.*, 2010; *Wang et al.*, 2013) rupture variability along-strike, but the extent and characteristics of downdip rupture remains largely unknown. An outstanding question is if episodic tremor and slow-slip (ETS) events can be used as a proxy to map downdip rupture limits along subduction zone megathrusts. In Nankai, it has been observed that longer duration slow-slip events have, over time, occurred along a transition region that separates the locked from ETS regions of the megathrust (*Kobayashi*, 2012). Similar to Nankai, ETS in northern Cascadia is spatially distinct from the locked region and occurs at depths between 30 and 50 km (*Gomberg*, 2010; *Rodgers*, 2003; *Wech and Creager*, 2011), but the frictional behavior and stress state within the transition region (i.e., the gap) for the CSZ is poorly constrained (Figure 2.1). Developing coseismic rupture models that explore the gamut of fault stress, rheology, and friction levels in the gap is critical to seismic hazards analysis because this region could exert strong control on downdip rupture propagation.

Kinematic rupture models show that ground motions from the Cascadia megathrust earthquake are significantly impacted by the choice of hypocentral depth, downdip rupture limit, rupture speed, slip distribution, and high-stress drop subevents (*Delorey et al.*, 2014; *Frankel et al.*, 2018; *Melgar et al.*, 2016; *Olsen et al.*, 2008; *Wirth et al.*, 2018). In particular, Frankel2018b find that a deeper downdip rupture limit generally produces higher ground motion intensity for inland locations, mostly due to the deeper locations of high stress-drop ($\sim$20 MPa) subevents. It is also common to assume a range of 2–3 km/s for rupture speeds in kinematic rupture simulations. However, faster rupture usually results in larger ground motions (e.g., *Graves*, 2008), and an increase in the average rupture velocity from 2.1 to 2.3 km/s can lead to a factor of 1.5 difference in spectral acceleration values in Cascadia kinematic rupture models (*Wirth et al.*, 2018). Our goal is thus to provide physically informed constraints on kinematic rupture properties for a future CSZ megathrust earthquake by considering rupture dynamics and our current understanding of stresses and fault friction.

A notable feature of the CSZ is its relative lack of seismicity near the plate interface (*McCrory et al.*, 2012; *Stone et al.*, 2018; *Williams et al.*, 2011), which precludes conventional estimates of earthquake stress release (*Scholz and Campos*, 2012). However, recent insight into the state of shear stress based on the joint inversion of horizontal GPS and vertical tide-gauge data (*Bruhat and Segall*, 2016, 2017) suggests an abrupt gradient near the inferred downdip limit of the locked zone in northern Cascadia. In fact, negative shear stress rates in the gap appear to be a necessary condition to fit the vertical geodetic data,

irrespective of imposed locking depth (*Bruhat and Segall*, 2016). We aim to test this particular shear stress profile in the gap below northern Cascadia while addressing uncertainties in its amplitude across the gap using 2-D dynamic earthquake rupture simulations operating under a linear slip-weakening friction law. We find that shear stress and friction levels in the gap play a principal role in governing downdip rupture propagation. In addition, we also design simulations to represent dynamically what may occur for a rougher and hydrated megathrust fault below southern Cascadia. Our simulations predict that rupture can break through the gap and propagate into the ETS region, unless the gap has large negative stress drops whose amplitudes exceed those predicted by geodetically derived shear stress rates. These results support a seismic hazard source model that extends below the locked region, which can be directly implemented in current kinematic rupture models (*Frankel et al.*, 2018; *Wirth et al.*, 2018). These 2-D dynamic rupture models can also be used to inform future 3-D CSZ dynamic rupture models and other megathrust faults that possess a separation between the locked and ETS regions such as Nankai or Mexico (e.g., *Brudzinski et al.*, 2016; *Takagi et al.*, 2016).

2.2 Methodology

2.2.1 Model Geometry and Friction Law

We model the northern Cascadia megathrust as a 240-km-wide low-angle thrust fault dipping at $\sim$ 11 degrees that extends to a depth of 40 km (Figure 2.1). Our along-dip model geometry is simplified because we want to emphasize dynamic effects from heterogeneous stress or friction conditions on rupture propagation. We consider only the upper 40 km because this depth extent adequately captures all three regions of interest along the megathrust: the locked, gap, and ETS zones. Similarly, the model geometry for southern Cascadia also extends to 40 km depth (Figure 2.1), but is only 160 km wide to reflect the steeper subduction angle (*McCrory et al.*, 2012). Both faults are embedded in a homogeneous, isotropic, and linearly elastic half-space characterized by a shear modulus (G) of 30.0 GPa and Poisson's ratio (v) of 0.25. A hemispherical absorbing boundary encloses the lower half of each computational domain. Dynamic rupture propagation is solved using the 2-D spectral element code SEM2DPACK (*Ampuero*, 2009).

2.2.2 Constraints on Cascadia Megathrust Stress Conditions

Pore pressure is inferred to be at or near lithostatic levels in proximity to the forearc-mantle corner (*Audet et al.*, 2009; *Liu and Rice*, 2009; *Wech and Creager*, 2011). Higher pore pressure, which translates to lower effective normal stress levels, is also supported by ETS stress drop measurements that range between 0.01 and 1.0 MPa (*Gao et al.*, 2012) and the fact that small stress perturbations on the order of ∼0.01 MPa influence tremor activity (*Nakata et al.*, 2008; *Rubinstein*, 2007). The effective normal stress within the ETS region is thus set to 1 MPa in each simulation for both Cascadia models. For northern Cascadia, effective normal stress in the locked region is set to a constant 50 MPa and tapers down to 10 MPa in the upper 5 km of the fault, consistent with other fault models for northern Cascadia (*Liu and Rice*, 2009; *Li and Liu*, 2016). For each simulation, we assume a decreasing linear gradient in stress across the gap region. Within the locked region in southern Cascadia, however, we select a lower effective normal stress level of 30 MPa to represent a higher state of hydration, which implies elevated pore pressures (*Stone et al.*, 2018).

We estimate initial shear stress conditions for northern Cascadia using shear stress rate and gap width constraints below the Olympic Peninsula (*Bruhat and Segall*, 2016; *Holtkamp and Brudzinski*, 2010; *Schmalzle et al.*, 2014). The *Bruhat and Segall* (2016) inversion analysis requires an abrupt transition in shear stress rate at the base of the locked zone, assuming creep is not present above the specified locking depth. They deduced an upper bound of 35 kPa/year near the bottom of the locked zone (∼21 km depth), which we multiply by an average megathrust recurrence interval of ∼505 years (*Goldfinger et al.*, 2017) to arrive at the accumulated tectonic shear stress at the bottom of the locked zone (17.7 MPa) in our northern Cascadia models. By assuming a complete stress drop during the last megathrust rupture, we use the dynamic fault strength to represent the stress state immediately after the last megathrust earthquake. Thus, our initial shear stress level is the sum of the dynamic fault strength and the accumulated tectonic shear stress, which leads to an initial shear stress level of 27.7 MPa near the bottom of the locked zone (Figure 2.2). Applying the same procedure to the gap region, where a negative shear stress rate of -2.5 kPa/ year is estimated (*Bruhat and Segall*, 2016), we calculate an initial shear stress level of ∼4.3 MPa. Within the ETS region, we select a nominal initial shear stress level of 0.21 MPa to provide some positive stress drop. In some simulations, we increase the dynamic friction coefficient equal to or greater than the static friction coefficient value to represent a slip-neutral or slip-strengthening frictional behavior in the gap region. The accumulated tectonic shear stress is also added to the dynamic fault strength in these cases to obtain the initial shear stress levels.

We use a different approach to estimate shear stress levels in the locked region for

southern Cascadia. Estimations of the in situ stress state near the Mendicino Triple Junction suggest effective friction coefficients between 0.1 and 0.2 (*Li et al.*, 2018). Since the initial shear stresses calculated from these effective friction values are below our dynamic shear strength levels, we select a slightly larger effective friction coefficient (0.21) and multiply this value by the effective normal stress to obtain an average initial shear stress of 6.3 MPa in the locked region. Our model also accounts for a comparatively rougher megathrust fault as inferred from the highly deformed Gorda plate subducting below southern Cascadia (*Gulick*, 1998; *McCrory et al.*, 2012) and the marked increase in seismicity rate here (*Chen and McGuire*, 2016; *Li et al.*, 2018; *Stone et al.*, 2018) by incorporating heterogeneous distributions of effective normal and initial shear stress.

In our simulations, the dynamic strength affects the fault strength excess (the difference between the static shear strength and initial shear stress), whereas the accumulated tectonic shear stress is equivalent to the dynamic stress drop (the difference between the initial shear stress and dynamic shear strength). We use the S-ratio to quantify the ratio between fault strength excess and dynamic stress drop to investigate how rupture velocity may transition to amplitudes exceeding the shear-wave velocity, a phenomenon termed supershear (*Das*, 1977). A lower but positive S-ratio implies a higher initial shear stress given the same frictional strengths. But a deficit in initial shear stress relative to dynamic fault strength, which corresponds to a negative S-ratio, typically hinders rupture propagation. For mode II cracks governed by slip-weakening friction in homogeneous 2-D media supershear is encouraged when the S-ratio is below 1.77 (*Andrews*, 1985; *Dunham*, 2007).

2.2.3 Hypocenter Locations and Nucleation Procedure

The northern Cascadia model hypocenter is set to the downdip limit of the locked megathrust at 20 km depth (*Bruhat and Segall*, 2016) [(Figure 2.2)]. For the southern Cascadia model, we select a shallower hypocenter at 12 km depth, to be consistent with the downdip locking depth estimated there (*Schmalzle et al.*, 2014) [Figure 2.2]. We think these hypocenter choices are reasonable given (1) the maximum shear stress rate is located immediately above the gap from the *Bruhat and Segall* (2016) study and (2) the similar range of hypocenter depths of great earthquakes from global observations (*Lay et al.*, 2012). Rupture is artificially nucleated in both Cascadia models using the time-weakening method (*Andrews*, 1985).

2.3 Results

2.3.1 Northern Cascadia Simulations

To thoroughly study controls on downdip rupture propagation, we conduct a wide range of rupture models for both northern and southern Cascadia, assuming different dynamic friction coefficients, initial shear stress rate values, and effective normal stress levels in the locked, gap, and ETS regions (Figure 2.3). We highlight the results of three shear stress profiles across the gap in northern and southern Cascadia in Figure 2.2. In all three models, the initial shear stress asperity is at the base of the locked megathrust where rupture is nucleated. We simulate rupture until the rupture stops completely (150 or 90 s). The shallowest portion (depths $\leq$ 5 km) of the megathrust is assumed to be slip-weakening due to a lack of constraints, which leads to strong free-surface reflections (*Nielsen*, 1998).

Our first simulation considers the *Bruhat and Segall* (2016) stress rate profile from their preferred model and illustrates the effect of a negative dynamic stress drop in the gap (Figure 2.2). Whereas this stress condition in the gap should represent a barrier to rupture propagation, downdip rupture arrest is not observed in this scenario. Rupture can penetrate through the gap because the dynamic stress drop at the base of the locked megathrust provides sufficient energy to drive rupture downdip, regardless if dynamic stress drop becomes abruptly negative in the gap. The downdip rupture front propagates at $\sim$1 km/s in the gap and then accelerates to $\sim$2.8 km/s when it encounters the low static shear strength ETS region. Note that a daughter-crack indicative of a supershear rupture transition also emerges in the ETS region (Figure 2.2). In contrast, the updip rupture front is smooth and bifurcates at X = 90 km due to the tapering of stresses toward the deformation front (Figure 2a).

To explore what conditions could hinder downdip rupture propagation, we first assume slip-neutral friction across the gap (Figure 2.2). This means that the dynamic friction coefficient in the gap region is equal to the static level, which does not favor crack growth. We observe, however, that rupture still manages to propagate downdip, although the slip-rate is on average lower compared to the first simulation (Figure 2.2). We also observe several daughter-cracks with speeds exceeding the shear-wave velocity branching out from the primary downdip rupture front in the gap (Figure 2.2). The updip rupture front is unaffected by slip-neutral gap friction.

We found that the negative shear stress rate in the gap predicted by the *Bruhat and Segall* (2016) model by itself is insufficient to arrest down-dip rupture. Downdip rupture is impeded only if the gap has dynamic frictional levels greater than 0.6 and a negative shear stress rate of approximately $\sim$12 kPa/year is assumed in the gap, which leads to a much larger negative stress drop that inferred from the *Bruhat and Segall* (2016) model. We can

also assume an even more negative dynamic stress drop of $\sim$25.1 kPa/year and slip-neutral friction to arrest downdip rupture as well. While downdip rupture propagation beyond the influence of the time-weakening nucleation procedure is subdued, it does not hinder the free-surface reflection as it propagates back down the fault. We found that one way to effectively dampen the free-surface reflection is to increase the dynamic friction coefficient to at least 0.54 in the upper 5 km of the megathrust. We also tested a model where slip-neutral friction is present only in the ETS region, but this model does not arrest downdip rupture and produces rupture features that are qualitatively similar to the slip-weakening simulation. Assuming a lower initial shear stress rate at the base of the locked/gap regions and slip-weakening gap friction does not preclude downdip rupture either, but does retard the downdip rupture speed in the gap to less than 1 km/s. Our results show that it is the stresses and frictional conditions of the gap region, not the ETS region, that determine whether downdip rupture can penetrate deeper.

On the other hand, the observation of supershear rupture velocity near the ETS region strongly depends on the stresses and frictional conditions of the ETS region. If we depart from the 1 MPa effective normal stress level constraint in the ETS region, and either assume a lower fault strength gradient across the gap or a uniform fault strength level across the gap and ETS zones, we instead observe a coherent downdip rupture front that propagates at sub-Rayleigh speeds. These results demonstrate the sensitivity of the downdip kinematic properties to both the gap and ETS regions.

We summarize the final slip profiles from all northern Cascadia rupture models in Figure 2.3. Models that assume a higher static shear strength across the gap and ETS regions or slip-strengthening frictional behavior in the gap produce lower downdip slip amplitude (Figures 2.3). However, a majority of the models produce significant slip ($>$ 60 m) in the locked region and considerable slip ($\sim$20 m on average) in the gap and ETS regions (Figure 2.3). The peak slip in simulations with free-surface reflections occurs near the deformation front and is larger than that prescribed in previous kinematic rupture simulations. But the peak slip is more comparable to that prescribed in previous kinematic rupture simulations when free-surface effects are suppressed. Note that our slip profiles are more representative of the along-dip slip distribution through the hypocenter.

2.3.2 Southern Cascadia Simulations

The southern Cascadia region below 43 degrees N latitude is characterized by a steeper subduction angle, greater seismicity, and ample sediment entering the subduction zone that most likely has greater volumes of entrained water compared to northern Cascadia (*Flueh*,

1998; *Stone et al.*, 2018; *Trehu*, 1994). Since the spatial distribution of nonvolcanic tremor suggests a shorter gap width (Figure 2.2), we model the gap as an ∼20 km wide region across where both effective normal and initial shear stresses linearly decrease. We combine the effects of a rough fault and higher seismicity by implementing a stochastic effective normal stress and initial shear stress field, respectively. Such highly heterogeneous effective normal and initial shear stress conditions lead to significant fluctuations in the S-ratio, but still downdip rupture is not arrested (Figure 2.2). The shorter fault length of southern Cascadia megathrust leads to an overall shorter rupture duration compared to northern Cascadia rupture. We do not observe any daughter-cracks either updip or downdip. We also consider the effect of a rougher fault or higher seismicity separately and do not find that either stress parameterization produces drastically different results on the spatiotemporal rupture character; but a highly heterogeneous initial shear stress distribution along the locked region nearly doubles the final slip amplitude at the deformation front (Figure 2.3). We acknowledge that either shear or normal stress distribution depends on the particular stochastic stress level along the fault. However, the conclusion of rupture penetration through the gap is unaffected by these different stress parameterizations.

We also investigate the effects of the gap width by reducing it to approximately 500 m. Despite the drastic and unlikely gradient in fault strength, it shows that supershear transition can be attained almost immediately after the time-weakening procedure ceases. In contrast to the northern Cascadia models, the southern Cascadia models do not require the dynamic friction to increase completely to the static level in order to arrest downdip rupture: Both updip and downdip rupture fronts are impeded by a dynamic friction greater than 0.3 in the gap. Overall, the average final slip ofsouthern Cascadia rupture models is lower than that of northern Cascadia due to the smaller dynamic stress drop amplitudes in southern Cascadia (Figure 2.3).

2.4 Discussion and Conclusions

We consider a model of shear stress accumulation that implies a strong contrast in dynamic stress drop (positive to negative) at the locked/gap interface below northern Cascadia based on the shear stress rate estimated by (*Bruhat and Segall*, 2016). However, they assumed that the depth distribution of interseismic slip-rate is time invariant. *Bruhat and Segall* (2017) allowed updip propagation of interseismic slip into the locked region in their quasi-dynamic models and showed a similar transition in shear stress rate from the locked to gap regions. Their stress rate estimates vary with different model parameters. Among all the best-fitting models, the largest negative stress rate in the gap is approximately ∼20 kPa/year, which

is at the lower limit of the amplitude of negative shear stress rate that arrests downdip rupture in our models. This result demonstrates that the arrest of downdip rupture can be accomplished if the gap is slip-neutral, but with a negative shear stress rate that is an order of magnitude lower than the preferred *Bruhat and Segall* (2016) model.

Supershear rupture propagation can lead to increased ground velocities at greater distances *Andrews* (2010) and has been suggested by back-projection analysis of the Tohoku-Oki megathrust earthquake (*Meng et al.*, 2011). Our simulations show that the downdip rupture front can produce supershear daughter-cracks when encountering the ETS region (e.g., Figure 2.2). An exceptionally low amplitude effective normal stress in the ETS region and a high amplitude initial shear stress asperity are necessary to allow supershear daughter-cracks to jump ahead of the main rupture front downdip. To isolate the supershear effect, we assume slip-neutral friction in the upper 5 km of the fault to suppress the free-surface reflection and compare supershear rupture models to a sub-Rayleigh rupture model where the effective normal stress in the ETS region is increased to 10 MPa. We observe multiple wave pulses resulting from the supershear rupture in velocity seismograms recorded by a station near the location of Seattle (Figure 2.3). The pulses give rise to larger high-frequency ground motions in the first 40 s ($\sim$20-60 s). However, the peak ground velocity generated by the supershear ruptures are comparable to that generated by the sub-Rayleigh rupture. From a seismic hazard standpoint, the combined effects ofan offshore hypocenter (i.e., directivity), a deeper downdip rupture limit, and a higher rupture velocity could couple to low-velocity sedimentary basin amplification and change current ground motion prediction equation estimates (*Frankel et al.*, 2018; *Wirth et al.*, 2018; *Olsen et al.*, 2008). Supershear rupture velocity is one kinematic parameter that should be incorporated in future kinematic rupture models.

Our model for southern Cascadia also shows rupture penetrating through the gap (Figures 2.2). Kinematic rupture models suggest that if rupture extends to the top ofthe ETS region, coseismic uplift is predicted using an elastic half-space (*Wirth et al.*, 2018). Paleoseismic observations in the southern CSZ, on the other hand, support coseismic subsidence during the last megathrust rupture in 1700 CE (*Leonard et al.*, 2010; *Wang et al.*, 2013). While we also employed an elastic half-space model to simulate dynamic rupture, inelastic material effects around the fault zone and upper plate, or a nonplanar free-surface could also influence predicted coseismic uplift and subsidence signals (*Tinti and Armigliato*, 2002). Alternatively, the gap in southern Cascadia may behave as a barrier to downdip rupture relative to the ETS region if dynamic friction levels exceed 0.3 in the gap or if viscous-shear effects can impact coseismic rupture (*Gao and Wang*, 2017). It is also unclear whether the next Cascadia earthquake will rupture in a similar way as the 1700 Cascadia earthquake

(*Wang et al.*, 2013; *Wirth et al.*, 2018).

In addition to heterogeneous stresses or friction, slab geometry may significantly influence rupture propagation. Recent studies have suggested that smoother megathrusts naturally lead to larger earthquakes because a more homogeneous interface allows for more uniform fault strength distributions (*Bletery et al.*, 2016). Since the incoming plate offshore northern Cascadia is smoother compared to southern Cascadia (*van Rijsingen et al.*, 2018), along-strike rupture propagation may be easier to sustain and allow $\sim$M9 ruptures to develop. For lack of direct updip constraints on the shear stress state across the CSZ, we did not rigorously explore the parameter space beyond increasing the dynamic friction to limit the free-surface reflection. Previous dynamic rupture models of the 2011 Tohoku-Oki earthquake show that the free-surface reflection and shallow subduction angle assisted near-trench slip (*Huang et al.*, 2012, 2014), and we obtain a similar result in our 2-D models (Figures 2.3). Given the shallow subduction angle in the upper 5-km depth for most of the CSZ ($<$ 8 degrees), reflected waves in the wedge or deformation front may indeed form a viable mechanism to generate relatively large slip there, emphasizing the tsunami hazard (*Lotto et al.*, 2018; *Melgar et al.*, 2016).

Our dynamic rupture simulations show that if a sharp shear stress gradient exists at the base of the locked zone below northern Cascadia, downdip rupture propagation is not impeded unless the gap has higher dynamic friction and low shear stress rate levels. Extremely low effective normal stress in the ETS region also promotes supershear rupture, giving rise to high-frequency radiation. These results favor a deeper seismic source model for Cascadia and demonstrate that stress gradients and friction in the gap control downdip rupture extent.

2.5 Figures - Chapter 2

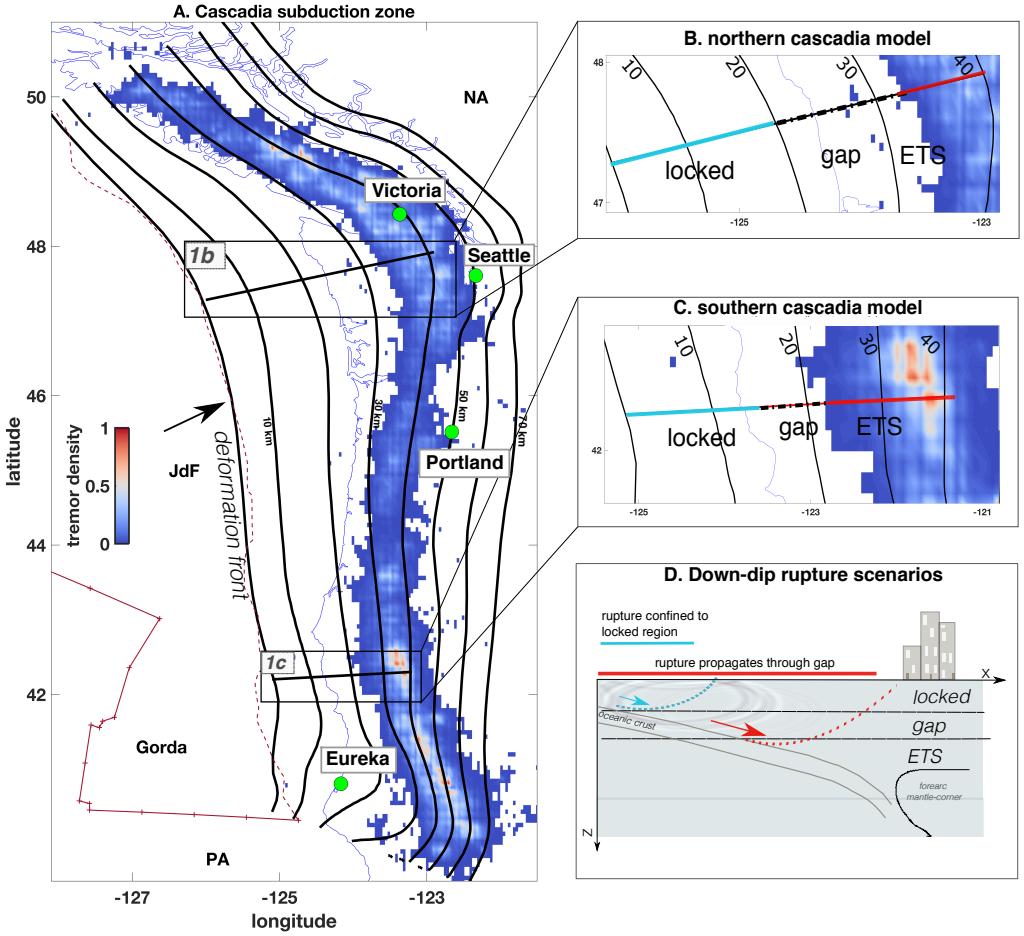

Figure 2.1: The Cascadia subduction zone. (a) Map of nonvolcanic tremor (normalized) density along the Cascadia megathrust from 2009 to 2018. Plate interface depths are given by the bold black lines in 10 km intervals. Major continental and oceanic are denoted as NA, PA, JdF, and Gorda. (b) 2-D rupture model setup across northern Cascadia showing the locked (solid teal line), gap (dashed black line), and ETS (solid red line) megathrust regions. (c) 2-D rupture model setup across southern Cascadia. (d) Schematic drawing of the two downdip rupture scenarios that highlight how if rupture can penetrate into the gap, seismic waves are brought closer to populated areas, extending the length of the earthquake source model. ETS = episodic tremor and slow-slip; NA = North America; PA = Pacific; JdF = Juan de Fuca.

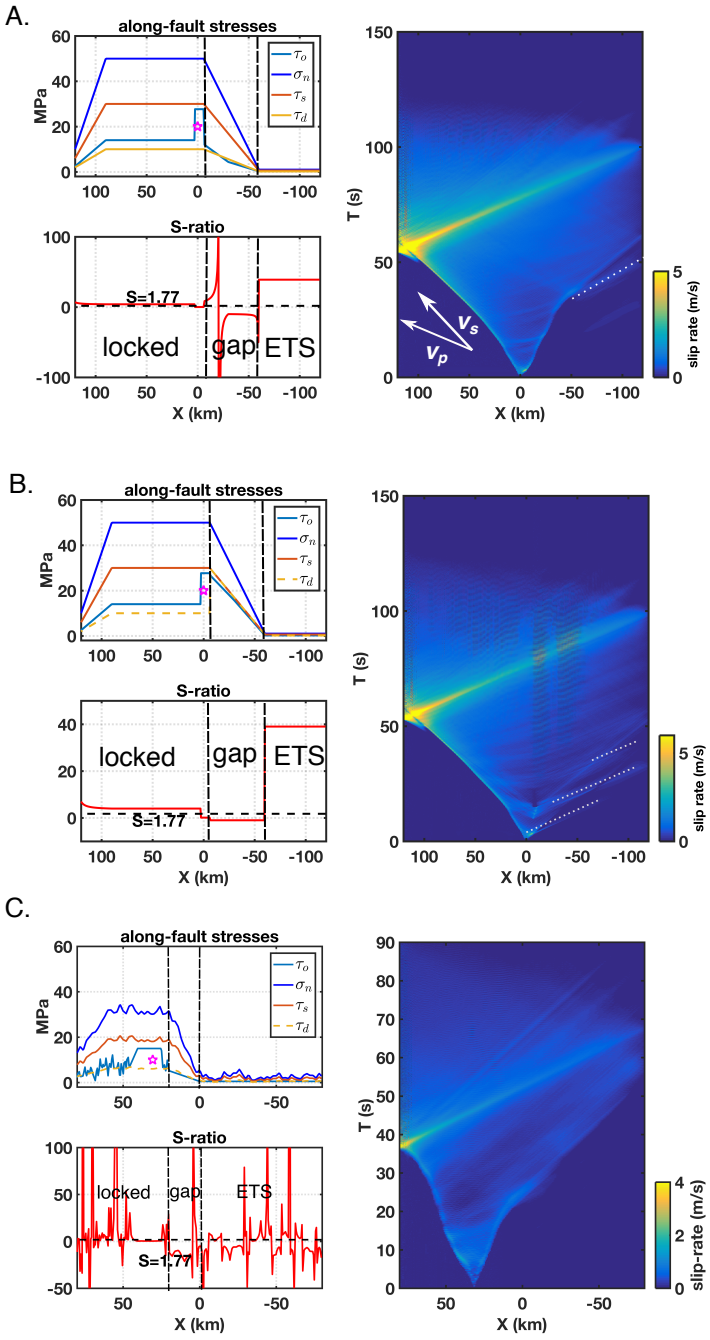

Figure 2.2: Dynamic rupture simulations for northern and southern Cascadia. The heavy dashed black lines partition the fault into the locked, gap, and ETS regions. Alongdip stresses, S-ratio, and resulting spatiotemporal rupture histories are shown for each model. (a) Northern Cascadia model assuming an initial shear stress asperity at the base ofthe locked region of the fault, a negative shear stress rate amplitude of $\sim$2.5 kPa/year in the gap, and the entire fault is assumed slip-weakening. (b) A northern Cascadia model assuming a dynamic friction coefficient level of 0.6 and an approximately $\sim$2.5 kPa/year shear stress rate in the gap. This model generates multiple downdip supershear daughter-cracks (white dotted lines). (c) Southern Cascadia model incorporating heterogeneous τ_o and σ_n perturbations to represent a rougher fault. ETS = episodic tremor and slow-slip.

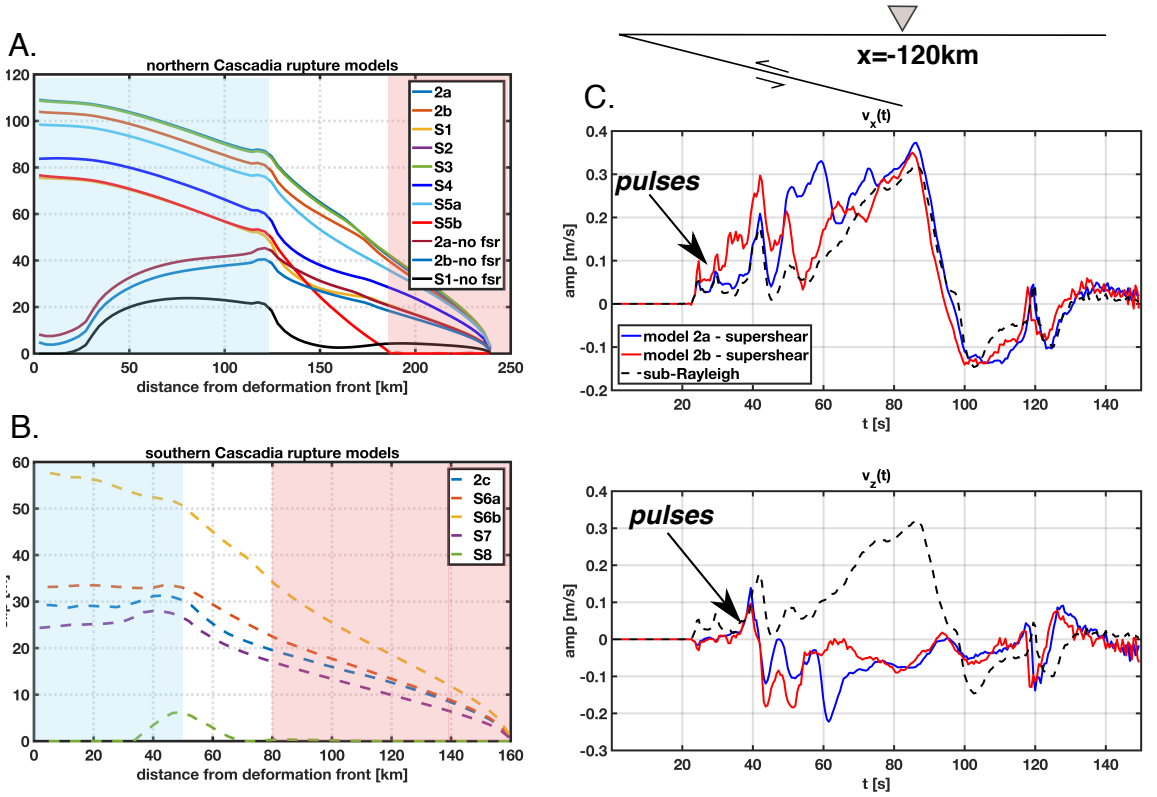

Figure 2.3: Final along-fault slip distributions for all rupture models and the effect of downdip supershear on synthetic waveforms. "No-fsr" models have the free- surface reflection suppressed by assuming slip-neutral friction in the upper 5 km of the fault. (a) Coseismic slip for northern Cascadia rupture models where the light blue and red regions signify the locked and ETS regions of the fault, respectively. The gap region is left unshaded. (b) Coseismic slip for southern Cascadia models. (c) Horizontal (top) and vertical (bottom) component seismograms for a station located at x = 120 km, immediately above the downdip edge of the modeled northern Cascadia megathrust. The wave pulses resulting from supershear rupture are indicated.

CHAPTER III

Assessing Margin-Wide Rupture Behaviors along the Cascadia Megathrust with 3-D Dynamic Rupture Simulations *

Abstract

From California to British Columbia, the Pacific Northwest coast bears an omnipresent earthquake and tsunami hazard from the Cascadia subduction zone. Multiple lines of evidence suggests that magnitude eight and greater megathrust earthquakes have occurred - the most recent being 321 years ago (i.e., 1700 A.D.). Outstanding questions for the next great megathrust event include where it will initiate, what conditions are favorable for rupture to span the convergent margin, and how much slip may be expected. We develop the first 3-D fully dynamic rupture simulations that are driven by fault stress, strength and friction to address these questions. The initial dynamic stress-drop distribution in our simulations is constrained by geodetic coupling models, with segment locations taken from geologic analyses. We document the sensitivity of nucleation location and stress-drop to the final seismic moment and coseismic subsidence amplitudes. We find that the final earthquake size strongly depends on the amount of slip-deficit in the central Cascadia region, which is inferred to be creeping interseismically, for a given initiation location in southern or northern Cascadia. Several simulations are also presented here that can closely approximate recorded coastal subsidence from the 1700 A.D. event without invoking localized high-stress asperities along the down-dip locked region of the megathrust. These results can be used to inform earthquake and tsunami hazards for not only Cascadia, but other subduction zones that have limited seismic observations but a wealth of geodetic inference.

*ChapterIII is submitted to *Journal of Geophysical Research: Solid Earth*: Ramos, M. D., et al. "Assessing Margin-Wide Rupture Behaviors along the Cascadia Megathrust with 3-D Dynamic Rupture Simulations." Journal of Geophysical Research: Solid Earth (202X).

3.1 Introduction

The Cascadia subduction zone megathrust dominates the earthquake hazard in the United States Pacific Northwest. It is oft-cited that the probability of a magnitude ∼9 (M9) event occurring in the coming decades is between 10 – 14 percent (Peterson et al., 2014). The most recent megathrust rupture in Cascadia occurred in 1700 A.D. and generated a transoceanic tsunami (*Heaton, T.H. Hartzell, S. H.*, 1987). Matching amplitudes of historical tsunami records from Japan requires a magnitude between M8.7 - 9.2 for this earthquake (*Satake et al.*, 1996; *Satake*, 2003). While 321 years have elapsed since this last great earthquake, the Holocene (<12 kya) earthquake record onshore and offshore documents even older M >8 megathrust events. (e.g., *Atwater and Griggs*, 2012; *Goldfinger et al.*, 2012, 2017; *Kemp et al.*, 2018; *Leonard et al.*, 2010).

3.1.1 Geological and Geophysical Inferences on the State of Megathrust Segmentation

Several geological and geophysical observations suggest the Cascadia megathrust exhibits along-strike segmentation. For example, there are systematic changes in the accretionary wedge backstop geometry, seismicity, and interseismic slip patterns (e.g., *Bartlow*, 2020; *Stone et al.*, 2018; *Watt and Brothers*, 2020) that may indicate coseismic rupture patterns will also be variable along-strike. The strongest observational constraints that may inform our understanding of future great earthquakes come from paleoseismic and geodetic observations. Underwater turbidite deposits, which can be generated from submarine landslides induced by strong ground-shaking during megathrust earthquakes, have been extensively used to map along-strike rupture extents (*Goldfinger et al.*, 2003, 2012, 2017). Analysis of the timing and spatial extents of turbidite deposits suggests that the recurrence interval (RI) between megathrust earthquakes could vary along the Cascadia margin (Figure 3.1). In particular, the RI estimated for northern Cascadia (<46°latitude) exceeds 400 years whereas it is estimated to be less than 200 years for the southern portions of Cascadia (<43°latitude).

Decadal scale interseismic velocities measured at the Earth's surface by Global Navigation Satellite System (GNSS) networks, tide gauge, and leveling data also find significant along strike variations in coupling (slip-deficit) distributions along the margin. Regions in northern and southern Cascadia have higher coupling suggesting they are accumulating strain that may be released in a future great earthquake (*Li et al.*, 2018; *Schmalzle et al.*, 2014; *Yousefi et al.*, 2020, Figure 1b,c). However, the use of geodetic coupling inversions to place bounds on the future down-dip or along-strike rupture extent is complicated by het-

erogeneous frictional properties (*Boulton et al.*, 2019) or the potential presence of stress-shadows (*Almeida et al.*, 2018; *Hetland and Simons*, 2010) and other factors (e.g., crustal thickening, off-fault deformation). Therefore, the down-dip extent of coupling and coseismic rupture may differ even though these inversion results are the best available constraint on potential stress distributions for the Cascadia megathrust (*Wang and Tréhu*, 2016).

Another piece of evidence for megathrust segmentation comes from the behavior of episodic tremor and slip (ETS) events along the margin. In GNSS displacement records, ETS manifests as transient reversals in displacement indicative of slip on or near the megathrust at depths between 30 and 40 km. These slow slip episodes are often accompanied by a weak seismic signature known as nonvolcanic tremor (*Rodgers*, 2003). The character of ETS events varies significantly along the margin. The northern (i.e. $>47°$) and southern ($<43°$) sections host more frequent slip episodes with average recurrence intervals of 10 and 14 months and have higher tremor density, whereas the central section of the megathrust hosts ETS approximately every 19 months (*Brudzinski and Allen*, 2007; *Wech and Creager*, 2011). Studies of the ETS source region find that the phenomenon occurs in regions of significantly elevated Vp/Vs ratios (e.g., *Audet et al.*, 2009; *Delph et al.*, 2018) and that tremor, and constituent low-frequency earthquakes, are extremely sensitive to small magnitude stress changes such as those from the solid Earth tides (*Royer et al.*, 2015). Collectively, these observations suggest that pore fluid pressures are nearly lithostatic in the ETS source region. The Cascadia megathrust also features a transition zone at depth that separates the ETS region from the region that is conventionally considered to be locked at $\sim$ 20-km depth (*Hyndman*, 2013). Known as the gap, this spatial disconnect in slip behavior is also found in other subduction zones (*Gao and Wang*, 2017); the gap may or may not participate in coseismic rupture (*Ramos and Huang*, 2019).

3.1.2 Cascadia Earthquake Source Models

What are ways to anticipate how a future Cascadia megathrust earthquake may behave? One way to assess the seismic and tsunami hazard posed by large seismic events in Cascadia is to use kinematic rupture simulations. Kinematic rupture simulations are commonplace due to the straightforward relationship between fault slip and the recorded elastic displacement field once the Green's functions are known, allowing these types of models to be run at lower computational cost. Using the kinematic framework, potential locations of strong-ground motion sources, sedimentary basin amplification or tsunami generation have been assessed (*Delorey et al.*, 2014; *Frankel et al.*, 2018; *Melgar et al.*, 2016; *Olsen et al.*, 2008; *Roten et al.*, 2019; *Wirth and Frankel*, 2019). Most of these kinematic rupture

models calibrate first-order rupture parameters (slip, slip-rate, rise-time or rupture speed) from the few large megathrust earthquakes observed in other subduction zones (e.g., M8.2 2003 Tokachi-Oki, M9.2 2004 Sumatra-Andaman, M8.8 2010 Maule, M9.1 2011 Tohoku-Oki). Kinematic simulations provide important constraints on strong ground motions felt onshore, but because they must assume a slip distribution before computing the elastic wavefield and thus cannot answer what controls the final rupture size.

To account for source physics, fully dynamic rupture simulations can be used to investigate what controls the final rupture size and kinematic rupture properties like rupture speed. Dynamic rupture simulations are self-consistent, physics-based numerical models that describe the entire earthquake rupture process (nucleation, propagation, and arrest) that is coupled a constitutive fault friction law (e.g., *Madariaga, R. and Olsen*, 2002). To date, 2-D dynamic rupture models in Cascadia have focused on tsunami generation (*Lotto et al.*, 2018) or how frictional and stress conditions in the transition zone may influence down-dip rupture extent (*Ramos and Huang*, 2019).

Here we develop 3-D dynamic rupture simulations to explore how variable strain accumulation rates, frictional behavior and hypocenter location influence megathrust rupture dynamics. We will use geodetic coupling results from *Schmalzle et al.* (2014), who utilized GNSS time series information spanning several decades for their coupling inversions. These coupling distributions represent two possible end-member scenarios for strain accumulation near the deformation front: either there is interseismic creep at shallow megathrust depths (hereafter referred to as the Gaussian coupling model; Figure 3.1) or it is fully coupled here (hereafter referred to as the Gamma coupling model; Figure 3.1). Specifically, these coupling models will be used to estimate the dynamic stress drop, which is defined as the difference between the initial shear stress and dynamic fault strength. Dynamic stress drop is a key parameter determining how much energy is available for rupture propagation (*Kanamori and Rivera*, 2004). Our dynamic stress drop levels are further constrained by strain accumulation times and segment locations adopted from paleoseismic studies (i.e., *Goldfinger et al.*, 2017, Figure 3.1). We compare the resulting coseismic uplift and subsidence patterns to available paleoseismic measurements and discuss which classes of models allow margin-wide ruptures to develop. We find the final earthquake size is sensitive to earthquake nucleation location (e.g., northern vs. southern Cascadia) and the distribution of relative dynamic stress drop. The principal control on margin-wide rupture, when using these particular end member geodetic coupling models, is the relative dynamic stress drop amplitude in the central Cascadia region ($\sim$43 - 47°latitude). The results also suggest that Gamma coupling models tend to produce larger earthquakes, even if shallow subducted sediment has a slip-strengthening or velocity-strengthening frictional behavior.

Another intriguing question is if geodetic coupling models can inform our understanding about the 1700 A.D. earthquake when incorporated into a dynamic rupture simulation. To that end, we also present several rupture simulations that provide a close fit to the 1700 A.D. event.

3.2 Methodology

We solve for 3-D elastodynamic earthquake rupture using SeisSol, a powerful open-source software package that implements the Arbitrary high-order DERivative-Discontinuous Galerkin (ADER-DG) approach to simulate wave propagation coupled to spontaneous dynamic rupture (*De La Puente et al.*, 2009; *Heinecke*; *Pelties et al.*, 2012; *Uphoff et al.*, 2017). The capability of SeisSol to solve for complex source dynamics and incorporate realistic geometric features, such as bathymetry, topography and fault zone structure (e.g., *Ulrich et al.*, 2019; *Wollherr et al.*, 2019) nicely lends itself to our purposes of investigating how heterogeneous megathrust stresses influence rupture behavior.

We generate an unstructured 3-D tetrahedral mesh for the Cascadia subduction zone that spans over 1100 km along-strike (39.0 to 51.0 degrees latitude, -127.5 to -121.0 degrees longitude) and we use static refinement to increase resolution locally. The average on-fault element edge size (h) is 2.5 km, and the maximum depth of the fault mesh is 50 km *Hayes et al.* (2018) and includes over 440,000 unstructured triangular elements. We account for the large-scale variations in the free-surface geometry by meshing the ETOPO1 topography and bathymetry dataset to 1 km average element size near the coastline. In all of our simulations, we use ADER-DG with fifth order accuracy (polynomial order p = 4) in time and space.

We ensure simulation results are sufficiently resolved by following the procedure established in *Wollherr et al.* (2018) to estimate the process zone, the region behind the rupture front where the fault strength drops from its static to dynamic level. For the 2.5-km fault mesh, the median process zone width(Λ_m) is 1.1 km. The recommended number of elements needed to resolve Λ_m in a purely elastic setup with depth-dependent initial conditions is 2 - 3 (p = 4). The quadrature points approach utilized in SeisSol ensures each element edge length is sampled p + 2 times (*Pelties et al.*, 2014). Given our setup, Λ_m is sampled by $\sim$2.7 elements which is within the recommended range. The expected relative percent error in the rupture arrival time, peak slip-rate, and final slip are 0.9, 8.32, and 0.71, respectively (*Wollherr et al.*, 2018). While the peak slip-rate relative error is slightly larger than the 7% recommended by *Day et al.* (2005) for elastic rupture problems, we compare our model-predicted slip and rupture size to higher resolution meshes with h = 1 km and h

= 0.5 km and observe negligible changes, which gives us confidence that these first order rupture features are correctly resolved. The highest resolution mesh has more than 50 million elements and requires 22 hours on 40 nodes of the supercomputer SuperMUC-NG at the Leibniz Supercomputing Centre, Germany.

3.2.1 Constraining Dynamic Rupture with Geodetic Coupling Models

In our Cascadia simulations, potential shear stress distributions are informed by geodetic coupling models. The *Schmalzle et al.* (2014) inversion for slip-rate deficit was performed with respect to a Cascadia megathrust geometry predating Slab2 (*McCrory et al.*, 2012) and as such, we first map the geodetic coupling models to our megathrust geometry through a bilinear interpolation using the cartesian horizontal plane coordinates. But the effect of this transformation does not distort the coupling model (Figure 3.1).

We define the parameter T as the time needed for a certain level of slip-deficit to accumulate on a section of the megathrust. The product of slip-rate deficit (coupling) and T is slip deficit. T should not be interpreted as the recurrence interval (RI), but rather as another way to quantify relative dynamic stress-drop along the megathrust. From these slip distributions, we estimate the static stress-drop using Poly3D, a three-dimensional, polygonal element, displacement discontinuity boundary element method, which accounts for nonplanar megathrust geometry and the free-surface effect due to buried slip (*Thomas*, 1993).

Initial shear stress is then estimated by adding the static stress-drop to the dynamic fault strength. Calculating the initial shear stress in this manner is known as the complete stress-drop assumption and assumes that slip-deficit is accumulated linearly in the along-dip fault dimension and will be entirely released during coseismic rupture (*Hok et al.*, 2011; *Yang et al.*, 2019a,b). This shear stress distribution is first resampled to an average grid spacing of $\sim$3 km and then linearly interpolated onto the fault mesh. We note that we initialise stress values and friction parameters with a high-order subelement resolution (e.g., *Pelties et al.*, 2014) . For all dynamic rupture simulations considered, we compare the results to the 1700 A.D. subsidence measurements along the coast, where available (*Wang et al.*, 2013), and to recorded subsidence amplitudes from other M9 earthquakes (e.g., 2011 Tohoku, 1960 Chile, 1964 Alaska).

3.2.2 Material Properties and Fault Strength

Wave propagation is simulated within a heterogenous, linearly elastic medium where the elastic moduli (lame parameters) vary as a function of depth. The average 1-D velocity

structure is taken from the Cascadia 3-D Community Velocity Model (3D-CVM) for P and S waves (*Stephenson et al.*, 2017, Figure 3.2). Since the goal of this study is to calculate upper plate deformation and rupture extent (along-dip and along-strike) for a given dynamic stress-drop distribution, we believe this is a satisfactory simplification to make. We estimate that we can resolve a cutoff seismic frequency up to ∼0.4 Hz in the near fault region. High frequency (>1 Hz) broadband ground motions can be calculated at a higher computational cost if an appropriate 3-D velocity model is utilized. The current 3D-CVM was developed with respect to an older Cascadia subduction zone geometry (i.e., *McCrory et al.*, 2012) and thus, we leave direct extrapolation of this 3-D velocity model to our model geometry can be left for future work.

Effective normal stress accounts for pore pressure counteracting vertical lithostatic stress on the fault. We use the depth-dependent effective normal stress distribution for Cascadia presented in *Ramos and Huang* (2019) that includes low strength levels (1 MPa) in the ETS region (Figure 3.2). These incredibly low effective stress conditions in the ETS region are supported by observations the sensitivity of tremor and low-frequency earthquakes to small magnitude stress changes (e.g., *Rubinstein*, 2007; *Royer et al.*, 2015), stress orientations in the ETS region (e.g., *Newton and Thomas*, 2020), and low stress-drops of ETS events (e.g., *Gao et al.*, 2012). For lack of in-situ fault stress information, we assume a linear stress gradient above and below the locked region (10 – 20 km depth) that are consistent with other Cascadia megathrust simulations (*Liu and Rice*, 2009; *Li and Liu*, 2016). Such assumptions are simple but allow us to focus on how heterogeneous shear stresses on the megathrust contribute to first order rupture characteristics.

3.2.3 Fault friction law

The physics controlling the inelastic breakdown process in our dynamic simulations is given by a nonsingular linear slip-weakening friction law (*Palmer*, 1973). This constitutive friction law allows us to idealize rupture as a propagating shear-crack. It is completely described by the static (μ_s) and dynamic (μ_d) friction coefficients and a critical slip-weakening distance (D_c).

We set $\mu_s = 0.6$ and $\mu_d = 0.1$ within the locked region of the megathrust (5 km $\leq$ z $\leq$ 22 km) [Figure 3.2]. Because *Ramos and Huang* (2019) showed that rupture can penetrate the gap or generate strong free-surface reflections if its frictional behavior is slip-weakening at depths $<$ 5 km and at depths $>$ 25 km (in conjunction with a highly negative stress-drop), we set μ_d equal to or above μ_s in these regions (Figure 3.2). D_c is set to a constant level of 1 m or 2 m. $D_c = 2$ m is selected in the dynamic rupture model in which the stress and strength

conditions of *Ramos and Huang* (2019) are extrapolated along strike, for consistency with the 2-D dynamic rupture simulations. D_c=1 m is used for the dynamic rupture models based on the heterogeneous geodetic coupling prestress distributions. Our range of Dc values are consistent with those used in slip-weakening simulations of the Tohoku-Oki earthquake, which constrained Dc using the frequency range of back-projection results (*Huang et al.*, 2014). We make minimalistic assumptions for cohesion, a material property of the rock surrounding the fault, in the upper 5 km of the megathrust (Figure 3.2). Due to the nearly zero dynamic stress-drop amplitudes near the deformation front for Gaussian coupling models, the cohesion gradient can be low (Figure 3.2). But in the case of the Gamma coupling models, relatively higher cohesion levels ($\sim$5 MPa average) are locally needed at shallow fault depths to prevent fault failure at the start of the simulation (Figure 3.2).

3.2.4 Rupture Initiation

Fault pre-stress conditions influence the estimated critical nucleation size when using a linear slip-weakening friction law. The theoretical critical nucleation radius that permits spontaneous dynamic rupture to initiate in a 3-D linearly elastic and homogeneous media has been derived by *Day* (1982) and is given by,

$$r_c = \frac{7\pi}{24}\frac{G(S+1)}{\Delta\sigma_d}D_c \tag{3.1}$$

where G is the shear modulus, S is the relative fault strength defined as the ratio between strength excess (static fault strength minus initial shear stress) and dynamic stress-drop ($\Delta\sigma_d$). Expression (1) provides a sufficient means to initiate and sustain dynamic rupture propagation for the 3-D dynamic rupture model that is adapted from 2-D dynamic rupture simulations presented in (*Ramos and Huang*, 2019). For the prestress distributions derived from the heterogeneous coupling models, we determine the best numerical nucleation size through a trial-and-error approach. We find that critical nucleation radii are within $\sim$10% of the theoretically predicted value calculated from equation (1). Rupture initiation is prescribed by a space and time dependent rupture initiation function, leading to an imposed rupture velocity that decreases away from the hypocenter and allows a gradual transition from forced to spontaneous rupture. Rupture nucleation locations are chosen within the areas presenting local maxima in the dynamic stress-drop distribution (see Figure 3.1). Each dynamic rupture simulation is run for 420 seconds (7 minutes) to allow seismic waves to propagate to the edge of the model domain and assess accurately the final ground deformation.

3.3 Results

3.3.1 Translating 2-D rupture simulations to 3-D

A 3-D dynamic rupture model that assumes a relatively homogeneous dynamic stress-drop profile along the locked region of the megathrust is shown in Figure 3.3. Previously developed 2-D dynamic rupture simulations (*Ramos and Huang*, 2019) were relative to a specific location in northern Cascadia, which is where we initiate rupture (Figure 3.3). Such a laterally uniform dynamic stress-drop distribution is unlikely given observations of geophysical and geological megathrust segmentation (e.g., *Watt and Brothers*, 2020). However, we develop such a simulation to demonstrate 1) what a megathrust event would appear as if there was a strong gradient in shear stress-rate from the locked to gap regions (20 - 30 km depth) across the margin and 2) how this scenario would influence coastal subsidence amplitudes.

In spite of the low dynamic stress-drop (<5 MPa) at depths shallower than 10 km and slip-strengthening friction, coseismic slip is able to reach the deformation front with amplitudes exceeding 60 m in most locations along-strike (Figure 3.3). The along-strike variation of slip at the deformation front exhibits two peaks north and south of the hypocenter - even though the initial dynamic stress-drop distribution is laterally invariant, the final coseismic slip pattern is not (Figure 3.4). This is attributed to the along-strike changes in megathrust dip. There are also small amounts of slip (< 5 m) in the gap region. The coseismic hingeline, separating regions of subsidence from regions of uplift, is entirely offshore (Figure 3.3). Subsidence levels exceeding 5 m are observed along most of the coastline (Figure 3.3). This exceeds subsidence measurements from the 1700 A.D. event (*Wang et al.*, 2013) by at least a factor of two because the earthquake is much larger than an M9 (Figure 3.3). Such subsidence amplitudes are also much larger than the maximum levels observed for the 2011 M9.0 Tohoku (∼1.1 m *Hashima et al.*, 2016), 1964 M 9.4 Alaska (∼2.4 m *Plafker*, 1972) or the largest ever recorded event, the 1960 M9.5 Chile Earthquake (∼2.7 m *Plafker, G., Savage*, 1970).

Interestingly, this model generates a down-dip rupture-front that can reach and be sustained across the ETS region, despite the negative dynamic stress-drop in the gap combined with slip-neutral frictional behavior(Figure 3.5). Due to stress perturbations emanated from rupture up-dip, we think this down-dip rupture front is most likely related to dynamic triggering and unclamping of the fault that is made possible by the incredibly low static fault strength here (i.e., 0.6 MPa).

3.3.2 Uniform Gaussian and Gamma coupling models

We now explore dynamic rupture scenarios based on the Gaussian and Gamma coupling models. We start with simulations that assume uniform T level (Figure 3.6). T is set to its 320 years, the time elapsed since the most recent event (*Goldfinger et al.*, 2017). In such a parameterization, the highest dynamic stress-drop amplitude is located in the northern Cascadia region for both Gaussian and Gamma distributions (Figure 3.6), which is where spontaneous rupture is initiated. The location of highest dynamic stress-drop is not co-incident between the Gaussian and Gamma coupling models, and hence the hypocentral locations are slightly different. Uniform T for both coupling models generates margin-wide rupture with coastal subsidence amplitudes that again exceed 1700 A.D. (Figure 3.6). The Gamma coupling model has higher dynamic stress-drop than the Gaussian model near the deformation front, which leads to a 1 to 2-meter difference in subsidence amplitude for the northern ($0 < Y < 200$ km) region of the megathrust (Figure 3.6). These subsidence amplitudes, while lower than the 2-D extrapolated model, still surpass the estimated subsidence amplitudes of the largest recorded global megathrust earthquakes (i.e., 1960 Chile, 1964 Alaska). This result demonstrates that the uniform T coupling model overestimates the amount of slip-deficit accumulated since 1700 A.D.

When comparing the along-dip gradient of dynamic stress-drop between the simple (i.e., Figure 3.3) and heterogeneous 3-D models (i.e., Figure 3.6), we note that the smoother model extends slightly deeper (Figure 3.5). The amplitude of coseismic subsidence is probably more strongly controlled by the dynamic stress-drop gradient towards the coastline (Figure 3.7). A point to note is that the region of higher relative dynamic stress-drop in the northern Cascadia region ($0 < Y < 200$ km) is also where there are limited paleoseismic measurements from 1700 A.D. Thus, while geodetic coupling models are well constrained here, the few along-strike subsidence measurements limit rigorous comparison to physics-based model predictions.

3.3.3 Segmented Gaussian and Gamma coupling models

We find that in order to produce coseismic uplift and subsidence amplitudes more consistent with the paleoseismic Cascadia measurements and data from other megathrust earthquakes (i.e., ±2 m), we must prescribe along-strike variations of T, with T amplitudes lower than 320 years for a particular segment. This is especially needed for the northern and southern regions of the Cascadia megathrust, where both the Gaussian and Gamma coupling models predict higher subsidence amplitudes than observed if T is set to 320 years. We refer readers to the discussion section on the possible meaning of these lower T values.

Our partitioning of the margin is informed by paleoseismic (*Goldfinger et al.*, 2012, 2017), ETS (*Brudzinski and Allen*, 2007), and morphotectonic studies (*Watt and Brothers*, 2020) in Cascadia. The following dynamic rupture models are parameterized using at least three segments. This choice is conservative - we found through trial-and-error that two segment models cannot match first-order 1700 A.D. subsidence patterns as well as three-segment models. We note that some geologic models may suggest up to five segments (e.g., *Goldfinger et al.*, 2017; *Wang et al.*, 2013) and thus there may be multiple ways to partition T levels along-strike.

Three segment rupture models that are nucleated in the northern Cascadia region are first studied to see how our choice of T and segment width affect final rupture length (Figure 3.8). We found that placing segment limits near ∼46 and 43 degrees latitude (Y ranges from 180 to -350 km; Figure 3.8), together with T levels between 200 – 250 years (∼8 – 10-m slip deficit), leads to margin-wide rupture. The position of these segment limits corresponds to changes in estimated RI level, tremor patterns and forearc morphology (Figure 1 *Goldfinger et al.*, 2017; *Watt and Brothers*, 2020). The middle segment encompasses most of the creeping region offshore Oregon. Holding T levels constant, we systematically move the location of the southern segment boundary southward until margin-wide rupture is no longer observed. An average slip-deficit of nearly 2 m over a width of ∼80 km is needed to drive rupture through the creeping section and into the southern end of Cascadia (Figure 3.8a,dashed-line). The higher coupling in the northernmost segment (Y $>$ 200 km) allows for rupture to propagate north of the epicenter in all cases. In contrast, if we use the Gamma coupling model, margin-wide rupture is much easier to attain even with lower relative stress-drop (lower T values) (Figure 3.8b). Lower T levels are used in the Gamma rupture simulations as higher values are not required to achieve margin-wide rupture with the Gamma distribution. This result demonstrates the sensitivity of margin-wide rupture to the stress level in the shallow portions of the fault. As the length of the central segment becomes shorter, moment-magnitude only weakly decreases (by ∼0.01) for Gamma ruptures. Gamma ruptures nucleated in northern Cascadia can feature shallow, narrow slip distributions and low rupture speeds ranging from ∼1 to 2 km/s in the central region of the megathrust (Figure 3.9).

For dynamic ruptures initiated in southern Cascadia, we found that slightly higher T levels (relative to ruptures nucleated in the north) were a necessary condition to sustain rupture propagation, particularly through the central Cascadia region (Figure 3.8). Gaussian models that lead to a margin-wide rupture required an additional slip-deficit of 3 m over a length of ∼60 km in the central segment (i.e., Figure 3.8c,dashed line) compared to non margin-wide rupture event (i.e., Figure 3.8c, dot-dashed line). Similar to what was

observed for ruptures initiated in northern Cascadia, Gamma coupling models tend to generate margin-wide ruptures at much lower slip-deficit (i.e., Figure 3.8d). Higher relative T levels in the southernmost segment is required in order for rupture to initiate and propagate outside the region of spontaneous rupture initiation, given our slip-weakening friction parameters (i.e., μ_d, μ_d, D_c) and effective normal stress that bound the fracture energy. The Cascadia megathrust dips more steeply in southern Cascadia, and this probably influences the initial stages of ruptures that propagate from south to north more than those that rupture north to south. In general, Gamma model results suggest that only a narrow region of concentrated higher dynamic-stress drop is sufficient for promoting margin-wide rupture, even if slip-strengthening friction or higher sediment cohesion levels are present. We will now discuss our assumptions about sediment friction in the shallow most portions of the megathrust, and its effect on rupture size.

3.3.4 Effect of up-dip frictional behavior

In all simulations presented so far, we have assumed the influence of subducting sediments will lead to slip-strengthening frictional behavior in the upper 5-km of the megathrust along-strike. We now relax this assumption and let the dynamic friction level vary from slip-strengthening to slip-weakening conditions (Figure 3.10) using the reference Gaussian model of Figure 3.8 (solid line). In all simulations, we fix T levels and segment locations, while testing varying dynamic friction coefficients in the near-margin region. Neither slip-strengthening ($\mu_d > 0.6$) nor slip-neutral (μ_d=μ_s=0.6) friction leads to margin-wide rupture for this particular parameterization (Figure 3.10a). Only a slip-weakening behavior at shallow depths allows rupture to spontaneously grow into a margin-wide event. The effect of dynamic friction level on slip at the deformation front is shown in Figure 3.10b. We observe high slip amplitudes (>25 m) in northern and southern Cascadia and reduced slip in central Cascadia (Figure 3.10). In the margin-wide rupture case (e.g., μ_d= 0.1), this slip pattern is similar to other Gaussian coupling models.

3.3.5 Effect of down-dip locking depth

Estimating the seismogenic width from the available geodetic data and paleoseismic measurements (*Hyndman*, 2013; *Wang and Tréhu*, 2016) is fraught with uncertainty because of their lack of margin-perpendicular resolution. In both the Gaussian and Gamma coupling models, the down-dip limit of coupling (positive stress-drop) is near 20 km depth (Figure 3.1), broadly consistent with thermal models proposed for this subduction zone (*Cozzens and Spinelli*, 2012; *Hyndman*, 2013; *Wang et al.*, 1995). To assess how locking depth in-

fluences rupture width, length and subsidence amplitudes, we now relax this assumption and let locking depth vary. Again, we start with the three-segment Gaussian simulation (Figure 3.8a, solid line), which did not break through the central Cascadia region (Figure 3.11a). Slip-weakening behavior with μ_d=0.1 is initially set to end at 20 km depth and we systematically extend locking depth by two kilometers until 30 km (Figure 3.11a). A dynamic rupture simulation assuming a shallower 15-km locking depth is also shown for sake of comparison. We observe that moment-magnitude increases ($8.8 < \text{Mw} < 9.2$) due to rupture penetrating the gap and ETS regions of the fault. The ruptures progressively extend further south for greater locking depth, but do not become margin-wide (Figure 3.11a).

We select a 2-D profile near the hypocenter along-strike to assess how the model predicts coseismic subsidence and amplitude patterns change in the margin-perpendicular direction (Figure 3.11b). The maximum uplift and subsidence amplitudes increases by $\sim$1 m for every 2-km increase in locking depth. For deeper locking depths, the coseismic hinge-line moves closer to shore, although all hinge-lines remain at least 100 km offshore for the profile selected in northern Cascadia (Figure 3.11b). The location of greatest coastal subsidence can be taken as a proxy for the down-dip rupture limit which is consistent with elastic dislocation models described by *Kanda and Simons* (2012) that account for the effect of megathrust curvature on the slip gradient and subsequently, uplift and subsidence measurements.

3.3.6 Fitting 1700 A.D. subsidence measurements

Previous elastic rupture models have shown that coastal subsidence measurements from 1700 A.D. can be well fit with high slip-patches positioned along-strike. *Wang et al.* (2013) used static models with four distinct asperities with T levels ranging from 450 – 550 years (18 – 22 m slip-deficit) to reproduce the subsidence amplitudes. In these static models, the greatest locking depth was taken to taken to coincide with the 350C isotherm as this is where silica-rich lithologies would be expected to transition from velocity-weakening to velocity-strengthening frictional behavior (i.e., *Wang et al.*, 2003). 3-D kinematic simulations used a range of locking depths ($\sim$10 - 30 km) and determined that, in the presence of subevents, a locking depth near $\sim$15 km provided the strongest fit to the subsidence data (*Wirth and Frankel*, 2019).

We present four 3-D dynamic rupture scenarios derived from Gaussian and Gamma coupling distributions with a shallower locking depth at 15 km, but we also note that deeper locking depths were also tested (see Discussion). The T levels and segment locations were selected through a trial-and-error approach. These dynamic source models show 1700

A.D. subsidence data can be reasonably fit without invoking high amplitude slip-deficit or subevents (Figure 3.12). Ruptures initiated in northern Cascadia with modest T levels ($\leq$250 years) can match subsidence data with three segments (Figure 3.12a) whereas we find that four segments are required for the Gaussian rupture model initiated in southern Cascadia (Figure 3.12b). The Gaussian-type simulation initiated in southern Cascadia has a final rupture length $\sim$100 km shorter than the other ruptures.

3.4 Discussion

3.4.1 What allows large earthquakes to develop along the Cascadia megathrust?

We observe margin-wide ruptures under conditions of higher relative dynamic stress-drop amplitudes in the inferred creeping region of the central Cascadia megathrust (higher T levels relative to the other segments). Alternatively, we also show that margin-wide ruptures are promoted by slip weakening frictional behavior at shallow depth (Figure 3.10).

When the Gaussian or Gamma coupling models are used to generate heterogeneous shear stress distributions, there are two natural locations to initiate spontaneous rupture: in northern or southern Cascadia. Our results suggest that if rupture initiates in southern Cascadia, higher T levels are required to sustain rupture through the central creeping region for Gaussian stress distributions (Figure 3.8c). This is due to the combined effects from a lower slip-rate deficit (inherent to both geodetic coupling models) and the generally narrower seismogenic rupture area offshore Oregon caused by an increasing megathrust dip angle in this region.

A notable feature of our dynamic rupture simulations is that large earthquakes (Mw 8.8 and above) can be generated at much lower T levels than previously suggested from static models (i.e., *Wang et al.*, 2013). An explanation for this comes from dynamic effects within the wedge. For instance, even though Gaussian simulations have little to no slip-deficit extending to the deformation front, reflections within the accretionary wedge appear to drive rupture propagation along-strike. While a more realistic rheology within the wedge would certainly affect wave propagation, our models suggest that wavefield inference at shallow depths could be a viable mechanism to sustain rupture (*Huang et al.*, 2014). It is a common assumption in dynamic rupture simulations of megathrust earthquakes to assume velocity strengthening (or in our case, slip-strengthening) frictional behaviors (*Kozdon and Dunham*, 2013) to represent sediments near the trench. One may also explicitly incorporate a subducting sediment channel structure with depth-varying rigidity using slip-weakening

friction (i.e., *Ulrich, T., Gabriel, A.A., Madden, E. H.*, 2020). The presence of clays or fluids within the megathrust fault zone can complicate the frictional behavior, however (*Saffer and Tobin*, 2011). While Cascadia is well-known to have significant sediment blanketing the trench along-strike with variable state of consolidation (*Han et al.*, 2017), there are few studies that directly sampled Cascadia megathrust fault gouge and subject them to high-velocity friction experiments (*Seyler et al.*, 2020). The assumption of slip-strengthening friction in the upper 5 km in our dynamic rupture simulations is therefore modest and will greatly benefit from offshore drilling data. We do not repeat the exercise of lowering the dynamic friction level for ruptures nucleated in southern Cascadia (or for Gamma models), but we expect that a longer rupture length or a higher slip would occur.

3.4.2 Explaining 1700 A.D. subsidence patterns with Dynamic Rupture Simulations

The geodetic coupling models we use show positive stress-drop down to $\sim$20 km depth (Figure 3.1). On the other hand, 3-D kinematic simulations were able to match 1700 A.D. subsidence data assuming positive stress-drop does not extend deeper than a fixed coupling level closer to 15 km depth (i.e., 1 cm/yr contour, *Burgette et al.*, 2009; *McCaffrey et al.*, 2013; *Wirth and Frankel*, 2019). We show that dynamic rupture simulations which taper stress-drop to 0 MPa below 16 km depth can agree well with the 1700 A.D subsidence data, particularly for ruptures initiated in northern Cascadia (Figure 3.12). While shallower locking depths generally provide a stronger fit to the paleoseismic data, we were also able to construct a dynamic rupture simulation with a 20-km locking depth that fits the data just as well (Figure 3.13). This result suggests that if T levels are sufficiently low along the fault, the subsidence patterns can probably be fit by an even deeper locking depth ($>$20 km). To reiterate, the influence of a deeper locking depth is to move the coseismic hinge-line landwards and increase the amplitude of subsidence and uplift (i.e., Figure 3.11b). As discussed in *Kanda and Simons* (2012), either the location of peak interseismic uplift-rate or greatest coseismic subsidence can provide a stronger constraint on the extent of coupling as opposed to the hinge-line. Unfortunately, both the interseismic uplift (i.e., *Krogstad et al.*, 2016) and paleoseismic subsidence data (i.e., *Wang et al.*, 2013) are limited in the along-dip direction for this subduction zone. We thus caution using only paleoseismic subsidence data to uniquely constrain the down-dip rupture limit in Cascadia.

3.4.3 The Potential of Heterogeneous Down-dip Frictional Properties

The next Cascadia megathrust rupture may or may not include high-frequency seismic energy radiated near the down-dip limit of slip (e.g., *Lay*, 2015), but one way to accomplish this is to superimpose high stress-drop subevents (>15 MPa) at several locations along-strike (Figure 3.14). The influence of subevents, compared to a coupling model with no subevents, is to increase the subsidence amplitude and generate higher relative frequencies.

To conceptually demonstrate that heterogeneous D_c can also generate relatively higher seismic frequencies in the specific case of the Cascadian margin, we also design a dynamic rupture simulation containing several 16 km^2 asperities near the down-dip edge of the locked megathrust that have lower D_c=1 m with D_c=2m everywhere else (Figure 3.15). These D_c levels are chosen to be consistent with already presented 3-D rupture simulations that can resolve the cohesive zone widths. In this particular model, the effect of a heterogeneous D_c distribution is to increase waveform amplitudes and high-frequency energy, with stations further away from the hypocenter showing this more clearly (Figure 3.15).

What is unclear are the set of conditions along the fault most conducive to generating high frequency seismic radiation down-dip. Dynamic rupture simulations for the 2011 Tohoku-Oki earthquake showed that heterogeneous frictional properties or strength distributions (*Huang et al.*, 2012, 2014; *Galvez et al.*, 2014) might account for these observations. We note that Cascadia is remarkably different from the Japanese or Chilean subduction zones. In particular, the subducting interface of the Juan de Fuca plate is relatively smooth along most of the margin compared to in the aforementioned regions (i.e., *van Rijsingen et al.*, 2018) and consequently, interface topography may not provide an obvious explanation for future high seismic frequencies radiated down-dip.

3.4.4 Limitations and Future Directions

Our study incorporates a physically consistent source model that emphasizes the importance of frictional and stress conditions necessary to generate M9-type ruptures. For lack of detailed information on the velocity structure in the accretionary prism and the highly simplified 1-D CVM used, our 3-D dynamic rupture simulations do not capture accurate wave propagation effects along the Cascadia margin. Forecasting accurate ground motions during megathrust earthquakes is important, especially for subduction zones with limited or no seismic recordings (*Frankel et al.*, 2018; *Wirth et al.*, 2018). Developing dynamic rupture simulations that account for 3-D source, site, and path effects is one future direction that would, for instance, lead to more physically informed hazard estimates (i.e., *Wirth et al.*, 2020).

Another limitation of our study is the rheology assumed: a linearly elastic body. There is potential for off-fault plastic yielding in the wedge where there is a significant sediment volume (*Ma*, 2012). We note further that our choice of a linear slip-weakening friction law allows us to assess first order along-strike and along-dip rupture limits, similar to (*Ramos and Huang*, 2019). Modifying the friction law (and adjusting the finite element mesh resolution accordingly) to account for strong rate-weakening would permit us to test a wider range of rupture styles. Understanding what fault zone lithologies are present along the Cascadia megathrust would also be helpful in assigning realistic dynamic friction levels during coseismic rupture.

To improve the predictive capability of dynamic rupture simulations, offshore (e.g. near-trench) geodetic measurements are needed. It would be particularly valuable if information about the interseismic uplift-rate could be constrained offshore, to extend existing leveling data onshore (*Krogstad et al.*, 2016). This would reduce the ambiguity in geodetic coupling models and improve our understanding of the spatial relationships between upper plate deformation and intra-plate slip behavior (*Bruhat and Segall*, 2017; *Malatesta, L. C., Bruhat, L., Finnegan, N. J., Olive*, 2021; *Watt and Brothers*, 2020). Our study stresses the importance of the spatial variation in coupling, especially in the central Cascadia region where confirming the presence of lower coupling offshore Oregon is critical for both kinematic and dynamic rupture simulation predictions.

Other geophysical measurements that have not been incorporated in this suite of dynamic rupture simulations include inferences made about the seismogenic width from the arguably highest resolution geophysical dataset available: the free-air gravity field. *Basset and Watts* (2015) observed that trench-parallel ridges in the free-air gravity anomaly field correlate well to the top of slow-slip and tremor across the Cascadia forearc. If such trench-parallel features in the gravity field are a proxy for down-dip rupture extent, then the transition from slip-weakening to slip-strengthening frictional behavior may extend to depths greater than 20 km in some regions of Cascadia. More work is needed to identify what geologic or geophysical features are most indicative of future coseismic rupture limits, especially in subduction zones like Cascadia that have not experienced megathrust events during the modern era of instrumentation.

3.5 Conclusions

Developing realistic seismic source models for the Cascadia megathrust is of paramount importance to assist with seismic and tsunami risk mitigation. We present 3-D dynamic rupture simulations that incorporate different hypotheses for megathrust strain accumula-

tion based on geodetic coupling models. We show that in order for margin-wide, 'M9' type ruptures to develop, there must be a sufficiently high relative dynamic stress drop in the central Cascadia region. Moreover, a slip weakening behavior or moderate slip deficit close to the deformation-front can greatly facilitate margin-wide ruptures. Along-strike variations in the slip deficit pattern relative to the geodetic coupling models are required to match available paleoseismic data in our dynamic rupture models. We note that strain accumulation times lower than those suggested from paleoseismic studies provide a better fit to the subsidence data, which might suggest coupling models are overpredicting the slip-rate deficit or there was incomplete stress drop from the last megathrust rupture. A close fit to 1700 A.D. subsidence data can be achieved using Gaussian or Gamma coupling distributions with locking depths of 15 or 20-km depth, obviating the need to call upon localized, high amplitude slip asperities along the down-dip region of the seismogenic zone.

This work is a step forward in using fully dynamic rupture simulations for seismic hazard analysis where there have been no instrumentally recorded ruptures. Kinematic rupture properties (e.g., rise-time, slip-rate and rupture speed) and static seafloor displacement from our dynamic simulations can be readily incorporated into existing 3-D kinematic rupture simulations or inform tsunami propagation and coastal inundation models.

3.6 Figures - Chapter 3

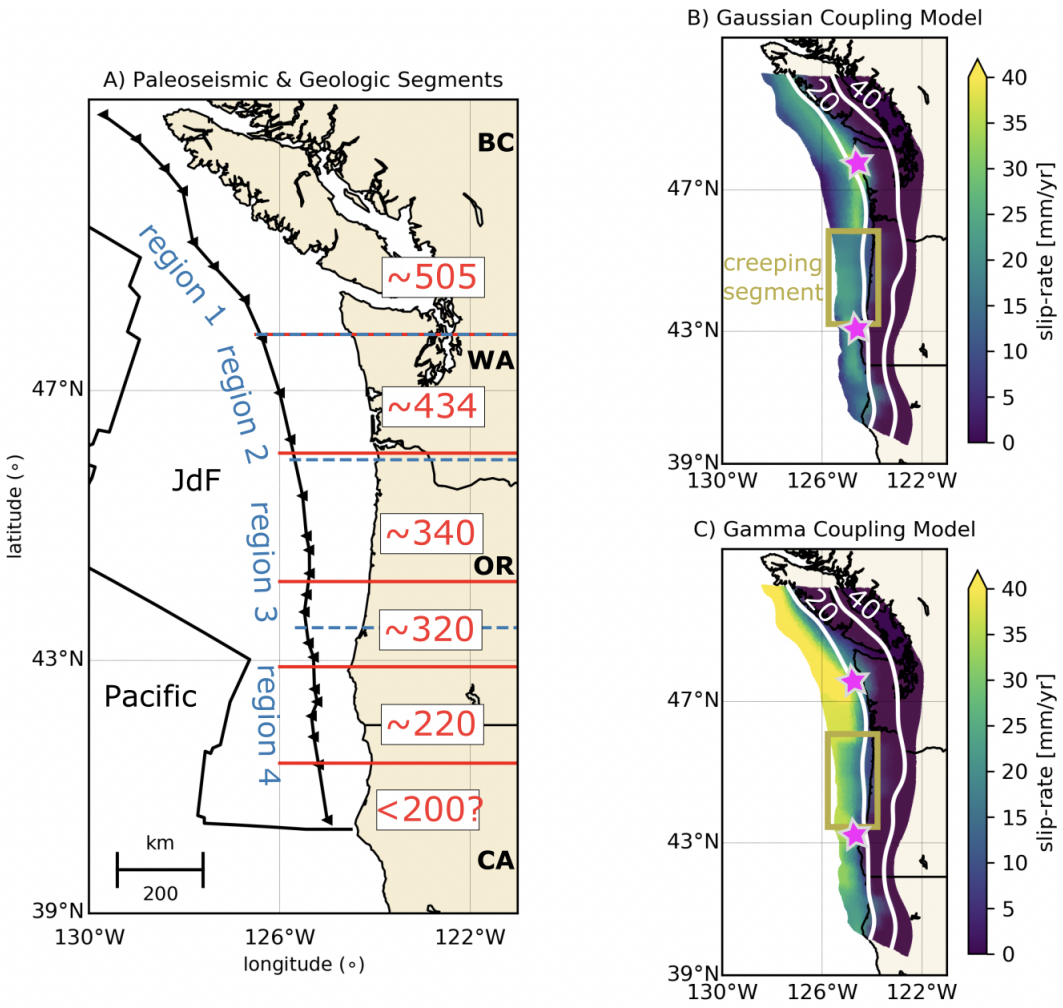

Figure 3.1: Cascadia subduction zone study area. A) Megathrust segmentation (segments are separated by red lines) suggested from offshore turbidite deposits with corresponding estimated segment recurrence intervals in years. Primary morphotectonic regions are superposed (blue dashed lines). B) Gaussian and C) Gamma coupling models projected onto the Slab2 megathrust geometry. The Gaussian coupling model assumes interseismic creep at shallow megathrust depths whereas the Gamma model assumes high strain accumulation. The inferred region of the creeping segment is denoted by a yellow box. Magenta stars denote rupture initiation locations in our dynamic rupture models. Thick white lines are megathrust depth contours (kilometers). JdF = Juan de Fuca plate.

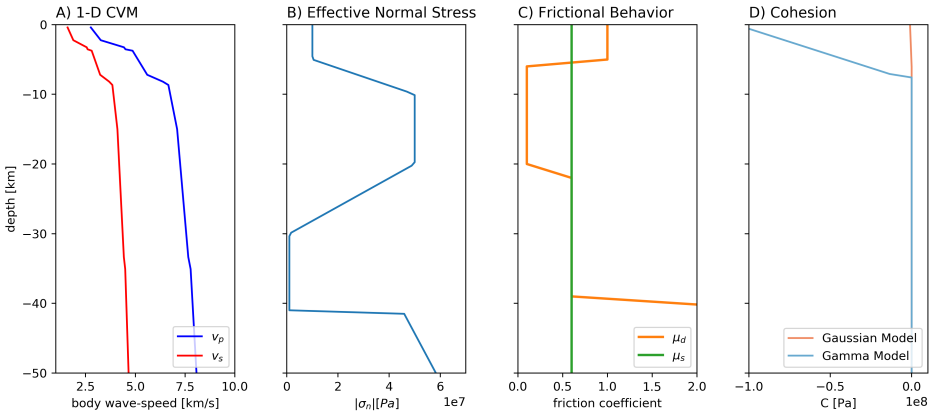

Figure 3.2: Material properties, stress, and frictional conditions for dynamic rupture simulations. A) Smoothed 1-D CVM velocity model for Cascadia (*Stephenson et al.*, 2017). B) Effective normal stress. C) Dynamic and static frictional coefficients with depth. D) Frictional cohesion for the Gaussian and Gamma coupling models.

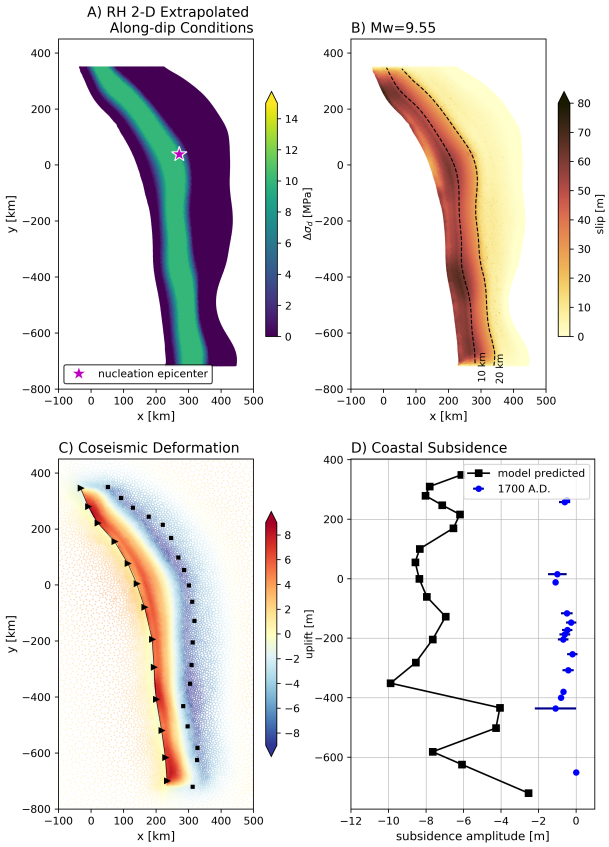

Figure 3.3: Dynamic rupture simulation results when stress and strength conditions from Ramos & Huang (2019) are extrapolated along-strike. A) Along-strike dynamic stress-drop and epicenter location. B) Final megathrust slip-distribution and moment-magnitude. The black dashed lines indicate the 10 and 20 km depth contours to highlight the extent of down-dip rupture. C) Coseismic uplift (red) and subsidence (blue) along the Cascadia margin. Squares signify the coastline whereas the triangles denote the deformation front. D) Model predicted (black squares; same as panel as C) and paleoseismic observations of estimated subsidence during the 1700 A.D. rupture.

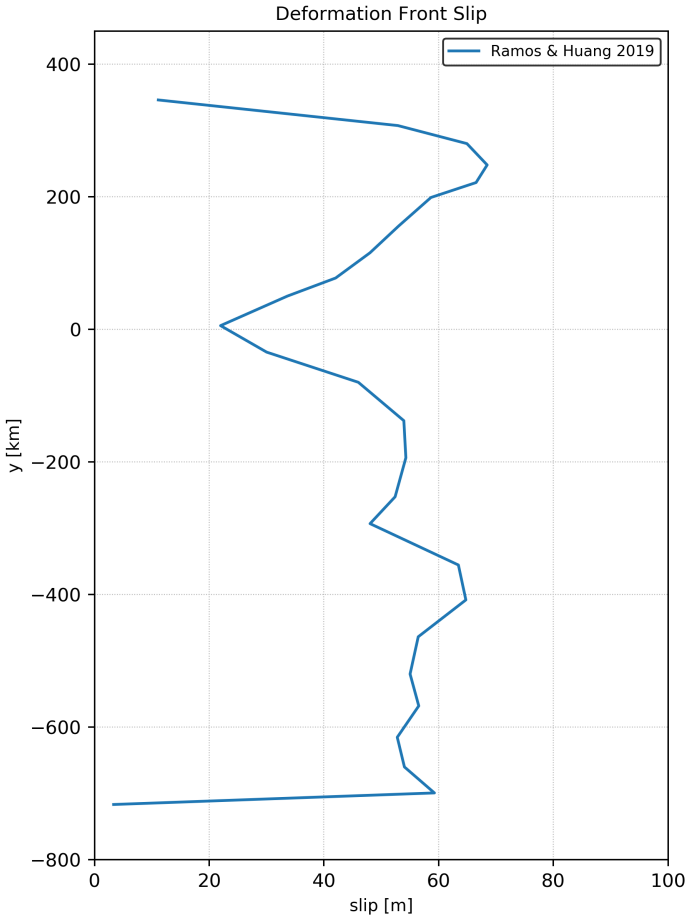

Figure 3.4: Slip at the deformation front for smooth model presented in Figure 3.

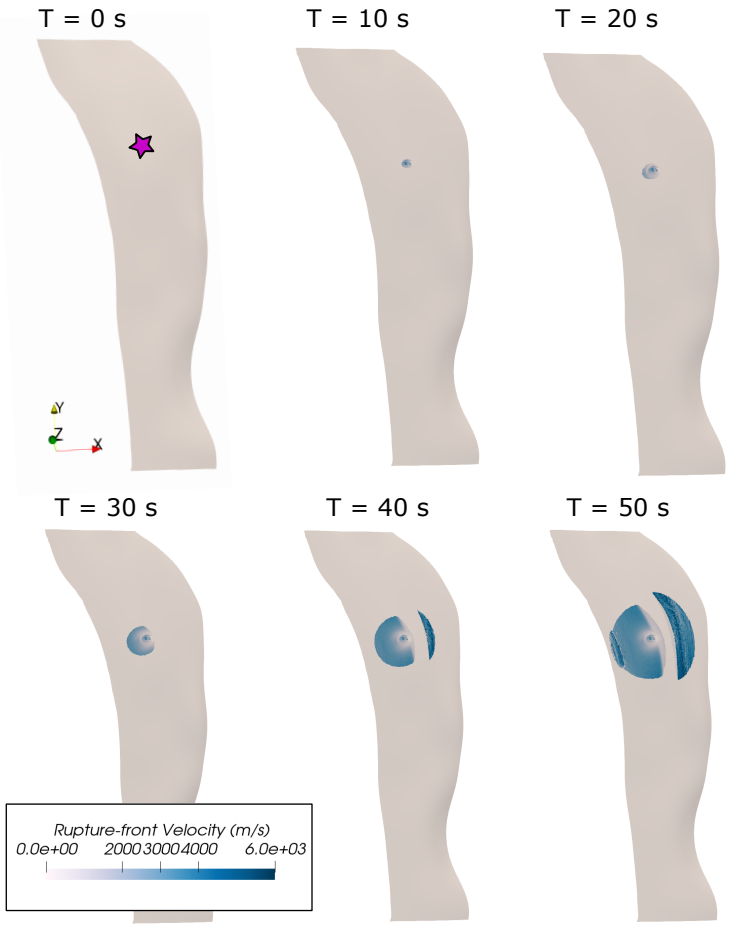

Figure 3.5: Snapshots of the rupture-front velocity at certain times. The downdip rupture front is due to dynamic wave triggering and from up-dip. This feature is possible because of the incredibly low fault strength in the ETS region (0.6 MPa and 0.1 MPa for the static and dynamic strengths, respectively).

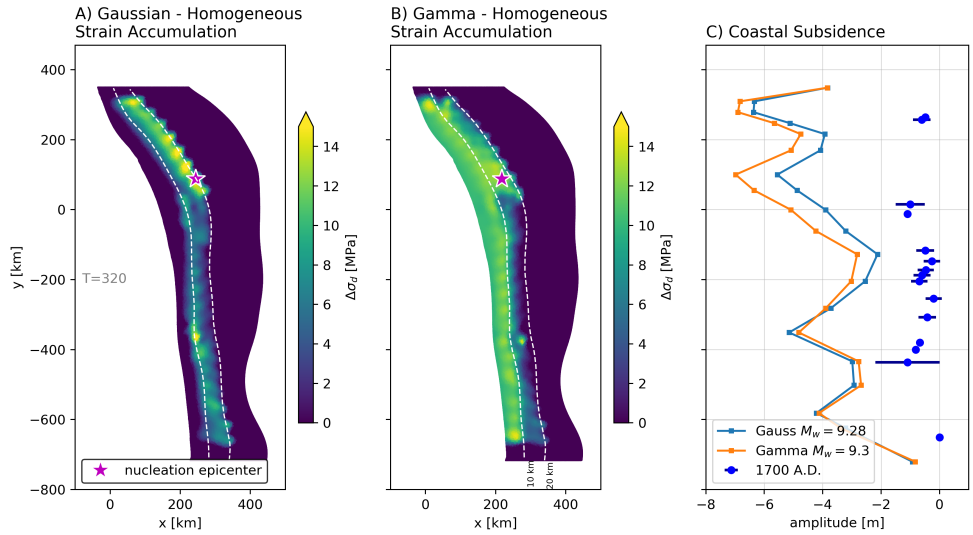

Figure 3.6: Comparison between Gaussian and Gamma dynamic stress-drop distributions and the resultant subsidence patterns assuming the maximum strain accumulation time (T) of 320 years (i.e., time since the last great earthquake in 1700 A.D.) A) Dynamic stress-drop distribution for the Gaussian coupling model. B) Dynamic stress-drop distribution for the Gamma coupling model. Both ruptures are nucleated in northern Cascadia (magenta star). C) model predicted subsidence along the coastline compared to 1700 A.D. measurements.

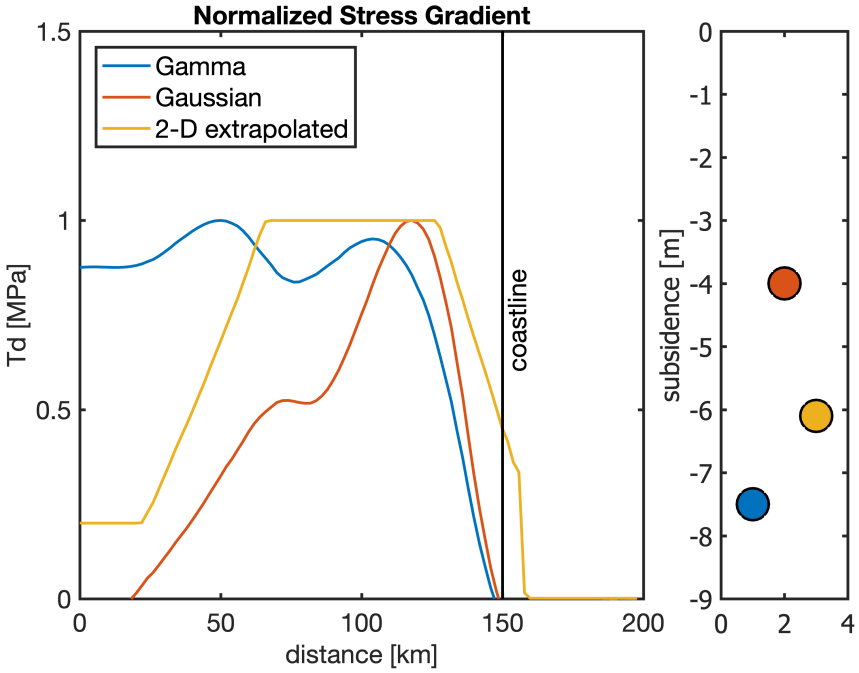

Figure 3.7: Example along-dip shear stress gradients between smooth and coupling models (left) and typical subsidence amplitudes predicted for each stress gradient (right). Distance is measured from the deformation-front and the location of the coastline is shown for reference.

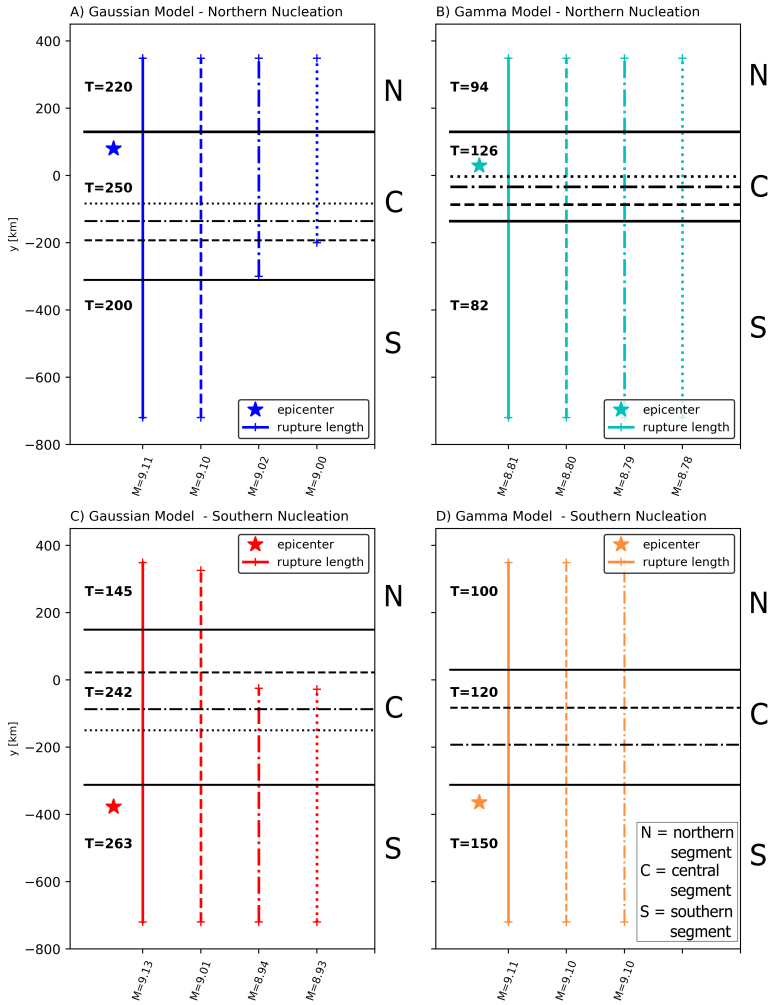

Figure 3.8: Gaussian and Gamma dynamic rupture simulations nucleated in northern or southern Cascadia (colored star). In each plot, the line length corresponds to the along-strike rupture extent. The line style corresponds to the variable segment location. A) Gaussian ruptures where the width of the central segment (also contains the nucleation asperity) is varied until margin-wide slip no longer occurs. The T levels (relative dynamic stress-drop) remains constant for each simulation. B) Same idea as A but for Gamma rupture simulations. The higher stress-drop at shallower depths provides enough energy for ruptures to easily span the entire Cascadia margin. Moment-magnitude is plotted along the x-axis on all plots. C) and D) show Gaussian and Gamma ruptures nucleated in southern Cascadia, respectively. For each subfigure, the Northern (N), central (C), or southern (S) segment regions are denoted.

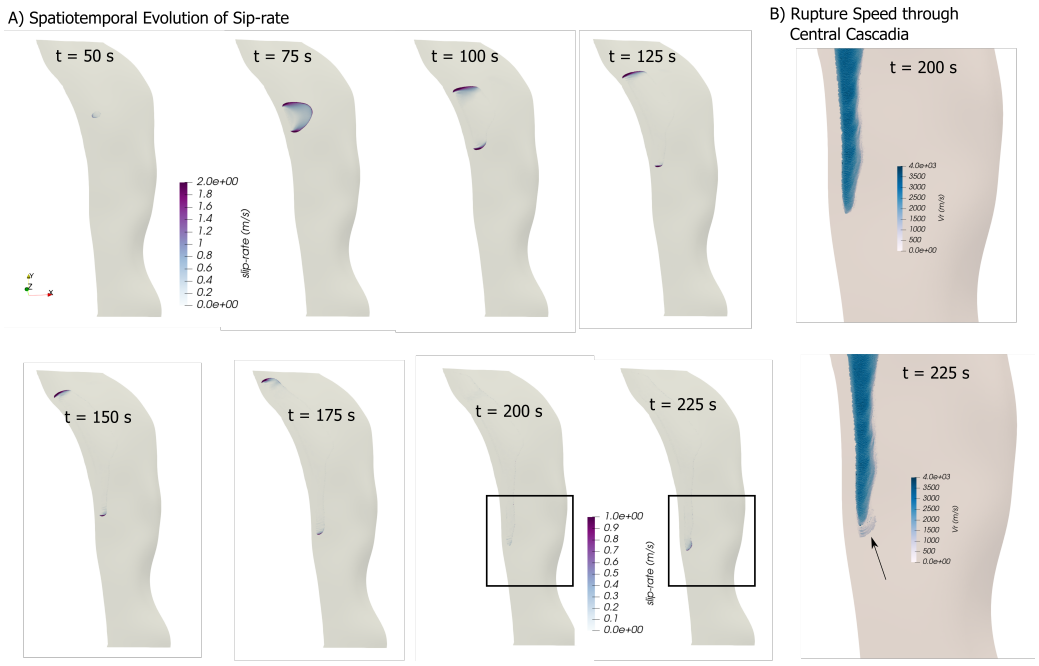

Figure 3.9: Slow rupture speed of Gamma models. A) Snapshots of the slip-rate at 25 second increments. Black box denotes zoom-in shown in B. B) Rupture velocity at the last two time steps to show how the rupture can dramatically slow down in the central Cascadia region.

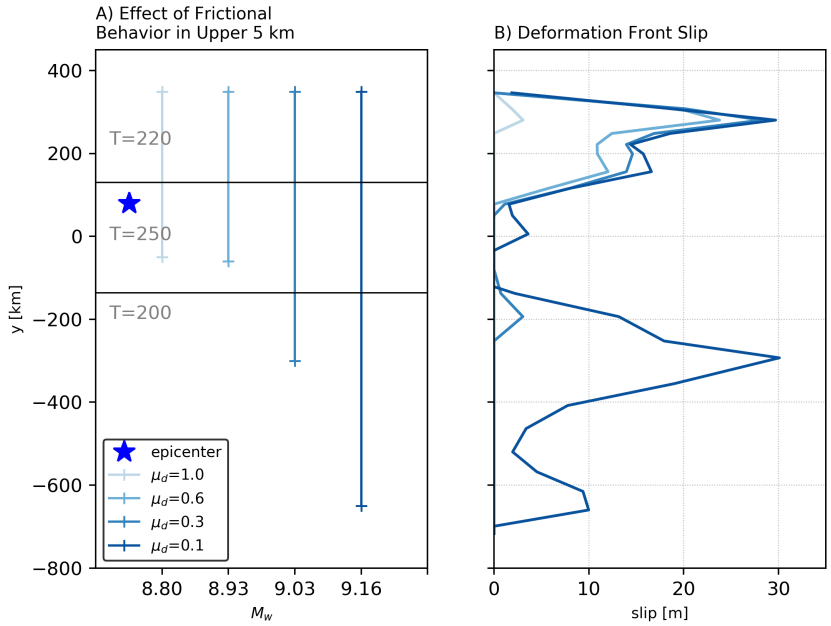

Figure 3.10: Gaussian coupling models with variable sediment frictional behavior in the upper 5 km of the megathrust. A) Along-strike rupture lengths (colored lines) as function of dynamic friction coefficient. B) Slip at the deformation-front for each scenario shown in A.

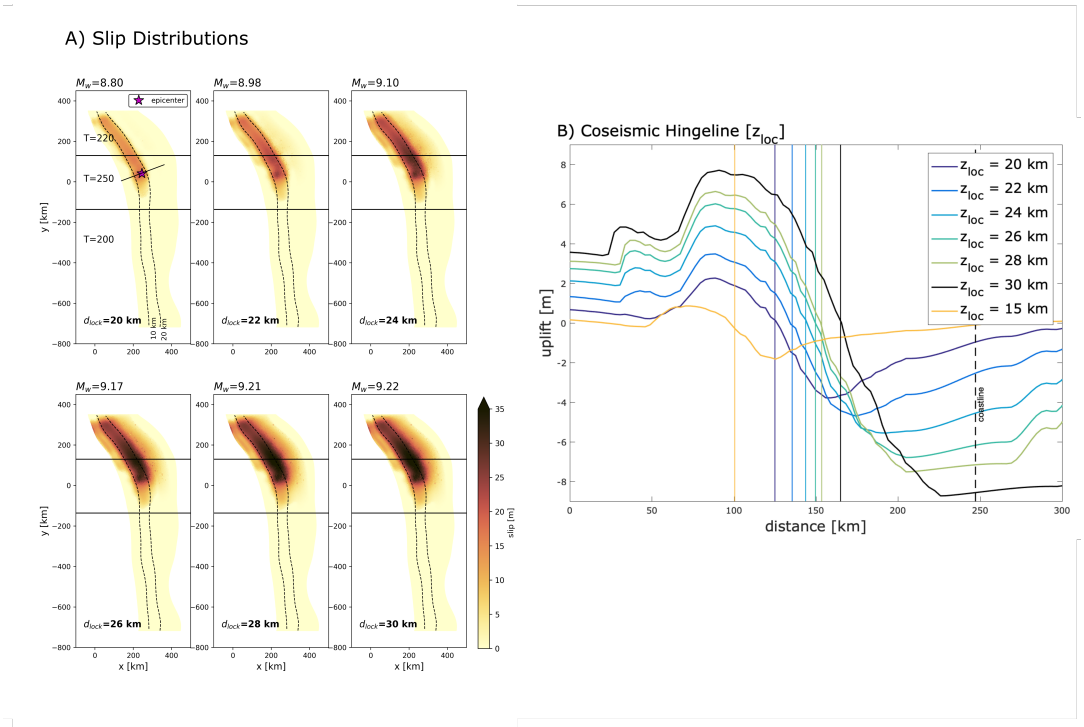

Figure 3.11: Effect of down-dip locking depth on coseismic slip distribution and uplift/subsidence patterns. A) Final slip distributions for the Gaussian coupling model nucleated in northern Cascadia. The earthquake is nucleated at the red star and a profile of uplift/subsidence at the free-surface is plotted in figure B (black line through red star). In each panel, the locking depth is systematically deepened by 2 km. B) Model-predicted coseismic subsidence and uplift for the range of locking depths studied. The coastline is plotted for reference near 250 km from the deformation front. Each solid line represents the coseismic hinge-line and is colored by its respective locking depth. We also show a shallower locking depth (15 km) in yellow to illustrate how such an assumption changes the amplitude and gradient of coseismic deformation.

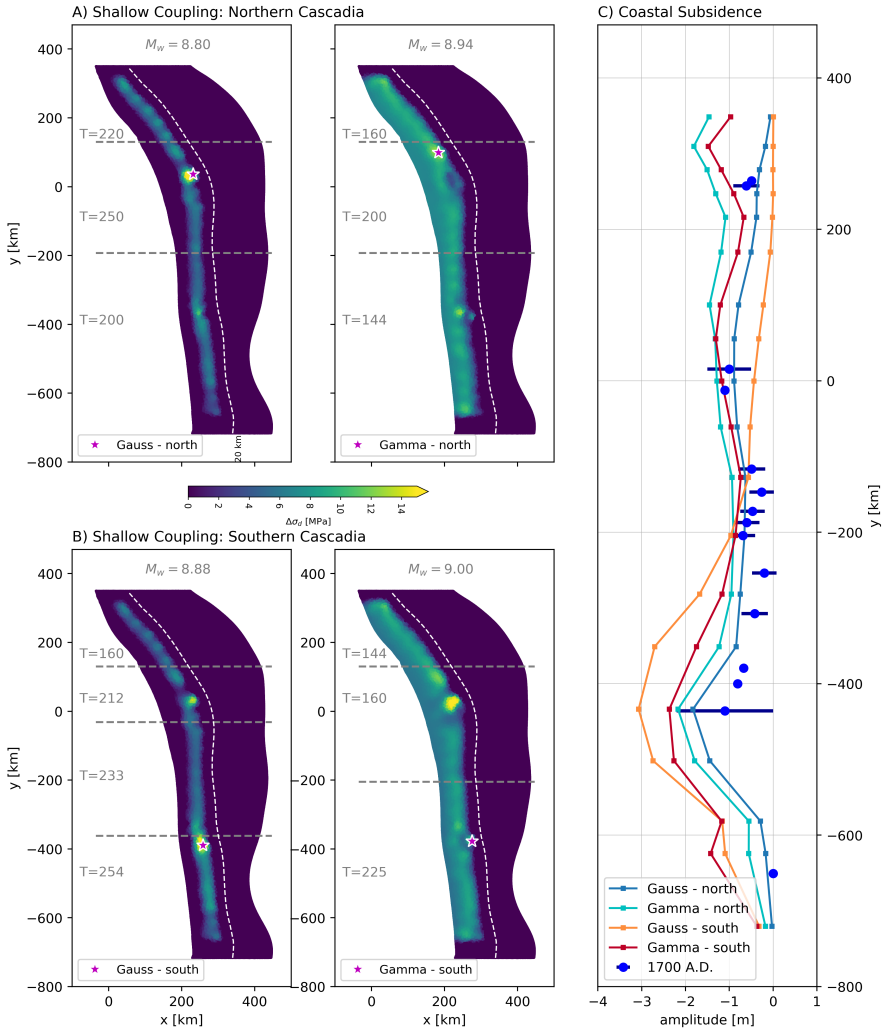

Figure 3.12: Gaussian and Gamma coupling models with shallow locking depth (15 km) that match coastal 1700 A.D. subsidence measurements to first order. A) Ruptures nucleated in northern Cascadia. B) Ruptures nucleated in southern Cascadia. C) comparison of predicted coastal subsidence from simulations shown in A and B.

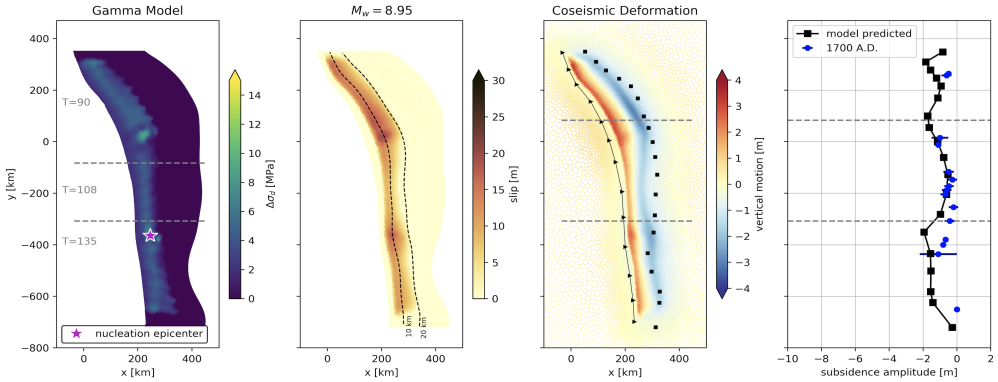

Figure 3.13: Deeper locking depth (20 km) alternative to fitting 1700 A.D. subsidence. A) Gamma coupling model dynamic stress-drop distribution. B) Final slip distribution. C) Predicted uplift and subsidence. D) Along-strike subsidence comparison between modeled (black) and 1700 A.D. observations (blue).

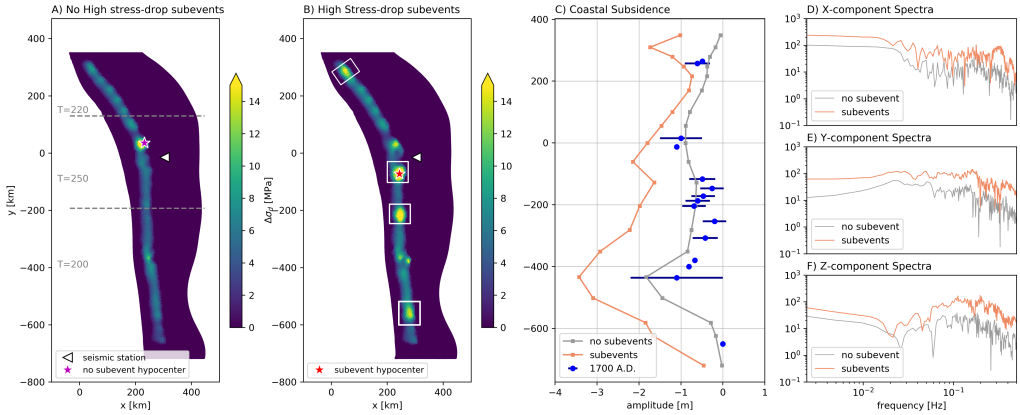

Figure 3.14: Comparison between dynamic rupture simulations with and without high dynamic stress-drop subevents positioned near the down-dip edge of locking ($\sim$15 km) along-strike. A) Gaussian dynamic stress-drop distribution without subevents. White triangle denotes synthetic seismogram receiver. B) Gaussian dynamic stress-drop distribution with superposed $\sim$15 – 20 MPa subevents. C) Coastal subsidence for both models with 1700 A.D. observations for comparison. D), F), and E) show the raw spectral amplitudes of the x-, y-, and z-components, respectively. The influence of the subevents is to increase the high-frequency amplitudes recorded (bold colored lines). D) and E) show (normalized) synthetic seismograms near the epicenter for dynamic rupture models excluding and including high stress-drop subevents.

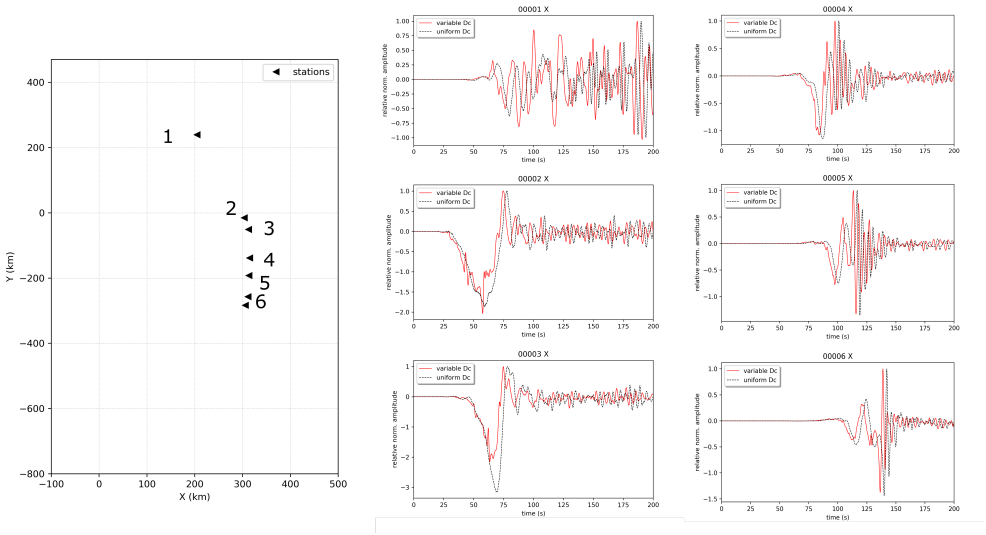

Figure 3.15: Effect of heterogeneous Dc at some seiesmic stations along the coast.

CHAPTER IV

Stress Changes on the Garlock Fault during and after the 2019 Ridgecrest Sequence *

Abstract

The recent 2019 Ridgecrest earthquake sequence in southern California jostled the seismological community by revealing a complex and cascading foreshock series that culminated in a M_w 7.1 mainshock. But the central Garlock fault, despite being located immediately south of this sequence, did not coseismically fail. Instead, the Garlock fault underwent postseismic creep and exhibited a sizeable earthquake swarm. The dynamic details of the rupture process during the mainshock are largely unknown, as is the amount of stress needed to bring the Garlock fault to failure. We present an integrated view of how stresses changed on the Garlock fault during and after the mainshock using a combination of tools including kinematic slip inversion, Coulomb stress change (ΔCFS), and dynamic rupture modeling. We show that positive ΔCFS cannot easily explain observed aftershock patterns on the Garlock fault but are consistent with where creep was documented on the central Garlock fault section. Our dynamic model is able to reproduce the main slip asperities and kinematically estimated rupture speeds ($\leq$ 2 km/s) during the mainshock, and suggests the temporal changes in normal and shear stress on the Garlock fault were the greatest near the end of rupture. The largest static and dynamic stress changes on the Garlock fault we observe from our models coincide with the creeping region, suggesting that positive stress perturbations could have caused this during or after the mainshock rupture. This analysis of near-field stress-change evolution gives insight into how the Ridgecrest sequence influenced the local stress field of the northernmost eastern California shear zone.

*Chapter IV is published in *Bulletin of the Seismological Society of America*: Ramos, M. D.., et al. "Stress Changes on the Garlock Fault during and after the 2019 Ridgecrest Sequence." Bulletin of the Seismological Society of America. 110. 4 (2020).

4.1 Introduction

The 2019 Ridgecrest earthquake sequence involved the rupture of a left-lateral M_w 6.4 foreshock that occurred on 4 July and a right-lateral M_w 7.1 mainshock that occurred on 6 July and initiated approximately 13 km northwest of the foreshock epicenter (Figure 4.1). This sequence was characterized by the activation of multiple orthogonal fault segments that are collectively referred to as the Little Lake fault zone (Llfz). Coseismic rupture of these faults continues to produce after- shocks, but it did not influence the adjacent left-lateral Garlock fault to fail. Instead, this sequence caused as much as three centimeters of surface creep on the Garlock fault that has been detected geodetically (*Barnhart et al.*, 2019; *Ross et al.*, 2019).

Several kinematic slip models have been developed to estimate the evolution of slip and rupture propagation during this highly complex sequence (*Barnhart et al.*, 2019; *Liu et al.*, 2019; *Ross et al.*, 2019; *Chen et al.*, 2020; *Goldberg et al.*, 2020; *Zhang et al.*, 2020). These models are consistent in the respect that a majority of foreshock and mainshock slip is limited to the upper 10 km depth. Positive stress-change amplitudes ($\sim$5 MPa) suggested by static Coulomb modeling generally coincide with the $\sim$25-kilometer-long region of creep on the central Garlock fault segment (*Barnhart et al.*, 2019). But the dynamic details of rupture and how stresses were mediated by the seismic wavefield remain hazy. The Garlock fault was apparently not near critical failure, or else we would have observed coseismic rupture there as well; this implies that the stress perturbations were unable to bring shear stresses to overcome the static Garlock fault strength.

When the Garlock fault will slip again is a major unknown. The Garlock fault extends for $\sim$260 km and is geometrically segmented into western, central, and eastern sections that are characterized by variations in geologic slip rate and recurrence interval (*Hill*, 1953; *Davis*, 1973; *McGill*, 2009). *Astiz, L., Allen, C. R.* (1983) analyzed historical seismicity on this fault and hypothesized that a rupture on the eastern Garlock segment may be more likely given its apparent seismic gap, though both the central and western sections can independently support M_w 7 earthquakes. Paleoseismic evidence suggests historic, nonperiodic surface rupture for the central Garlock segment (*Dawson et al.*, 2003). During the Ridgecrest sequence, different regions of the central Garlock fault segment experienced a swarm of low-magnitude earthquakes (ML $<$ 3.2; *Ross et al.* (2019) and underwent creep. How the strain accumulation budget of the central Garlock fault was influenced by the recent Ridgecrest sequence is enigmatic and warrants further scrutiny for seismic hazard analysis. A spatial separation between the Ridgecrest mainshock and Garlock fault planes is furthermore subject to uncertainty, as is the possibility of rupture branching from a segment

of the Garlock fault onto an adjacent segment or to the San Andreas fault during a future earthquake. In particular, the central and western segments have co-ruptured within the last 10 ka, despite a stepover structure in between them (*Madugo et al.*, 2012). Assessing the possibility of how close the Garlock fault is to failure depends on both the static and dynamic stress perturbations from the Ridgecrest sequence.

We aim to present a physically consistent picture of the stress interaction vis-à-vis the Garlock fault during and after the Ridgecrest sequence. We draw from updated kinematic inversion results that utilize geodetic, teleseismic, and near-field strong ground motion recordings to independently constrain the fault-slip amplitude, extent, and rupture initiation locations of the fore-shocks and M_w 7.1 mainshock. This is then used to inform our static Coulomb stress analysis and dynamic rupture modeling efforts. Our analysis illustrates that both normal and shear stress changes were the highest on the Garlock fault at the end of main- shock rupture, and could have been responsible for the observed geodetic creep as soon as 30 s from mainshock rupture initiation.

4.2 Methodology

4.2.1 Kinematic slip inversion

We use a joint slip-inversion model that is based on static Global Positioning System (GPS), teleseismic, and local strong ground motion datasets (*Ji*, 2002). The M_w 6.4 foreshock and the M_w 7.1 mainshock are modeled with two- and single- fault plane geometries, respectively (Figure 4.1). Slip along the mainshock fault occurs along a 100-kilometer-long segment that dips at $\sim$88 degrees (Figure 4.1). Of the two foreshock fault planes, one is nearly parallel to the strike of the mainshock (plane 1), whereas the second is perpendicular to the mainshock (plane 2; Figure 4.1; Table 4.1). These fault plane geometries are consistent with those estimated by the U.S. Geological Survey and do not extend deeper than 16 km depth. Geologic mapping and Interferometric Synthetic Aperture Radar (InSAR) observations of surface-breaching rupture strands during the Ridgecrest sequence suggest that our geometries are reasonable (*Xu et al.*, 2020). We use the slip-inversion results for the foreshock and mainshock fault planes as input into our static and dynamic stress-change modeling.

4.2.2 Static model: Coulomb stress change

Static stress changes are the final changes in the normal and shear stresses on the fault in response to slip after all seismic waves have propagated through. Such stress changes during the foreshock and mainshock of the Ridgecrest sequence have triggered thousands of aftershocks (*Ross et al.*, 2019). Coseismic stress changes have also been known to enhance or to reduce creep after the earthquake (e.g., *Allen*, 1972; *Bodin*, 1994; *Lienkaemper*, 1997). *Barnhart et al.* (2019) observed that an increase in the Coulomb stress change (ΔCFS) from the Ridgecrest earthquake was correlated with the surface deformation after the earthquake. Studies have also suggested that the M_w 6.4 foreshock and other large foreshocks promoted the rupture of the mainshock (*Barnhart et al.*, 2019; *Goldberg et al.*, 2020; *Lozos and Harris*, 2020).

To assess static stress changes, we calculate the ΔCFS using the Coulomb 3 software (*Lin*, 109; *Toda et al.*, 2005). We investigate the ΔCFS caused by the foreshock on the main-shock and separate the contribution of stress change from each of the two foreshock fault planes (Plane 1 and Plane 2; Figure 4.2). We use a friction coefficient of 0.6 and a depth of 5 km for the foreshock–mainshock static stress-change calculation because a majority of slip is resolved on foreshock plane 2 (Figure 4.1, which will dominate the ΔCFS amplitude.

We also calculate the ΔCFS due to mainshock slip on the Garlock fault. We represent the Garlock fault geometry as a plane with a strike, dip, and rake of 70°, 90°, and 0°, respectively. The strike of the Garlock fault varies from 68° in the east to 84° in the west (Figure 4.3), but we use 70° for the receiver fault as it is the closest to the strike of the western Garlock fault segment where the cluster of aftershocks occurred. Lastly, to address uncertainty in static friction level and hypocenter depth, we also examine how varying these parameters influences our results. We compare the results from friction coefficients of 0.2, 0.4, and 0.6, and at 5 km depth, where peak slip occurred, and at 10 km depth, where the asperity with most slip extends.

4.2.3 Dynamic model: Initial conditions and constraints

We model the mainshock fault plane as a 100 km, planar 2D crack embedded in a homogeneous, isotropic, and linearly elastic medium with a shear wavespeed of 3.2 km/s. The model domain is composed of rectangular elements enclosed on all sides by absorbing boundaries. We choose a finite-element size of 600 m with four Gauss–Lobatto–Legendre nodes to resolve dynamic rupture propagation at seismic frequencies up to 1 Hz for consistency with that resolved by the strong-motion dataset.

We select the linear slip-weakening friction law to control fault-slip evolution and utilize the 2D spectral element code SEM2DPACK to solve for dynamic rupture propagation (*Ampuero*, 2009). The critical-slip distance (Dc) is 0.3 m, which is constant along the fault (except for 15 km around the nucleation region) and is within the plausible range of previous slip-weakening dynamic rupture simulations for other crustal earthquakes of comparable magnitude and rupture dimension (e.g., *Ma and Archuleta*, 2006; *Tinti et al.*, 2009; *Lozos and Harris*, 2020). If dynamic friction (μ_d) is below the static friction (μ_s) level, then the fault experiences a strength drop during coseismic rupture and its frictional behavior is slip-weakening; conversely, if the dynamic friction is greater than static friction, there is no work available to grow the propagating shear crack and the frictional behavior is slip strengthening. The static friction coefficient is 0.5 everywhere along the fault. The fault is slip-weakening (μ_d = 0.1) along the central 70 km segment (35 km southeast and northwest of hypocenter) and slip strengthening (μ_d = 0.7) everywhere else to prohibit rupture from breaking the entire fault.

Given that we represent a strike-slip fault as a mode II in-plane crack, our stress and friction conditions are relative to a region on the mainshock fault plane at depth. Our model aims to reproduce the rupture propagation along the section of the fault that crosses through the main slip asperity imaged in the kinematic inversion (Figure 4.4). Effective normal stress is set to a constant level of 50 MPa that is consistent with elevated pore-pressure levels in the middle of permeable fault zones (*Rice*, 1992).

The initial shear stress distribution is a critical ingredient for any dynamic earthquake rupture model and determines the dynamic stress drop which in turn governs slip amplitude. We first calculate the static stress drop due to fault slip given by the kinematic inversion using a computationally efficient algorithm (Figure 4.4; *Ripperger and Mai* (2004). Earthquakes can exhibit total or near-total stress drop due to strong dynamic weakening (e.g., *Noda and Lapusta*, 2013; *Brodsky et al.*, 2020), meaning that the final shear stress on the fault after an earthquake is at or very near its dynamic fault strength level (the product of effective normal stress and dynamic friction). We make this assumption to calculate our initial shear stress by adding the static stress drop to the dynamic fault strength (Figure 4.4).

Rupture is artificially nucleated in the middle of the fault using the time-weakening method (*Andrews*, 1985). This technique requires twice the critical half-crack length ($2L_c$), an effective friction level (μ_o), and a weakening timescale (Tc) after which the prescribed nucleation is turned off and rupture spontaneously evolves according to the nonlinear interaction between fault strengths and stresses. Given the friction law parameters we assume for mode II rupture in an elastic domain, $2L_c$ is given by

$$2L_c = \frac{2}{1-v}\frac{G}{\pi}\frac{\tau_s - \tau_d}{(\tau_o - \tau_d)^2}D_c \tag{4.1}$$

in which G is the shear modulus (30 GPa), v is the Poisson's ratio, τ_s is the static fault strength, τ_d is the dynamic fault strength, τ_o is the initial shear stress, and μ_o is the effective friction coefficient calculated as the ratio between initial shear and effective normal stress amplitudes at the hypocenter. We determined that a $2L_c$ of 2 km (μ_o ~0.1) and Tc of 10 s are necessary to nucleate and sustain spontaneous rupture.

4.3 Results

4.3.1 Kinematic slip inversion

Using our kinematic inversion methodology, the mainshock hypocenter has been relocated to a depth of 3 km by the arrival times of nearby strong-motion and broadband seismic stations (Figure 4.1). The aftershock hypocenter is deeper (9 km) and slip is distributed across two fault segments (Figure 4.1). The fault parameters and hypocenters of both earthquakes are summarized in Table 4.1. We note that the M_w 7.1 mainshock ruptured bilaterally with a majority of slip concentrated within the upper 10 km and a peak slip amplitude of 4.7 m located ~10 km northwest of the hypocenter (Figure 4.1). There is a smaller asperity that underwent ~2.5 m of slip southeast of the mainshock hypocenter, as well. On the other hand, peak slip resolved for the foreshock is lower (1.3 m) and occurred mostly on plane 2, which is perpendicular to the mainshock fault plane (Figure 4.1).

We also compare our mainshock slip-inversion results with those from other studies of the Ridgecrest mainshock. We utilize seismic and GPS datasets to constrain the slip, which is similar to the approach by (*Liu et al.*, 2019). In contrast, other studies make use of a combination of seismic, high-rate GPS and InSAR (*Ross et al.*, 2019; *Chen et al.*, 2020; *Goldberg et al.*, 2020), InSAR and optimal image tracking (*Barnhart et al.*, 2019), or only seismic datasets (*Zhang et al.*, 2020). The details of slip distribution, and in particular the relative location and amplitude of maximum slip, varies between studies. The maximum slip is mostly shallower (~4 km, *Barnhart et al.* (2019), to the northwest of (~10 km, (*Liu et al.*, 2019), or slightly deeper (~5 km, *Ross et al.* (2019) than the hypocenter location used in their inversion. The kinematic slip inversion we present resolves two primary slip patches (i.e., Figure 4.1), which have similar amplitudes (4.7 and 2.5 m) and locations (northwest and southeast of hypocenter) to the *Barnhart et al.* (2019), *Liu et al.* (2019),and *Zhang et al.* (2020) inversion results. A major difference in maximum slip amplitude occurs between our model and the *Ross et al.* (2019) study, which estimates as much as 9 m of

slip between 5 and 10 km depth. Other notable changes between our study and other's include a more widely distributed higher (4 m) slip distribution (*Chen et al.*, 2020), or a maximum slip amplitude difference on the order of 1.5 m between what is resolved from our inversion (4.7 m) and the *Goldberg et al.* (2020) [$\sim$3.5 m] study. Such differences are most likely due to the datasets used to constrain the inversions as well as the particular inversion parameterization. Overall, our mainshock slip distribution is consistent with other published models, characterized by bilateral rupture propagation and a shallow ($<$ 10 km) slip distribution.

4.3.2 Static stress change

We find the foreshock increased the ΔCFS near the edges of the foreshock faults, especially at the intersection of plane 2 and mainshock fault, but our relocated mainshock hypocenter is located in a region of slightly decreased ΔCFS (Figure 4.2). However, this result depends on the method used to locate the mainshock hypocenter and its uncertainty. For instance, the Advanced National Seismic System (ANSS) comprehensive catalog epicentral coordinates agree with ours to within a kilometer but its depth is 5 km deeper than our preferred depth of 3 km, whereas the hypocenter resolved by *Ross et al.* (2019) is $\sim$12 km away from the foreshock hypocenter but at a similar shallow depth ($<$4 km). The hypocenters estimated by the ANSS catalog and by *Ross et al.* (2019) are located near the edges of different regions of positive ΔCFS. We also calculated the ΔCFS from both foreshock planes separately (Figure 4.2). Plane 2 has a much larger slip compared with plane 1, with almost twice the peak slip (i.e., 1.3 vs. 0.74 m; Table 4.1). However, plane 1 causes an $\sim$0.5 MPa greater ΔCFS on the southeast region of the mainshock fault compared with plane 2, as plane 1 is closer (Figure 4.2). This underscores the sensitivities of the ΔCFS to input fault-slip amplitude and extent.

We further calculate the ΔCFS on the Garlock fault due to mainshock slip and assess the effect of various friction coefficients and depths on our results. Overall, we find that the friction coefficient has a relatively small (i.e., a difference within $\sim$0.1 MPa) impact on our ΔCFS results for a given depth (Figure 4.3). Larger friction coefficients tend to increase the ΔCFS amplitude and changes the spatial distribution of positive and negative stress changes (Figure 4.3). This is similar to *Barnhart et al.* (2019), in which they found that their results are consistent for all friction coefficients that they tested. For a given friction coefficient, changing the depth of the ΔCFS calculation from 5 to 10 km increases the ΔCFS amplitude by $\sim$0.3 MPa and decreases the extent of the region of positive ΔCFS on the Garlock fault by approximately 20 km (Figure 4.3). The amplitude difference is

because the largest portion of mainshock slip extends to about 10 km depth, and the change in slip at this depth produces a larger ΔCFS than at 5 km depth. The region of positive ΔCFS in proximity to the creeping section of the Garlock fault is most consistent in spatial extent with that of *Barnhart et al.* (2019) when we use a friction coefficient of 0.2 and a depth of 5 km. Lastly, we find that the cluster of aftershocks on the Garlock fault are unlikely to be simply explained by ΔCFS from the mainshock as the value of the stress change can be small ($<$0.01 MPa) or even negative ($\sim$0.1 MPa) [Figure 4.3].

4.3.3 Dynamic earthquake rupture model

Our first goal is to explain the kinematic fault-slip distribution using rupture dynamics. We seek to reproduce the two primary patches of 2.5 and 4.7 m slip southeast and northwest of the hypocenter, respectively, (Figures 4.1 and 4.5). We show the rupture history until 35 s to highlight the arrest of both the northwest and southeast rupture fronts (Figure 4.5).

The initial conditions and friction parameters outlined in the Methodology section gives a good agreement between the kinematically imaged and dynamically modeled slip distributions. The exception is the region near the hypocenter, where the dynamic rupture model overpredicts the kinematic slip amplitude by $\sim$0.8 m (Figure 4.5). This is most likely due to our time-weakening nucleation procedure but is probably within the uncertainty of the true fault slip resolved by the kinematic inversion. The distribution in dynamic stress drop is positive for which higher slip is concentrated, and negative in a small region southeast of the hypocenter and where we impose slip-strengthening frictional behavior at the ends of the fault (Figure 4.5).

The bilateral mainshock dynamic rupture is overall heterogeneous and spatiotemporally complex (Figure 4.5). There are three major asperities (i.e., relatively high dynamic stress-drop regions) that contribute to several rupture-front accelerations (Figure 4.5). The model shows a slow ($<$ 1 km/s) rupture front propagating to the southeast for the first 5 s after nucleation ceases; this southeast rupture front then accelerates to $<$ 1.3 km/s before decelerating and arresting at 28 s (Figure 4.5). In contrast, the northwest rupture front propagates at a more uniform speed ($<$ 2.1 km/s) before decelerating and stopping at $\sim$25 s. These rupture speeds are consistent with recent kinematic models that prescribe a constant sub-Rayleigh mainshock rupture speed (*Liu et al.*, 2019; *Ross et al.*, 2019; *Goldberg et al.*, 2020; *Zhang et al.*, 2020). Rupture speed depends on how much total available energy is partitioned into radiated or fracture energy during the faulting process. Slower ruptures (as observed during the Ridgecrest sequence) may be due to a relatively high fracture energy consumed on the fault, consistent with the hypothesis that the Llfz is less compliant

and more energy was needed to break multiple fault segments (*Perrin, C., Manighetti, I., Ampuero, J. P., Cappa, F., Gaudemer*, 2016; *Liu et al.*, 2019; *Goldberg et al.*, 2020). Our dynamic model shows that the mainshock rupture fronts do not exhibit slip-rate amplitudes above 4 m/s and propagate at well below the Rayleigh wavespeed.

4.3.4 Temporal stress changes on the Garlock fault

Using our dynamic rupture model, we investigate the stress contributions to a section of the central Garlock fault during and after the Ridgecrest mainshock. Given the limitation of our modeling domain, we cannot assess far-field dynamic stress contributions from surface-wave amplitude changes. We instead focus on how the initial peak stresses carried by near-field seismic waves impacted the Garlock fault during coseismic rupture.

The 2D stress tensor in our model is for an isotropic body and yields three unique components: σ_{xx}, σ_{yy}, and σ_{xy}. Only one component of the normal stress (σ_{yy}) and the shear stress (σ_{xy}) are important to be considered further in our analysis. If we place the strike of the mainshock fault plane on an east–west coordinate system, the angle between the mainshock and Garlock fault planes (measured clockwise) is approximately 110°. We therefore applied a rotation of the stress field at a particular instant in time to represent the stress perturbation the mainshock imparts to the Garlock fault (Figure 4.6). When this rotation is performed at the final timestep, the rotated stress field is equivalent to the static stress change on the Garlock fault. We observe an abrupt transition from negative to positive normal static stress change as one crosses the intersection of the strike of the mainshock fault plane (Figure 4.6). The shear stress change is slightly more complex with an asymmetric stress amplitude distribution across the fault, but shows a very pronounced region of positive stress change that generally coincides with the ∼25-kilometer-long section of the central Garlock fault that underwent creep (*Barnhart et al.*, 2019; *Xu et al.*, 2020). To confirm our static stress-change analysis from the dynamic model, we compare it with our ΔCFS calculation and find that its orientation and amplitude are consistent.

We also calculate the temporal stress change on the central Garlock fault segment during the Ridgecrest mainshock. We select one point near the creeping region on the Garlock fault (∼60 km, ∼10 km; Figures 4.7 and 4.8) to show how normal and shear stresses change during mainshock rupture. Although propagation spontaneously arrests at near ∼28 s toward the southeast, we simulate rupture until 100 s to make sure stress changes relax to constant levels, which are attained at 60 s (Figure 4.9). This section of the central Garlock fault begins to experience a positive normal stress change near 17.5 s (Figure 4.7). During the main portion of coseismic rupture, normal stress changes reach their maximum of ∼0.3

MPa at 32 s (Figures Figures 4.7 and 4.9). In contrast, positive shear stress changes arrive at the Garlock fault in three distinct pulses (e.g., Figures 4.8 and 4.9). Two of these positive shear stress-change pulses arrive after the largest change in normal stress change and continue to be above the normal stress-change amplitude for the remainder of our simulation (Figures Figures 4.8 and 4.9). The extrema of the normal and shear stress-change amplitudes are symmetric through time due to the alternating arrivals of compressional-wave (P) and shear-wave (SV) motions

4.4 Discussion and Conclusion

We show that stress changes during and after the Ridgecrest foreshocks and mainshock may have influenced postseismic creep on the central Garlock fault segment and brought certain regions potentially closer to coseismic failure. Our results also shed light on the temporal stress evolution on the Garlock fault due to source dynamics. Because both normal and shear stresses vary during coseismic rupture, evaluating their respective contribution is of critical importance to identifying periods when stress changes may have been favorable to engender the observed postseismic creep.

The ΔCFS results show that positive static stress changes were experienced on the central Garlock fault due to mainshock slip (Figure 4.3) and are coincident with previously documented fault creep (*Barnhart et al.*, 2019; *Ross et al.*, 2019; *Xu et al.*, 2020). Among ΔCFS calculated for different friction levels and depths, in only one case (i.e., friction level of 0.6) is a positive static stress change on the order of $\sim$0.1 MPa observed adjacent to the region of the Garlock fault that experienced a sizeable aftershock swarm (Figure 4.3). This may indicate that other postseismic relaxation processes or dynamic stress changes were at play to produce this aftershock pattern. Various studies have also calculated the ΔCFS of the foreshock at the mainshock hypocenter with their slip-inversion results. While *Barnhart et al.* (2019) found an increase in ΔCFS of 0.6 MPa due to the foreshock at their hypocenter, *Zhang et al.* (2020) found an increase of 0.04 MPa and *Goldberg et al.* (2020) found a $<$0.1 MPa increase. We find a 0.1 MPa decrease in ΔCFS at the location of our hypocenter. The disparity in magnitude and sign of the results may be due to the fact that Coulomb stress calculations are very sensitive to the slip-inversion model used and the inferences may change depending on the location of the hypocenter, as well.

When we assess the ΔCFS through time we find that ΔCFS predominantly increases during mainshock rupture and remains at a high level afterward; this is evident from our dynamic model as the normal stress-change amplitude is mostly below the shear stress amplitude (Figure 4.9). Temporal stress changes during the mainshock rupture also support

predominantly positive shear stress changes near this creeping Garlock region (Figure 4.8), whereas positive and negative normal stress distributions are observed on both sides of the fault (Figure 4.7). Our results for temporal normal and shear stress changes near the Garlock fault agree with other dynamic rupture simulations that prescribe a complex 3D fault geometry but similar constitutive friction law parameters (*Lozos and Harris*, 2020). Moreover, this study also documents a detailed temporal evolution of normal, shear, and Coulomb stresses impacting the central Garlock fault (i.e., Figure 4.9), and not just the final stress changes after all seismic waves have been radiated away. Because positive normal stress changes serve to strengthen the fault whereas positive shear stresses should bring the fault closer to failure, our dynamic model offers one possible scenario that creep could have occurred as soon as 15 s after nucleation of the Ridgecrest mainshock when positive shear stresses began to arrive at the Garlock fault. However, this is speculative given that we do not have information on the absolute stress state of the Garlock fault prior to the aftershock.

Our dynamic model also suggests that the largest shear stress changes (0.3 - 0.4 MPa) arrived before and after the largest normal stress changes, but they are comparable in amplitude (Figures 4.7, 4.8,4.9). Given this maximum shear stress-change amplitude at a given time, we estimate approximately 0.1 cm of slip may have been triggered near the creeping section of the Garlock fault at a depth less than 1 km. We also test a model for which creep on the Garlock fault was exceptionally shallow *Schleicher* (2019), but the distribution of creep is more heterogeneous. We still obtain a similar amount of creep that is consistent with the shear stress-change amplitude. These estimates are lower than the maximum magnitude of resolved surface creep (i.e., 3 cm) documented earlier by *Barnhart et al.* (2019) and *Ross et al.* (2019), however. The creep magnitudes we estimate are furthermore only valid for a homogenous, Poisson solid and should be considered an upper bound for any given shear stress-change perturbation because our dynamic rupture model captures the region on the mainshock fault plane that experiences the greatest dynamic stress drop (7MPa; Figure 4.5). There is potential for more creep to be accommodated by successive near-field stress changes arriving at the Garlock fault during mainshock rupture, but this depends on the near-surface rheology and earthquake history of the central Garlock fault. In addition, we cannot rule out the possibility that the maximum resolvable creep was driven by cumulative or postseismic strain-rate changes not seen by satellite observations because the smallest observation window is at least five to six days after the mainshock (*Barnhart et al.*, 2019). But extensometer data imply that it did not extend very deep into the crust, regardless of how much triggered creep was (*Bilham and Castillo*, 2020).

The fact that the Garlock fault did not coseismically fail could be supported by theoretical considerations to the prestress state, rupture speed and fault orientation between

the mainshock and Garlock fault planes if they are connected (*Poliakov et al.*, 2002; *Kame et al.*, 2003). For a low angle of maximum horizontal shear stress (SHmax) with respect to the fault ($<$ 45 degrees), this prestress state encourages rupture to bifurcate towards the compressional side, whereas a higher angle ($>$ 45 degrees) predicts that the rupture along the extensional side is more favorable (*Poliakov et al.*, 2002). *Yang and Hauksson* (2013) inverted earthquake focal mechanisms in central and southern California, estimating the regional SHmax orientation lies between zero and five degrees east of North. Our dynamic rupture model predicts an average mainshock rupture-front to shear-wave speed ratio of 0.4. Given that the mainshock fault plane is approximately oriented 45 degrees west of North, such a low prestress orientation together with low rupture speed levels are not likely to encourage rupture propagation to the Garlock fault, if connected (*Kame et al.*, 2003). This mechanical argument, however, must be taken with a grain of salt considering changes in the local stress field orientation surrounding the M_w 7.1 mainshock due to the M_w 6.4, smaller foreshocks, and other seismicity. A detailed seismological analysis of foreshock and aftershock stress-tensor inversions will undoubtedly place stronger constraints on the SHmax orientation to the mainshock fault plane, and perhaps lend credence to theoretical expectations we have briefly discussed here.

One aspect we could continue to explore in greater detail is how a fully dynamic model incorporating segmented foreshock and mainshock fault planes changes the details of the temporal stress changes on the Garlock fault. Several kinematic studies are able to fit seismogeodetic data using a segmented fault model (e.g., *Goldberg et al.*, 2020; *Liu et al.*, 2019; *Ross et al.*, 2019).Given that the Ridgecrest sequence produced multiple orthogonal faulting with some ruptures breaking the surface while others not *Ross et al.* (2019), we would expect the temporal stress change to accordingly reflect this complexity. We note that the geometrically segmented 3-D dynamic fault model by *Lozos and Harris* (2020) yields static normal and shear stress changes on the Garlock fault that are consistent to first-order in sign and amplitude with our modelling efforts. There are small differences, but this is expected due to different initial stress parameterizations, velocity structure, and fault geometry for the mainshock and foreshock fault planes.

How the M_w6.4 foreshock and M_w7.1 mainshock Ridgecrest sequences changed the local stress field in Southern California is a crucial question to consider given the proximity of these events to other active faults (e.g., Garlock and San Andreas). Through a unique combination of kinematic, static, and dynamic modeling, we present a physically coherent picture of the stress changes on the central Garlock fault during and after the coseismic rupture of the M_w7.1 event. We find that positive stress changes near the creeping section of the Garlock fault are observed during and after coseismic rupture. We also show that

the greatest shear stress change was comparable to the greatest normal stress change, but arrived earlier during dynamic rupture; this may have promoted a section of the Garlock fault to creep even before the Ridgecrest mainshock finished slipping. Our dynamic models physically explain the resolved slip amplitude through the mainshock hypocenter and reproduce the low sub-Rayleigh rupture speeds previously suggested by kinematic rupture models.

Event	M_w	Hypocenter	Strike	Dip	Rake	Peak Slip (m)
Mainshock	7.1	35.772° N, 117.602° E, 3 km	322	81	-170	4.7
Foreshock	6.4	35.705° N, 117.506° E, 9 km	318	88	-172	1.3
			228	81	0	0.74

Table 4.1: Coulomb Stress-Change Parameters of the Mainshock and Aftershock Fault Planes

4.5 Figures - Chapter 4

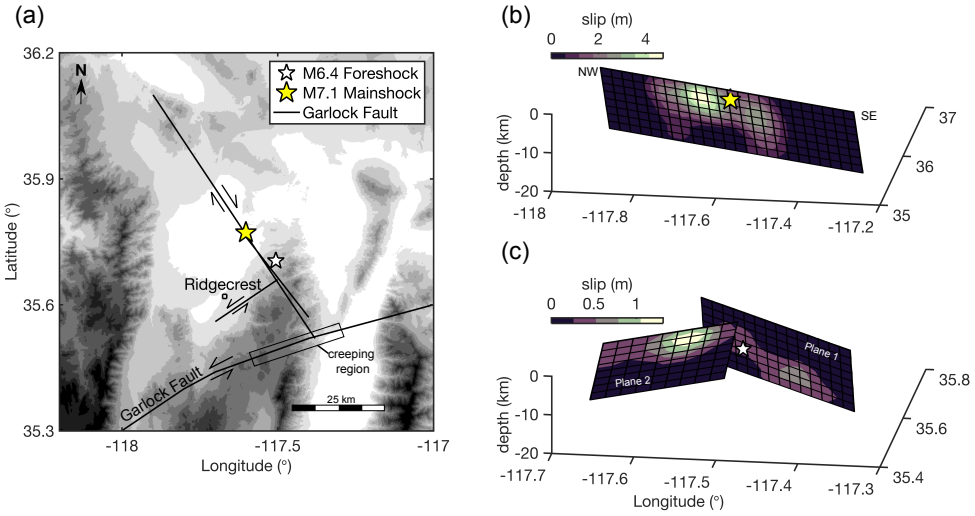

Figure 4.1: 2019 Ridgecrest earthquake sequence. (a) Study area with foreshock and mainshock fault planes denoted by solid lines. The approximate region of the central Garlock fault that experienced creep during this sequence is indicated by the box. (b) Mainshock slip-inversion results in which we determine a hypocenter depth of 3 km and a peak slip amplitude of 4.7 m that is immediately northwest (NW) of the hypocenter. (c) Foreshock slip-inversion results. Foreshock planes parallel and perpendicular to the mainshock fault plane are denoted as plane 1 and plane 2, respectively. Note that an NW–southeast (SE) fault orientation is the same for the mainshock and foreshock fault planes. Stars indicate (a) epicenter or (b,c) hypocenter locations.

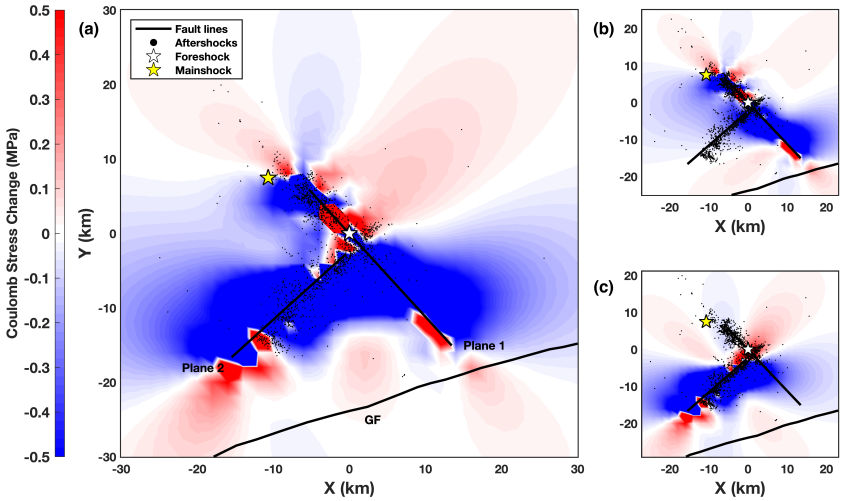

Figure 4.2: Coulomb stress change (ΔCFS) due to foreshock planes 1 and 2 on the mainshock fault plane calculated at a depth of 5 km and with a friction coefficient of 0.6. (a) The combined effect of both aftershock fault plane slip on the mainshock. (b) The ΔCFS from plane 1, which is parallel to the main fault plane. (c) ΔCFS from plane 2, which is the northeast–southwest-striking cross fault. The aftershocks depicted are the earthquakes that occurred after the foreshock and do not include those induced from mainshock stress changes. GF, Garlock fault.

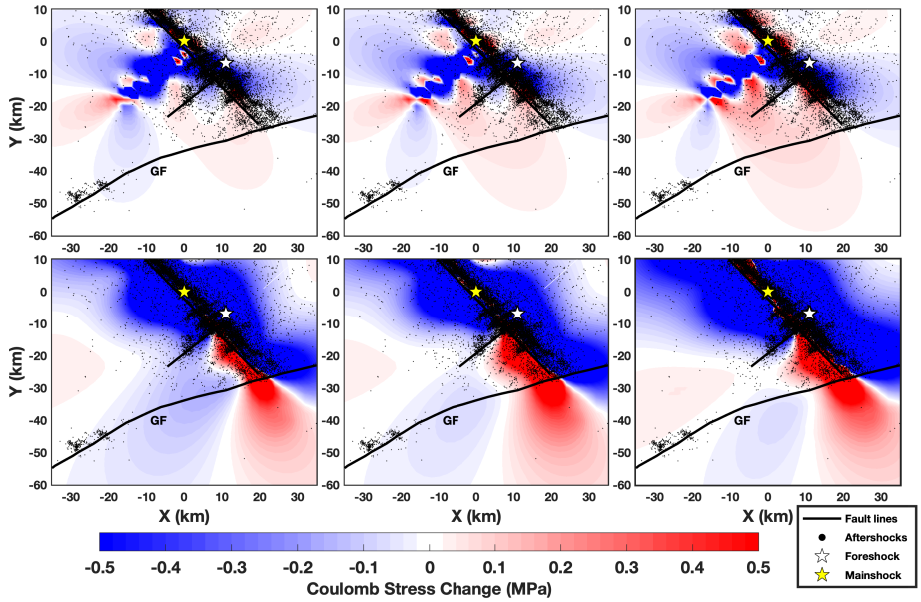

Figure 4.3: ΔCFS of the mainshock on a receiver fault of 70° strike and 90° dip, approximating the leftmost part of the Garlock fault in this figure. (Top) ΔCFS results for a 5 km depth source at friction coefficients of (left to right) 0.2, 0.4, and 0.6. (Bottom) ΔCFS results for a 10 km depth source with the same friction coefficients.

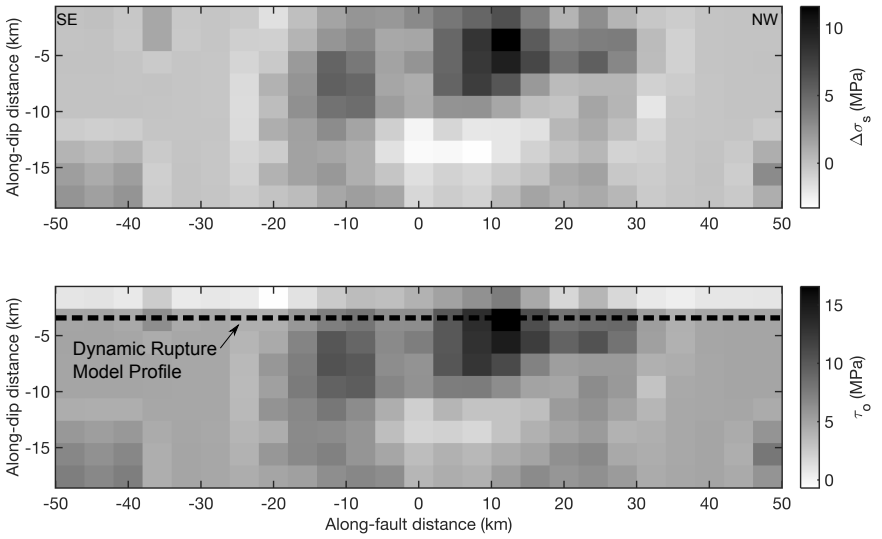

Figure 4.4: (a) Static stress drop and (b) initial shear stress along the mainshock fault plane. Static stress drop is calculated assuming a homogeneous Poisson medium and initial shear stress is computed using the complete stress-drop assumption. We select an initial shear stress profile through the main asperity at 3 km depth (dashed line) for our 2D dynamic rupture models.

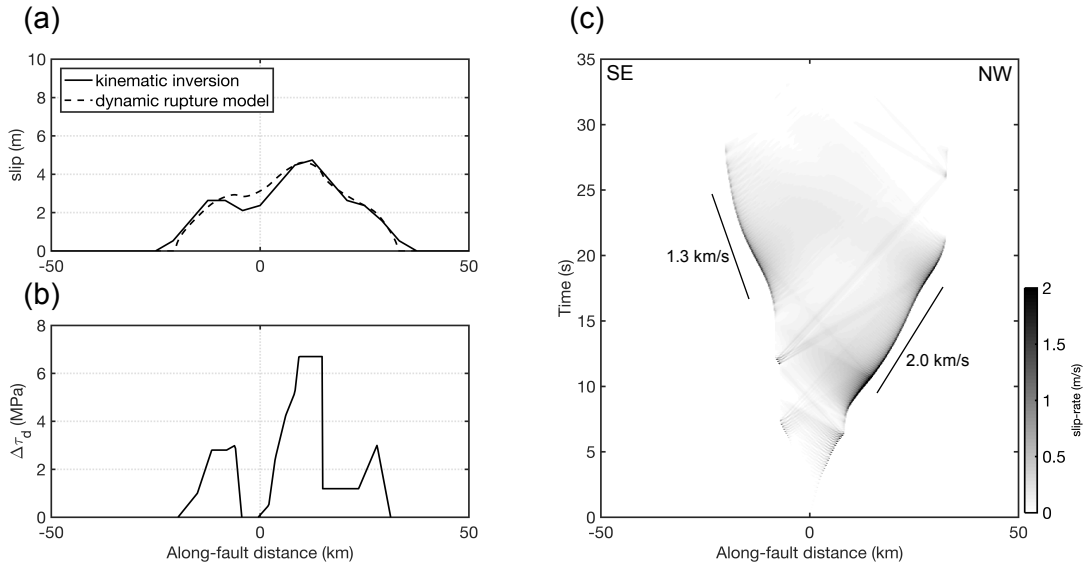

Figure 4.5: (a) Along-fault slip distribution resolved by the kinematic slip inversion (solid line) and that calculated from the dynamic rupture model (dashed line). The x-axis measures distance from where the earthquake is nucleated in our model. (b) Dynamic stress drop along the fault. Location shown in Figure 4. (c) Spatiotemporal and bilateral rupture history predicted by the dynamic rupture model. Solid lines signify average rupture-front speed. Both rupture fronts propagate at sub-Rayleigh wavespeed.

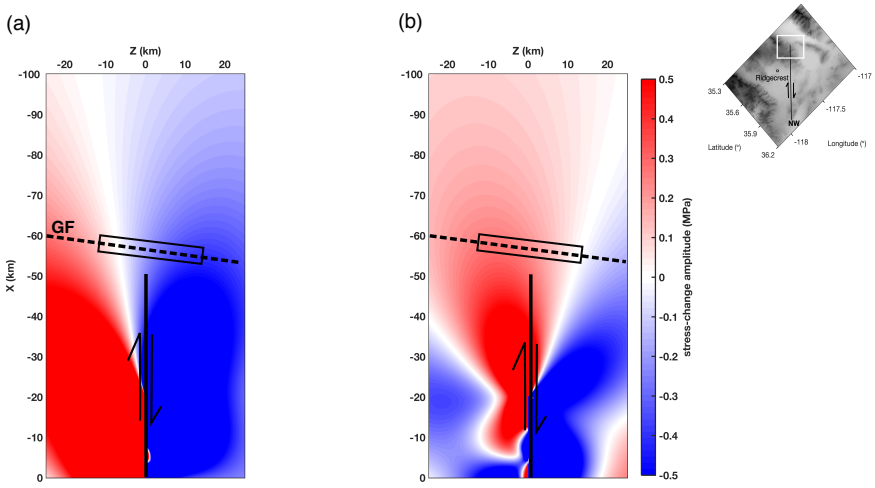

Figure 4.6: Static stress-change field in the modeling domain rotated to the strike of the Garlock fault. (a) Normal stress and (b) shear stress. Garlock fault trace (dashed line) and Ridgecrest mainshock fault (solid line) are superimposed onto the figure. Box denotes approximate location of the creeping region. Inset study area map gives stress- change spatial orientation for Figures 6–8.

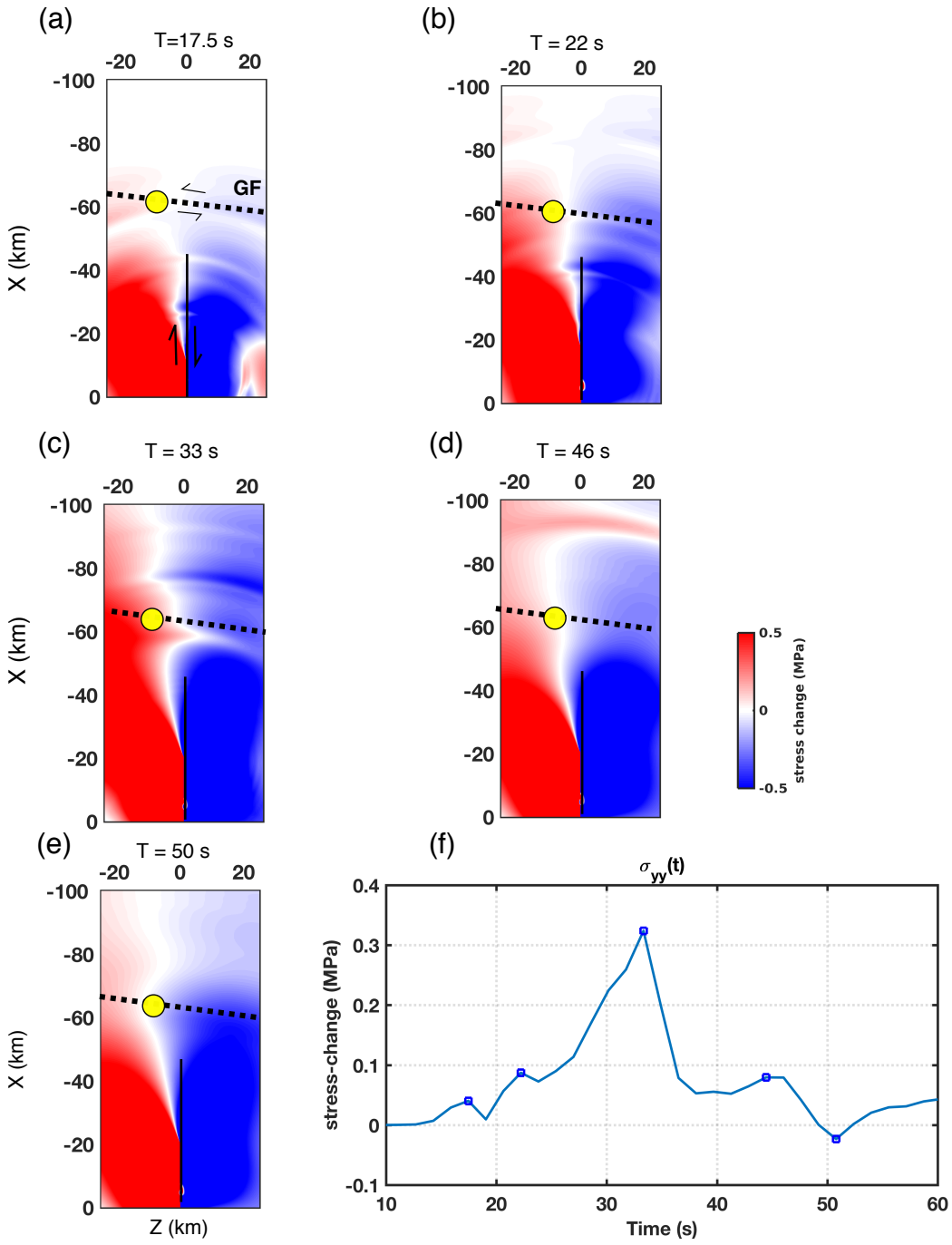

Figure 4.7: Normal stress changes (σ_{yy}) at various moments in time on the central Garlock fault during coseismic rupture of the mainshock. A point on the Garlock is selected to visualize the stress amplitude variability (solid circle). (a–e) represent σ_{yy} from 17.5 to 50 s during rupture propagation. (f) The time history of yy in which (a–e) the blue squares denote the amplitude change at each of the normal stress snapshots.

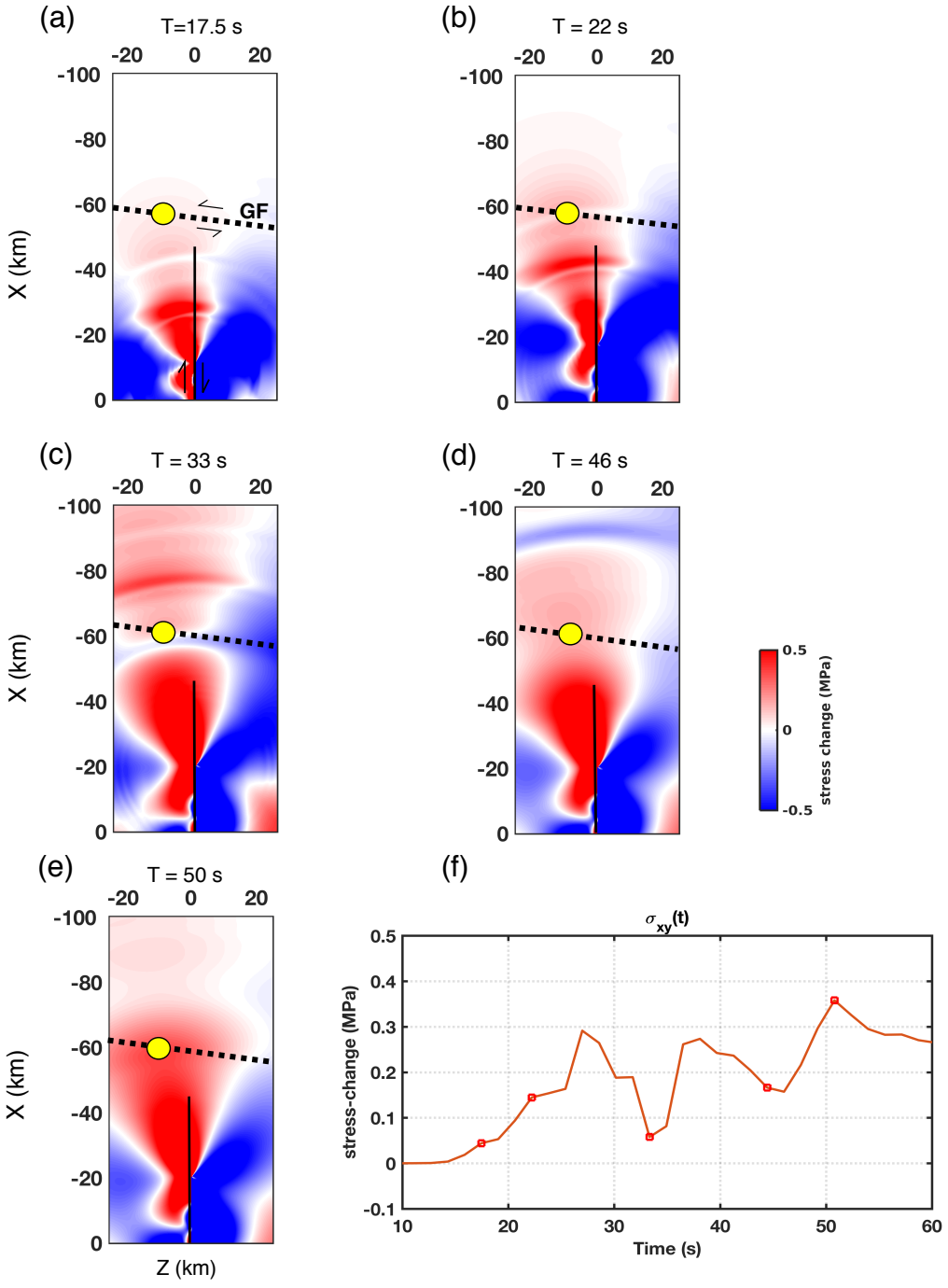

Figure 4.8: Similar to Figure 9, but shear stress changes (σ_{xy}) during coseismic rupture. (a–e) σ_{xy} from 17.5 to 50 s during rupture propagation. (f) The time history of σ_{xy} showing three distinct peaks in stress change on the Garlock fault at ~28, 38, and 50 s.

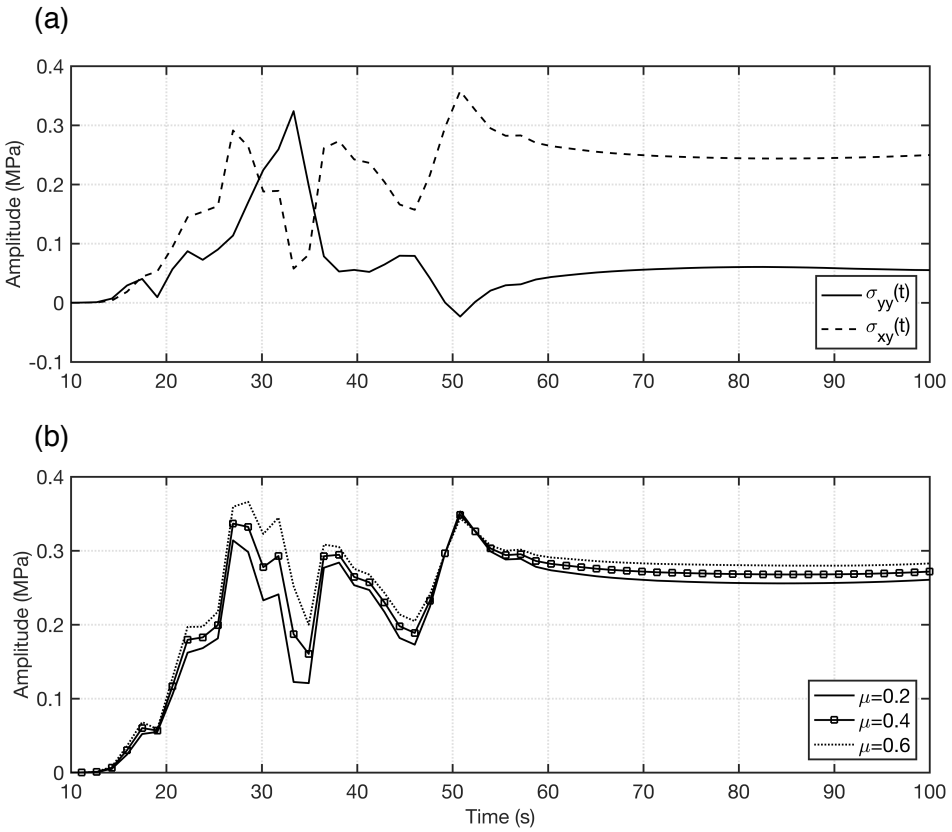

Figure 4.9: Stress-change evolution on a section of the Garlock fault during the entire Ridgecrest earthquake simulation. (a) Normal (σ_{yy}) and shear (σ_{xy}) stress change. (b) Temporal ΔCFS for friction coefficient levels assessed in the static stress-change analysis. Note that we plot the temporal stress change starting at 10 s because this is when the artificial nucleation procedure ceases.

CHAPTER V

Conclusions

Advancing our knowledge of how earthquakes rupture requires both ample geological and geophysical measurements as well as sophisticated numerical techniques that can resolve heterogeneous fault stress and friction distributions. This doctoral dissertation utilized physics-based dynamic rupture simulations to inform earthquake hazard in the Cascadia and in southern California regions.

In Chapters 2 and 3, I constrained potential stress conditions for 2-D and 3-D dynamic rupture simulations using geodetic models along the Cascadia megathrust. In these simulations I also incorporated $\sim$1 MPa effective normal stress amplitudes to represent the inferred weak fault conditions that may enable episodic tremor and slow-slip (ETS) to occur, a constraint that has not been adopted in previous dynamic simulations for subduction megathrusts.

Chapter 2 showed that if an abrupt stress gradient with a negative dynamic stress-drop exists at the base of the locked/transition region of the northern Cascadia megathrust, then a faster (supershear) and deeper down-dip rupture extent can occur. This result is dependent on the assumed frictional behavior in the transition region as well as the relative fault strength in the ETS region. There are large uncertainties on the exact friction levels and accumulated tectonic shear stress for the transition region, but the 2-D dynamic rupture simulations I presented underscore the potential for rupture propagating closer to land. This study also suggested that supershear rupture velocity can be incorporated into kinematic rupture simulations of Cascadia megathrust earthquakes.

Chapter 3 built upon chapter 2 and developed 3-D dynamic rupture simulations for Cascadia that use end-member geodetic coupling models to inform the initial dynamic stress-drop distribution. The geodetic coupling models represent two hypotheses on how the Cascadia megathrust accumulates interseismic strain – one model suggests strong coupling extending to the top of the megathrust while the other model suggests there is pervasive fault creep along-strike (and thus low coupling). This study documented how the relative dynamic stress-drop in the central Cascadia region (inferred to be creeping in both

geodetic coupling models) exerts strong control on the final rupture extent. 3-D dynamic rupture simulations showed that using coastal paleoseismic subsidence data (i.e.,1700 A.D. megathrust event) to uniquely constrain the down-dip coseismic rupture limit is unfeasible: there are multiple down-dip rupture limits and slip distributions that can provide a close fit to these geologic data. This study also found that in order to attain reasonable coseismic subsidence amplitudes ($\sim$1-2 m), there must be an along-strike segmentation in the relative dynamic stress-drop, which is consistent with the multitude of Cascadia literature suggesting segmentation for this subduction zone.

I moved away from the subduction zone setting in Chapter 4 and turned my attention towards a large strike-slip earthquake in the Eastern California Shear Zone (Ridgecrest earthquake sequence). Unlike the previous chapters that relied mostly on geodetic or paleoseismic datasets, chapter 4 leveraged a combination of seismic and geodetic recordings to constrain a 2-D dynamic rupture simulation of the M7.1 Ridgecrest event. I presented a physically consistent framework for assessing elastic stress changes during and after the M7.1 event on the Garlock fault, a major fault immediately south of Ridgecrest. The dynamic simulations were able to reproduce first order kinematic rupture characteristics (e.g., low rupture speed, peak slip distribution) and suggest the temporal changes in normal and shear stress on the Garlock fault were the greatest near the end of rupture. I showed that the largest static and dynamic stress changes on the Garlock fault coincide with a section of the Garlock fault that creeped over nearly 30 km.

5.0.1 Future Research Directions

The work presented here shows that dynamic rupture simulations can be used to address outstanding questions in seismic hazard such as what to expect from future megathrust ruptures given the available interseismic and paleoseismic data (i.e., Chapters 2, 3), or how coseismic rupture influences nearby fault systems (i.e., Chapter 4).

How the details of an earthquake change as rupture propagates up-dip and seismic waves interact with topography or the shallow fault zone structure deserves further scrutiny. Chapters 2 and 3 focused on dynamic controls on along-dip or along-strike rupture propagation, respectively, but a missing element from these studies is a focused treatment of the tsunami hazard. While I am a co-author on a kinematic tsunami simulation study that used coupling models and a handful of dynamic rupture simulations to assess seafloor displacement (i.e., *Salaree*, 2021), both the kinematic tsunami and the dynamic rupture simulations simplified the near-trench structure. Understanding potential dynamic controls (e.g., friction, stress, geometry) on large tsunami generation will be of great help to quantifying

near-field tsunami hazards facing the Pacific Northwest coastline. Previous studies have shown that up-dip rupture propagation and near-trench slip amplitudes are influenced by dynamic wave interactions in the accretionary wedge (e.g., *Kozdon and Dunham*, 2013; *Huang et al.*, 2014), the presumed rheology and material strength of the wedge (e.g., *Ma*, 2012; *Lotto et al.*, 2017), and whether or not shallow rupture will breach the trench (*Wang and He*, 2008). One of the unique aspects about the Cascadia subduction zone is that the trench is entirely buried by sediment that can be, in some locations, almost 2 km thick (e.g., *Han et al.*, 2017). This feature might be relevant to include in future dynamic rupture simulations and motivate a parameter study exploring how accretionary wedge structure, shallow fault stress and fluid pressure levels, or choice of rheology (e.g., off-fault plastic yielding) changes predicted seafloor deformation. But offshore detailed images of wedge structure and its physical properties are greatly needed in Cascadia to make these simulations worthwhile.

Another important condition to consider is how subducted sediment influences megathrust rupture behavior. In accretionary subduction zones, sediment can either accrete to the upper plate or subduct with the lower plate. The subduction zone channel (SC) represents a thick package of subducted sediments that make up the megathrust fault zone (*Shreve and Cloos*, 1986; *Vannucchi et al.*, 2012). SC thickness generally decreases from $\sim$2 - 3 km at the top of the trench to $<$ 1 km in the upper 5 km below the seafloor and is common to many subduction zones (*Vannucchi et al.*, 2012; *Rowe et al.*, 2013). Or, structurally, the SC can be thought of as a layer of anastomosing, active faults that experience focused slip on only a few principal fault surfaces (*Rowe et al.*, 2013). But because the SC is located in a highly consolidated and fluid-rich environment (*Saffer and Tobin*, 2011; *Han et al.*, 2017), these physical conditions could be simply represented in a dynamic rupture simulation with exceptionally low effective normal stress levels in conjunction with a fault friction law that accounts for pore fluid pressurization and heating (*Andrews*, 2002; *Rice*, 2006). The feedback between the SC wave velocity contrast and dynamic weakening due to elevated pore fluid pressure change might contribute greatly to near-trench slip. Explicitly accounting for the SC is one area of future research that could be used to explore, for instance, mechanisms behind 'tsunami-earthquakes' or to anticipate future near-trench rupture characteristics.

Beyond examining the influence of shallow fault zone structure on tsunami hazard, a key output from my 3-D dynamic rupture simulations are kinematic rupture properties (slip, slip-rate, rise-time, rupture duration, peak slip) that can be incorporated into kinematic 3-D rupture simulations (e.g., *Frankel et al.*, 2018) or used to inform novel kinematic and stochastic earthquake source generators for subduction zone earthquakes. Unlike strike-slip fault systems, seismic waves interact differently for dip-slip faults due to interaction

with the earth's surface, modulating the details of rupture propagation (*Ampuero and Ben-Zion*, 2007; *Nielsen*, 1998; *Wang et al.*, 2019). Kinematic rupture properties taken from my dynamic rupture simulations may be used by the strong ground-motion modelling community to show how the interplay of dynamic stresses and friction ultimately control ground shaking in the Pacific Northwest.

BIBLIOGRAPHY

Allen, W. M. B. J. N. G. A. W. R. E., C. R. (1972), Displacements on the imperial, Superstition Hills, and San Andreas faults triggered by the Borrego Mountain earthquake, *U.S. Geological Survey Professional Paper*, *787*, 87–104.

Almeida, R., E. O. Lindsey, K. Bradley, J. Hubbard, R. Mallick, and E. M. Hill (2018), Can the Updip Limit of Frictional Locking on Megathrusts be Detected Geodetically? Quantifying the Effect of Stress Shadows on Near-Trench Coupling, *Geophysical Research Letters*, pp. 1–10, doi:10.1029/2018GL077785.

Ampuero, J.-P., and Y. Ben-Zion (2007), Cracks, pulses and macroscopic asymmetry of dynamic rupture on a bimaterial interface with velocity-weakening friction, *Geophys. J. Int*, *000*, 0–0.

Ampuero, P. (2009), SEM2DPACK: A spectral element method tool for 2D wave propagation and earthquake source dynamics, *User's Guide*, *version 2.3.6*.

Andrews, D. J. (1976), Rupture Propagation With Finite Stress in Antiplane Strain., *Journal of Geophysical Research*, *81*(20), 3575–3582, doi:10.1029/JB081i020p03575.

Andrews, D. J. (1985), Dynamic plane-strain shear rupture with a slip-weakening friction law calculated by a boundary integral method, *Bulletin of the Seismological Society of America*, *75*, 1—21.

Andrews, D. J. (2002), A fault constitutive relation accounting for thermal pressurization of pore fluid, *Journal of Geophysical Research: Solid Earth*, *107*(B12), ESE 15–1–ESE 15–8, doi:10.1029/2002jb001942.

Andrews, D. J. (2010), Ground motion hazard from supershear rupture, *Tectonophysics*, *493*(3-4), 216–221, doi:10.1016/j.tecto.2010.02.003.

Aochi, Hideo, Madariaga, R. (2003), The 1999 Izmit, Turkey, Earthquake: Nonplanar Fault Structure, Dynamic Rupture Process, and Strong Ground Motion, *Bulletin of the Seismological Society of America*, *93*(3), 1249–1266.

Astiz, L., Allen, C. R. (1983), Seismicity of the Garlock fault, California, *Bulletin of the Seismological Society of America*, *73*(6), 1721–1734, doi:10.1017/CBO9781107415324.004.

Atwater, B., and G. Griggs (2012), Deep-sea turbidites as guides to Holocene earthquake history at the Cascadia Subduction Zone—Alternative views for a seismic-hazard workshop, *US Geological Survey Open-File Report*, *1043*, 58.

Atwater, B. F. (1987), Evidence for great Holocene earthquakes along the outer coast of Washington State, *Science*, *236*, 844–942.

Audet, P., M. G. Bostock, N. I. Christensen, and S. M. Peacock (2009), Seismic evidence for overpressured subducted oceanic crust and megathrust fault sealing, *Nature*, *457*(7225), 76–78, doi:10.1038/nature07650.

Barnhart, W. D., G. P. Hayes, and R. D. Gold (2019), The July 2019 Ridgecrest, California, Earthquake Sequence: Kinematics of Slip and Stressing in Cross-Fault Ruptures, *Geophysical Research Letters*, (July), 859–867, doi:10.1029/2019GL084741.

Bartlow, N. M. (2020), A Long-Term View of Episodic Tremor and Slip in Cascadia, *Geophysical Research Letters*, *47*(3), 1–9, doi:10.1029/2019GL085303.

Basset, D., and A. Watts (2015), Gravity anomalies, crustal structure, and seismicity at subduction zones: 2. Interrelationships between fore-arc structure and seismogenic behavior, *Geochemistry Geophysics Geosystems*, *16*(1-2), 1541–1576, doi:10.1002/2014GC005684.Key.

Bilek, S. L., and T. Lay (2018), Subduction zone megathrust earthquakes, *Geosphere*, *14*(4), 1468–1500, doi:10.1130/GES01608.1.

Bilham, R., and B. Castillo (2020), The July 2019 ridgecrest, California, earthquake sequence recorded by creepmeters: Negligible epicentral afterslip and prolonged triggered slip at teleseismic distances, *Seismological Research Letters*, *91*(2 A), 707–720, doi:10.1785/0220190293.

Bletery, Q., A. Thomas, A. W. Rempel, L. Karlstrom, A. Sladen, and L. De Barros (2016), Mega-earthquakes rupture flat megathrusts, *Science*, *356*, 1027–1032.

Bodin, G. J., P. (1994), Triggered seismicity and deformation between the Landers, California, and Little Skull Mountain, Nevada, earthquakes, *Bulletin of the Seismological Society of America*, *84*, 835–843.

Boulton, C., A. R. Niemeijer, C. J. Hollis, J. Townend, M. D. Raven, D. K. Kulhanek, and C. L. Shepherd (2019), Temperature-dependent frictional properties of heterogeneous Hikurangi Subduction Zone input sediments, ODP Site 1124, *Tectonophysics*, *757*(October 2018), 123–139, doi:10.1016/j.tecto.2019.02.006.

Brodsky, E. E., J. J. Mori, L. Anderson, F. M. Chester, M. Conin, E. M. Dunham, N. Eguchi, P. M. Fulton, R. Hino, T. Hirose, M. J. Ikari, T. Ishikawa, T. Jeppson, Y. Kano, J. Kirkpatrick, S. Kodaira, W. Lin, Y. Nakamura, H. S. Rabinowitz, C. Regalla, F. Remitti, C. Rowe, D. M. Saffer, S. Saito, J. Sample, Y. Sanada, H. M. Savage, T. Sun, S. Toczko, K. Ujiie, M. Wolfson-Schwehr, and T. Yang (2020), The

State of Stress on the Fault Before, During, and After a Major Earthquake, *Annual Review of Earth and Planetary Sciences*, *48*(1), annurev–earth–053,018–060,507, doi: 10.1146/annurev-earth-053018-060507.

Brudzinski, M. R., and R. M. Allen (2007), Segmentation in episodic tremor and slip all along Cascadia, *Geology*, *35*(10), 907–910, doi:10.1130/G23740A.1.

Brudzinski, M. R., K. M. Schlanser, N. J. Kelly, C. DeMets, S. P. Grand, B. Marquez-Azua, and E. Cabral-Cano (2016), Tectonic tremor and slow slip along the northwestern section of the Mexico subduction zone, *Earth and Planetary Science Letters*, *454*, 259–271, doi: 10.1016/j.epsl.2016.08.004.

Bruhat, L., and P. Segall (2016), Coupling on the northern Cascadia subduction zone from geodetic measurements and physics-based models, *Journal of Geophysical Research: Solid Earth*, *121*(11), 8297–8314, doi:10.1002/2016JB013267.

Bruhat, L., and P. Segall (2017), Deformation rates in northern Cascadia consistent with slow updip propagation of deep interseismic creep, *Geophysical Journal International Geophys. J. Int*, *211*(December), 427–449, doi:10.1093/gji/ggx317.

Burgette, R. J., R. J. Weldon, and D. A. Schmidt (2009), Interseismic uplift rates for western Oregon and along-strike variation in locking on the Cascadia subduction zone, *Journal of Geophysical Research: Solid Earth*, *114*(1), 1–24, doi:10.1029/2008JB005679.

Byerlee, J. (1978), Friction of Rocks, *Pure and Applied Geophysics*, *116*, 615–626.

Chen, K., J. P. Avouac, S. Aati, C. Milliner, F. Zheng, and C. Shi (2020), Cascading and pulse-like ruptures during the 2019 Ridgecrest earthquakes in the Eastern California Shear Zone, *Nature Communications*, *11*(1), 3–10, doi:10.1038/s41467-019-13750-w.

Chen, X., and J. J. McGuire (2016), Measuring earthquake source parameters in the Mendocino triple junction region using a dense OBS array: Implications for fault strength variations, *Earth and Planetary Science Letters*, *453*, 276–287, doi:10.1016/j.epsl.2016.08.022.

Cochard, A., Madariaga, R. (1996), Complexity of seismicity due to highly rate-dependent friction, *Journal*, *101*(B11), 25,321–25,336.

Cozzens, B. D., and G. A. Spinelli (2012), A wider seismogenic zone at cascadia due to fluid circulation in subducting oceanic crust, *Geology*, *40*(10), 899–902, doi:10.1130/G33019.1.

Das, A. K., S. (1977), A numerical study of two-dimensional spontaneous rupture propagation, *Geophysical Journal ofthe Royal Astronomical Society*, *503*, 643—668.

Daub, E. G., and J. M. Carlson (2010), Friction, fracture, and earthquakes, *Annual Review of Condensed Matter Physics*, *1*, 397–418, doi: 10.1146/annurev-conmatphys-070909-104025.

Davis, B. C. B., G. A. (1973), Garlock fault: An intracon- tinental transform structure, Southern California, *Bulletin of the Geological Society of America*, *84*.

Dawson, T. E., S. F. McGill, and T. K. Rockwell (2003), Irregular recurrence of paleoearthquakes along the central Garlock fault near El Paso Peaks, California, *Journal of Geophysical Research: Solid Earth*, *108*(B7), doi:10.1029/2001jb001744.

Day, S. M. (1982), Three-Dimensional Simulation of Spontaneous Rupture: The Effect of Nonuniform Prestress, *Bulletin of the Seismological Society of America*, *72*(6), 1881–1902.

Day, S. M., L. A. Dalguer, N. Lapusta, and Y. Liu (2005), Comparison of finite difference and boundary integral solutions to three-dimensional spontaneous rupture, *Journal of Geophysical Research: Solid Earth*, *110*(12), 1–23, doi:10.1029/2005JB003813.

De La Puente, J., J. P. Ampuero, and M. Käser (2009), Dynamic rupture modeling on unstructured meshes using a discontinuous Galerkin method, *Journal of Geophysical Research: Solid Earth*, *114*(10), 1–17, doi:10.1029/2008JB006271.

Delorey, A. A., A. D. Frankel, P. Liu, and W. J. Stephenson (2014), Modeling the Effects of Source and Path Heterogeneity on Ground Motions of Great Earthquakes on the Cascadia Subduction Zone Using 3D Simulations, *Bulletin of the Seismological Society of America*, *104*(3), 1430–1446, doi:10.1785/0120130181.

Delph, J. R., A. Levander, and F. Niu (2018), Fluid Controls on the Heterogeneous Seismic Characteristics of the Cascadia Margin, *Geophysical Research Letters*, *45*(20), 11,021–11,029, doi:10.1029/2018GL079518.

Di Toro, G., R. Han, T. Hirose, N. De Paola, S. Nielsen, K. Mizoguchi, F. Ferri, M. Cocco, and T. Shimamoto (2011), Fault lubrication during earthquakes, *Nature*, *471*(7339), 494–499, doi:10.1038/nature09838.

Dragert, W. K. J. T. S., H. (2001), A silent slip event on the deeper Cascadia subduction interface, *Science*, *292*, 1525–1528.

Dunham, E. M. (2007), Conditions governing the occurrence of supershear ruptures under slip-weakening friction, *Journal of Geophysical Research: Solid Earth*, *112*(7), 1–24, doi:10.1029/2006JB004717.

Flueh, F. M. A. B. J. C. J. R. K. D. K. N. e. a., E. R. (1998), New seismic images of the Cascadia sub- duction zone from cruise SO108 — ORWEL, *Tectonophysics*, *293*, 69—94.

Frankel, A., E. Wirth, N. Marafi, J. Vidale, and W. Stephenson (2018), Broadband Synthetic Seismograms for Magnitude 9 Earthquakes on the Cascadia Megathrust Based on 3D Simulations and Stochastic Synthetics, Part 1: Methodology and Overall Results, *Bulletin of the Seismological Society of America*, *108*(5), 2347–2369, doi:10.1785/0120180034.

Galvez, P., J. P. Ampuero, L. A. Dalguer, S. N. Somala, and T. Nissen-Meyer (2014), Dynamic earthquake rupture modelled with an unstructured 3-D spectral element method applied to the 2011 M9 Tohoku earthquake, *Geophysical Journal International*, *198*(2), 1222–1240, doi:10.1093/gji/ggu203.

Gao, H., D. A. Schmidt, and R. J. Weldon (2012), Scaling relationships of source parameters for slow slip events, *Bulletin of the Seismological Society of America*, *102*(1), 352–360, doi:10.1785/0120110096.

Gao, X., and K. Wang (2017), Rheological separation of the megathrust seismogenic zone and episodic tremor and slip, *Nature*, *543*(7645), 416–419, doi:10.1038/nature21389.

Goldberg, D. E., D. Melgar, V. J. Sahakian, A. M. Thomas, X. Xu, B. W. Crowell, and J. Geng (2020), Complex Rupture of an Immature Fault Zone: A Simultaneous Kinematic Model of the 2019 Ridgecrest, CA Earthquakes, *Geophysical Research Letters*, *47*(3), 1–10, doi:10.1029/2019GL086382.

Goldfinger, C., C. H. Nelson, and J. E. Johnson (2003), Holocene Earthquake records from the Cascdia Subduction Zone and Northern San Andreas fault based on precise dating of offshore turbidites, *Annual Review of Earth and Planetary Sciences*, *31*(1), 555–577, doi:10.1146/annurev.earth.31.100901.141246.

Goldfinger, C., H. Nelson, A. Morey, J. E. Johnson, J. R. Patton, E. Karabonov, J. Gutierrez, A. T. Eriksson, G. Eulalia, G. Dunhill, R. J. Enkin, and T. Vallier (2012), Turbidite Event History — Methods and Implications for Holocene Paleoseismicity of the Cascadia Subduction Zone, *USGS Professional Paper*, *1661-F*, 184.

Goldfinger, C., S. Galer, J. Beeson, T. Hamilton, B. Black, C. Romsos, J. Patton, C. H. Nelson, R. Hausmann, and A. Morey (2017), The importance of site selection, sediment supply, and hydrodynamics: A case study of submarine paleoseismology on the northern Cascadia margin, Washington USA, *Marine Geology*, *384*, 4,17,25–16,17,46, doi:10.1016/j.margeo.2016.06.008.

Gomberg, J. (2010), Slow-slip phenomena in Cascadia from 2007 and beyond: A review, *Bulletin of the Geological Society of America*, *122*(7-8), 963–978, doi:10.1130/B30287.1.

Graves, A. B. T. H. K. W. S. L. M. S. J. P. . J. T. H., R. W. (2008), Broadband simulations for Mw 7.8 southern San Andreas earthquakes: Ground motion sensitivity to rupture speed, *Geophysical Research Letters*, *35*.

Gulick, M. A. M. C. S. H., S. P. S. (1998), Seismic structure of the southern Cascadia subduction zone and accretionary prism north of the Mendocino triple junction, *Journal of Geophysical Research*, *103*, 207—227.

Han, S., N. L. Bangs, S. M. Carbotte, D. M. Saffer, and J. C. Gibson (2017), Deformation front sediment consolidation impacts Cascadia megathrust slip and forearc deformation, *Nature Geoscience*, *10*, 954–959, doi:10.1038/s41561-017-0007-2.

Hartzell, S. H., and T. H. Heaton (1983), Inversion of strong ground motion and teleseismic waveform data for the fault rupture history of the 1979 Imperial Valley, California, earthquake, *Bulletin of the Seismological Society of America*, *73*(6), 1553–1583.

Hashima, A., T. W. Becker, A. M. Freed, H. Sato, and D. A. Okaya (2016), Coseismic deformation due to the 2011 Tohoku-oki earthquake: Influence of 3-D elastic structure around Japan 6. Geodesy, *Earth, Planets and Space*, *68*(1), 1–15, doi: 10.1186/s40623-016-0535-9.

Hayes, G. P., G. L. Moore, D. E. Portner, M. Hearne, H. Flamme, M. Furtney, and G. M. Smoczyk (2018), Slab2 - A Comprehensive Subduction Zone Geometry Model, *Science*, (August), 1–10.

Heaton, T.H. Hartzell, S. H. (1987), Earthquake Hazards on the Cascadia Subduction Zone, *Science*, *236*(4798), 162–168, doi:DOI:10.1126/science.236.4798.162.

Heinecke, B. A. R. S. B. M. G. A. A. P. C. B. A. B. W. L. X. V. K. S. M. . D. P., A. (), *IEEE*, *International Conference for High Performance Computing, Networking, Storage and Analysis*, doi:doi.org/10.1109/SC.2014.6.

Hetland, E. A., and M. Simons (2010), Post-seismic and interseismic fault creep II: Transient creep and interseismic stress shadows on megathrusts, *Geophysical Journal International*, *181*(1), 99–112, doi:10.1111/j.1365-246X.2009.04482.x.

Hill, T. W. D., M. L. (1953), San Andreas, Garlock and Big Pine faults, California, *Bulletin of the Geological Society of America*, *64*, 443–458.

Hok, S., E. Fukuyama, and C. Hashimoto (2011), Dynamic rupture scenarios of anticipated Nankai-Tonankai earthquakes, southwest Japan, *Journal of Geophysical Research: Solid Earth*, *116*(12), 1–22, doi:10.1029/2011JB008492.

Holtkamp, S., and M. R. Brudzinski (2010), Determination of slow slip episodes and strain accumulation along the Cascadia margin, *Journal of Geophysical Research: Solid Earth*, *115*(4), 1–21, doi:10.1029/2008JB006058.

Huang, Y., L. Meng, and J. P. Ampuero (2012), A dynamic model of the frequency-dependent rupture process of the 2011 Tohoku-Oki earthquake, *Earth, Planets and Space*, *64*(12), 1061–1066, doi:10.5047/eps.2012.05.011.

Huang, Y., J. P. Ampuero, and H. Kanamori (2014), Slip-Weakening Models of the 2011 Tohoku-Oki Earthquake and Constraints on Stress Drop and Fracture Energy, *Pure and Applied Geophysics*, *171*(10), 2555–2568, doi:10.1007/s00024-013-0718-2.

Hyndman, R. D. (2013), Downdip landward limit of Cascadia great earthquake rupture, *Journal of Geophysical Research: Solid Earth*, *118*(10), 5530–5549, doi:10.1002/jgrb.50390.

Ida, Y. (1972), Cohesive force across the tip of a longitudinal–shear crack and Griffith's specific surface energy, *Journal of Geophysical Research*, *77*, 3796–3805.

Ji, W. D. J. H. D. V., C. (2002), Source description of the 1999 Hector Mine, California earthquake; part I: Wavelet domain inversion theory and resolution analysis, *Bulletin of the Seismological Society of America*, *92*, 1192—1207.

Kame, N., J. R. Rice, and R. Dmowska (2003), Effects of prestress state and rupture velocity on dynamic fault branching, *Journal of Geophysical Research: Solid Earth*, *108*(B5), 1–21, doi:10.1029/2002jb002189.

Kanamori, H., and L. Rivera (2004), Static and dynamic scaling relations for earthquakes and their implications for rupture speed and stress drop, *Bulletin of the Seismological Society of America*, *94*(1), 314–319, doi:10.1785/0120030159.

Kanda, R. V., and M. Simons (2012), Practical implications of the geometrical sensitivity of elastic dislocation models for field geologic surveys, *Tectonophysics*, *560-561*, 94–104, doi:10.1016/j.tecto.2012.06.040.

Kelsey, H. M., R. C. Witter, and E. Hemphill-Haley (2002), Plate-boundary earthquakes and tsunamis of the past 5500 yr, Sixes River estuary, southern Oregon, *Bulletin of the Geological Society of America*, *114*(3), 298–314, doi:10.1130/0016-7606(2002)114⟨0298:PBEATO⟩2.0.CO;2.

Kemp, A. C., N. Cahill, S. E. Engelhart, A. D. Hawkes, and K. Wang (2018), Revising estimates of spatially variable subsidence during the A.D. 1700 cascadia earthquake using a bayesian foraminiferal transfer function, *Bulletin of the Seismological Society of America*, *108*(2), 654–673, doi:10.1785/0120170269.

Kobayashi, A. (2012), Long-term slow slip event around Kochi City from 1977 to 1980, *Journal of the Seismological Society of Japan*, *64*, 63–73.

Kozdon, J. E., and E. M. Dunham (2013), Rupture to the Trench: Dynamic rupture simulations of the 11 march 2011 Tohoku earthquake, *Bulletin of the Seismological Society of America*, *103*(2 B), 1275–1289, doi:10.1785/0120120136.

Krogstad, R. D., D. A. Schmidt, R. J. Weldon, and R. J. Burgette (2016), Constraints on accumulated strain near the ETS zone along Cascadia, *Earth and Planetary Science Letters*, *439*, 109–116, doi:10.1016/j.epsl.2016.01.033.

Lay, T. (2015), The surge of great earthquakes from 2004 to 2014, *Earth and Planetary Science Letters*, *409*, 133–146, doi:10.1016/j.epsl.2014.10.047.

Lay, T., H. Kanamori, C. J. Ammon, K. D. Koper, A. R. Hutko, L. Ye, H. Yue, and T. M. Rushing (2012), Depth-varying rupture properties of subduction zone megathrust faults, *Journal of Geophysical Research: Solid Earth*, doi:10.1029/2011JB009133.

Leonard, L. J., C. A. Currie, S. Mazzotti, and R. D. Hyndman (2010), Rupture area and displacement of past Cascadia great earthquakes from coastal coseismic subsidence, *Bulletin of the Geological Society of America*, *122*(11-12), 2079–2096, doi:10.1130/B30108.1.

Li, D., and Y. Liu (2016), Spatiotemporal evolution of slow slip events in a nonplanar fault model for northern Cascadia subduction zone, *Journal of Geophysical Research: Solid Earth*, *121*(9), 6828–6845, doi:10.1002/2016JB012857.

Li, D., J. J. McGuire, Y. Liu, and J. L. Hardebeck (2018), Stress rotation across the Cascadia megathrust requires a weak subduction plate boundary at seismogenic depths, *Earth and Planetary Science Letters*, *485*, 55–64, doi:10.1016/j.epsl.2018.01.002.

Lienkaemper, G. J. S. S. R. W., J. J. (1997), Creep response of the Hayward fault to stress changes caused by the Loma Prieta earthquake, *Science*, *276*, 2014–2016.

Lin, J. T., K. S. Aslam, A. M. Thomas, and D. Melgar (2020), Overlapping regions of coseismic and transient slow slip on the Hawaiian décollement, *Earth and Planetary Science Letters*, *544*, 116,353, doi:10.1016/j.epsl.2020.116353.

Lin, S. R. S., J. (109), Stress triggering in thrust and subduc- tion earthquakes, and stress interaction between the southern San Andreas and nearby thrust and strike-slip faults, *Journal of Geophysical Research*, *25*, B02,303.

Liu, C., T. Lay, E. E. Brodsky, K. Dascher-Cousineau, and X. Xiong (2019), Coseismic Rupture Process of the Large 2019 Ridgecrest Earthquakes From Joint Inversion of Geodetic and Seismological Observations, *Geophysical Research Letters*, doi: 10.1029/2019GL084949.

Liu, Y., and J. R. Rice (2009), Slow slip predictions based on granite and gabbro friction data compared to GPS measurements in northern Cascadia, *Journal of Geophysical Research: Solid Earth*, *114*(9), 1–19, doi:10.1029/2008JB006142.

Lotto, G. C., E. M. Dunham, T. N. Jeppson, and H. J. Tobin (2017), The effect of compliant prisms on subduction zone earthquakes and tsunamis, *Earth and Planetary Science Letters*, *458*, 213–222, doi:10.1016/j.epsl.2016.10.050.

Lotto, G. C., T. N. Jeppson, and E. M. Dunham (2018), Fully-coupled simulations of megathrust earthquakes and tsunamis in the Japan Trench , Nankai Trough , and Cascadia Subduction Zone, *Pure and Applied Geophysics*, pp. https://doi.org/10.1007/s00,024–018–1990–y Pure, doi:10.1007/s00024-018-1990-y.

Lozos, J. C., and R. A. Harris (2020), Dynamic Rupture Simulations of the M6.4 and M7.1 July 2019 Ridgecrest, California, Earthquakes, *Geophysical Research Letters*, *47*(7), 1–9, doi:10.1029/2019GL086020.

Ma, S. (2012), A self-consistent mechanism for slow dynamic deformation and large tsunami generation for earthquakes in the shallow subduction zone, *Geophysical Research Letters*, *39*(L11310), doi:10.1029/2012GL051,854. 1., doi:10.1029/2012GL051854.

Ma, S., and R. J. Archuleta (2006), Radiated seismic energy based on dynamic rupture models of faulting, *Journal of Geophysical Research: Solid Earth*, *111*(5), 1–17, doi: 10.1029/2005JB004055.

Madariaga, R. and Olsen, K. (2002), Earthquake Dynamics, *International Handbook of Earthquake and Engineering Seismology*, *81A*, 175–194.

Madugo, C. M., J. F. Dolan, and R. D. Hartleb (2012), New paleoearthquake ages from the western Garlock fault: Implications for regional earthquake occurrence in Southern California, *Bulletin of the Seismological Society of America*, *102*(6), 2282–2299, doi: 10.1785/0120110310.

Malatesta, L. C., Bruhat, L., Finnegan, N. J., Olive, J. L. (2021), Colocation of the downdip end of seismic coupling and the continental shelf break, *Journal of Geophysical research : Soild Earth*, *X*, 1–38, doi:10.2307/2609006.

McCaffrey, R., R. W. King, S. J. Payne, and M. Lancaster (2013), Active tectonics of northwestern U.S. inferred from GPS-derived surface velocities, *Journal of Geophysical Research: Solid Earth*, *118*(2), 709–723, doi:10.1029/2012JB009473.

McCrory, P. A., J. L. Blair, F. Waldhauser, and D. H. Oppenheimer (2012), Juan de Fuca slab geometry and its relation to Wadati-Benioff zone seismicity, *Journal of Geophysical Research: Solid Earth*, *117*(9), 1–24, doi:10.1029/2012JB009407.

McGill, K. S., S. F. (2009), Surficial offsets on the central and eastern Garlock fault associated with prehistoric earthquakes, *Journal of Geophysical Research*, *96*.

Melgar, D., R.-J. LeVesque, D. S. Dreger, and R. Allen (2016), Kinematic rupture scenarios and synthetic displacement data: An example application to the Cascadia subduction zone, *Journal of Geophysical research : Soild Earth*, *121*, 6658–6674.

Meng, L., A. Inbal, and J. P. Ampuero (2011), A window into the complexity of the dynamic rupture of the 2011 Mw 9 Tohoku-Oki earthquake, *Geophysical Research Letters*, *38*(16), 1–6, doi:10.1029/2011GL048118.

Nakata, R., N. Suda, and H. Tsuruoka (2008), Non-volcanic tremor resulting from the combined effect of Earth tides and slow slip events, *Nature Geoscience*, *1*(10), 676–678, doi:10.1038/ngeo288.

Newton, T. J., and A. M. Thomas (2020), Stress Orientations in the Nankai Trough Constrained Using Seismic and Aseismic Slip, *Journal of Geophysical Research: Solid Earth*, *125*(7), 1–16, doi:10.1029/2020JB019841.

Nielsen, S. B. (1998), Free surface effects on the propagation of dynamic rupture, *Geophysical Research Letters*, *25*, 125—128.

Noda, H., and N. Lapusta (2013), Stable creeping fault segments can become destructive as a result of dynamic weakening, *Nature*, *493*(518), doi:10.1038/nature11703.

Olsen, K. B., W. J. Stephenson, and A. Geisselmeyer (2008), 3D crustal structure and long-period ground motions from a M9.0 megathrust earthquake in the Pacific Northwest region, *Journal of Seismology*, *12*, 145–159, doi:10.1007/s10950-007-9082-y.

Palmer, . R. J. R., A.C (1973), The growth of slip surfaces in the progressive failure of over-consolidated clay, *Proceedings of the Royal Society of London*, *332*, 527–548.

Pelties, C., J. De La Puente, J. P. Ampuero, G. B. Brietzke, and M. Käser (2012), Three-dimensional dynamic rupture simulation with a high-order discontinuous Galerkin method on unstructured tetrahedral meshes, *Journal of Geophysical Research: Solid Earth*, *117*(2), 1–15, doi:10.1029/2011JB008857.

Pelties, C., A. A. Gabriel, and J. P. Ampuero (2014), Verification of an ADER-DG method for complex dynamic rupture problems, *Geoscientific Model Development*, *7*(3), 847–866, doi:10.5194/gmd-7-847-2014.

Perrin, C., Manighetti, I., Ampuero, J. P., Cappa, F., Gaudemer, Y. (2016), Location of largest earthquake slip and fast rupture controlled by along-strike change in fault structural maturity due to fault growth, *Journal of Geophysical Research: Solid Earth*, *121*, 3782–3803, doi:10.1002/2015JB012608.Received.

Plafker, G. (1972), Alaskan earthquake of 1964 and Chilean earthquake of 1960: Implications for arc tectonics, *Journal of Geophysical Research*, *77*(5), 901, doi:10.1029/JB077i005p00901.

Plafker, G., Savage, J. (1970), Mechanism of the Chilean Eartquakes of May 21 and 22, 1960, *Geological Society of America Bulletin*, *81*, 1001–1030.

Poliakov, A. N. B., R. Dmowska, and J. R. Rice (2002), Dynamic shear rupture interactions with fault bends and off-axis secondary faulting, *Journal of Geophysical Research: Solid Earth*, *107*(B11), ESE 6–1–ESE 6–18, doi:10.1029/2001jb000572.

Priest, G. R., C. Goldfinger, K. Wang, R. C. Witter, Y. Zhang, and A. M. Baptista (2010), Confidence levels for tsunami-inundation limits in northern Oregon inferred from a 10,000-year history of great earthquakes at the Cascadia subduction zone, *Natural Hazards*, *54*(1), 27–73, doi:10.1007/s11069-009-9453-5.

Ramos, M. D., and Y. Huang (2019), How the transition region along the Cascadia megathrust influences coseismic behavior: Insights from 2-D dynamic rupture simulations, *Geophysical Research Letters*, *46*, 1–11, doi:10.1029/2018gl080812.

Ramos, M.D., Neo, J.C., Thakur, P., Huang, Y., Shengji, W. (2020), Stress Changes on the Garlock Fault During and After the 2019 Ridgecrest Earthquake Sequence, *Bulletin of the Seismological Society of America*, *Ridgecrest*, 1–13, doi:10.1785/0120200027.

Reches, Z., and D. A. Lockner (2010), Fault weakening and earthquake instability by powder lubrication, *Nature*, *467*(7314), 452–455, doi:10.1038/nature09348.

Rice, J. R. (1992), Fault Stress States, Pore Pressure Distributions, and the Weakness of the San Andreas Fault, *International Geophysics*, *51*(C), 475–503, doi:10.1016/S0074-6142(08)62835-1.

Rice, J. R. (2006), Heating and weakening of faults during earthquake slip, *Journal of Geophysical Research: Solid Earth*, *111*(B05311), doi:10.1029/2005JB004,006, doi:10.1029/2005JB004006.

Ripperger, J., and P. M. Mai (2004), Fast computation of static stress changes on 2D faults from final slip distributions, *Geophysical Research Letters*, *31*(18), 2–5, doi:10.1029/2004GL020594.

Rodgers, D. H., G. (2003), Episodic tremor and slip on the Cascadia subduction zone: The chatter of silent slip, *Science*, *300*, 1942—1943.

Ross, Z. E., B. Idini, Z. Jia, O. L. Stephenson, M. Zhong, X. Wang, Z. Zhan, M. Simons, E. J. Fielding, S.-h. Yun, E. Hauksson, and A. W. Moore (2019), 2019 Ridgecrest earthquake sequence, *Science*, *3665*(October), 346–351.

Roten, D., K. B. Olsen, and R. Takedatsu (2019), Numerical Simulation of M9 Megathrust Earthquakes in the Cascadia Subduction Zone, *Pure and Applied Geophysics*, doi:10.1007/s00024-018-2085-5.

Rowe, C. D., J. C. Moore, and F. Remitti (2013), The thickness of subduction plate boundary faults from the seafloor into the seismogenic zone, *Geology*, *41*(9), 991–994, doi:10.1130/G34556.1.

Royer, A. A., A. M. Thomas, and M. G. Bostock (2015), Tidal modulation and triggering of low-frequency earthquakes in northern Cascadia, *Journal of Geophysical Research: Solid Earth*, *120*(1), 384–405, doi:10.1002/2014JB011430.

Rubinstein, V. J. G. J. B. P. C. K. C. . M. S., J. L. (2007), Non-volcanic tremor driven by large transient shear stresses, *Nature*, *448*, 579—582.

Saffer, D. M., and H. J. Tobin (2011), Hydrogeology and Mechanics of Subduction Zone Forearcs: Fluid Flow and Pore Pressure, *Annual Review of Earth and Planetary Sciences*, *39*, 157–186, doi:10.1146/annurev-earth-040610-133408.

Salaree, H. Y. R. M. D. . S. S., A. (2021), Cascadia Tsunamis: Should we wait for the Big One?, *in review*.

Satake, K., K. Shimazaki, Y. Tsuji, and K. Ueda (1996), Time and size of a giant earthquake in Cascadia inferred from Japanese tsunami records of January 1700, doi:10.1038/379246a0.

Satake, W. K. A. B., K. (2003), Fault slip and seismic moment of the 1700 Cascadia earthquake inferred from Japanese tsunami descriptions, *Journal of Geophysical Research*, *108*, B11.

Schleicher, H. M. A. K. A. F. J., L. S. (2019), Seismic hazard implications of post-seismic deformation and stress transfer from the 2019 Searles Valley California earthquakes, *2019 Fall AGU Meeting*, *25*, December 9 – 14.

Schmalzle, G. M., R. McCaffrey, and K. C. Creager (2014), Central Cascadia subduction zone creep, *Geochemistry, Geophysics, Geosystems*, *15*(4), 1515–1532, doi:10.1002/2013GC005172.

Scholz, C. H., and J. Campos (2012), The seismic coupling of subduction zones revisited, *Journal of Geophysical Research: Solid Earth*, *117*(5), 1–22, doi:10.1029/2011JB009003.

Segall, P., and A. M. Bradley (2012), Slow-slip evolves into megathrust earthquakes in 2D numerical simulations, *Geophysical Research Letters*, *39*(17), 2–6, doi:10.1029/2012GL052811.

Seyler, C., J. D. Kirkpatrick, T. Hirose, and H. M. Savage (2020), Rupture to the trench? Frictional properties of incoming sediments at the Cascadia subduction zone, *Earth and Planetary Science Letters*, *546*, 116,413, doi:10.1016/j.epsl.2020.116413.

Shreve, R. L., and M. Cloos (1986), Dynamics of sediment subduction, melange formation, and prism accretion, *Journal of Geophysical Research*, *91*(B10), 10,229, doi:10.1029/JB091iB10p10229.

Stephenson, W. J., N. G. Reitman, and S. J. Angster (2017), P- and S-wave velocity models incorporating the Cascadia subduction zone for 3D earthquake ground motion simulations, *USGS Open File Report*, (December), 28, doi:10.3133/ofr20171152.

Stone, I., J. E. Vidale, S. Han, and E. Roland (2018), Catalog of Offshore Seismicity in Cascadia: Insights Into the Regional Distribution of Microseismicity and its Relation to Subduction Processes, *Journal of Geophysical Research: Solid Earth*, doi:10.1002/2017JB014966.

Takagi, R., K. Obara, and T. Maeda (2016), Slow slip event within a gap between tremor and locked zones in the Nankai subduction zone, *Geophysical Research Letters*, *43*(3), 1066–1074, doi:10.1002/2015GL066987.

Thomas, A. L. (1993), Poly3D: A Three-Dimensional, Polygonal Element, Displacement Discontinuity Boundary Element Computer Program with Applications to Fractures, Faults, and Cavities in the Earth's Crust, *Standford University*.

Tinti, E., M. Cocco, E. Fukuyama, and A. Piatanesi (2009), Dependence of slip weakening distance (Dc) on final slip during dynamic rupture of earthquakes, *Geophysical Journal International*, *177*(3), 1205–1220, doi:10.1111/j.1365-246X.2009.04143.x.

Tinti, S., and A. Armigliato (2002), A 2-D hybrid technique to model the effect of topography on coseismic displacements. Application to the Umbria-Marche (central Italy) 1997 earthquake sequence, *Geophysical Journal International*, *150*(2), 542–557, doi:10.1046/j.1365-246X.2002.01721.x.

Toda, S., R. S. Stein, K. Richards-Dinger, and S. B. Bozkurt (2005), Forecasting the evolution of seismicity in southern California: Animations built on earthquake stress

transfer, *Journal of Geophysical Research: Solid Earth*, *110*(5), 1–17, doi:10.1029/2004JB003415.

Trehu, A. I. B. T. M. L. J. H. M. W. D. N. J. L. N. Y., A. M. (1994), Crustal architecture of the Cascadia forearc, *Science*, *266*, 237—243.

Ulrich, T., A. A. Gabriel, J. P. Ampuero, and W. Xu (2019), Dynamic viability of the 2016 Mw 7.8 Kaikōura earthquake cascade on weak crustal faults, *Nature Communications*, *10*(1), doi:10.1038/s41467-019-09125-w.

Ulrich, T., Gabriel, A.A., Madden, E. H. (2020), Stress, rigidity and sediment strength control megathrust earthquake and tsunami dynamics, *under review at Nature Geoscience*, *X*, doi:10.31223/osf.io/s9263/s.

Uphoff, C., S. Rettenberger, M. Bader, E. H. Madden, T. Ulrich, S. Wollherr, and A. A. Gabriel (2017), Extreme scale multi-physics simulations of the tsunamigenic 2004 sumatra megathrust earthquake, *Proceedings of the International Conference for High Performance Computing, Networking, Storage and Analysis, SC 2017*, doi:10.1145/3126908.3126948.

van Rijsingen, E., S. Lallemand, M. Peyret, D. Arcay, A. Heuret, F. Funiciello, and F. Corbi (2018), How Subduction Interface Roughness Influences the Occurrence of Large Interplate Earthquakes, *Geochemistry, Geophysics, Geosystems*, *19*(8), 2342–2370, doi:10.1029/2018GC007618.

Vannucchi, P., F. Sage, J. Phipps Morgan, F. Remitti, and J. Y. Collot (2012), Toward a dynamic concept of the subduction channel at erosive convergent margins with implications for interplate material transfer, *Geochemistry, Geophysics, Geosystems*, *13*(1), 1–24, doi:10.1029/2011GC003846.

Wang, K., and J. He (2008), Effects of frictional behavior and geometry of subduction fault on coseismic seafloor deformation, *Bulletin of the Seismological Society of America*, *98*(2), 571–579, doi:10.1785/0120070097.

Wang, K., and A. M. Tréhu (2016), Invited review paper: Some outstanding issues in the study of great megathrust earthquakes—The Cascadia example, *Journal of Geodynamics*, *98*, 1–18, doi:10.1016/j.jog.2016.03.010.

Wang, K., T. Mulder, C. Rogers, and R. D. Hyndman (1995), Case for very low coupling stress on the Cascadia subduction fault, *Journal of Geophysical Research*, *100*(B7), 12,907–12,918.

Wang, K., R. Wells, S. Mazzotti, R. D. Hyndman, and T. Sagiya (2003), A revised dislocation model of interseismic deformation of the Cascadia subduction zone, *Journal of Geophysical Research: Solid Earth*, doi:10.1029/2001JB001227.

Wang, P. L., S. E. Engelhart, K. Wang, A. D. Hawkes, B. P. Horton, A. R. Nelson, and R. C. Witter (2013), Heterogeneous rupture in the great Cascadia earthquake of 1700 inferred from coastal subsidence estimates, *Journal of Geophysical Research: Solid Earth*, *118*(5), 2460–2473, doi:10.1002/jgrb.50101.

Wang, Y., S. M. Day, and M. A. Denolle (2019), Geometric Controls on Pulse-Like Rupture in a Dynamic Model of the 2015 Gorkha Earthquake, *Journal of Geophysical Research: Solid Earth*, *124*(2), 1544–1568, doi:10.1029/2018JB016602.

Watt, J., and D. S. Brothers (2020), Systematic Characterization of Morpho-Tectonic Variability Along the Cascadia Convergent Margin: Implications for Outer Wedge Dynamics and Shallow Megathrust Behavior, *Geosphere*, *17*(X), 1–23, doi:10.1130/abs/2019cd-329471.

Wech, A. G., and K. C. Creager (2011), A continuum of stress, strength and slip in the Cascadia subduction zone, *Nature Geoscience*, *4*(9), 624–628, doi:10.1038/ngeo1215.

Wells, R. E., R. J. Blakely, Y. Sugiyama, D. W. Scholl, and P. A. Dinterman (2003), Basin-centered asperities in great subduction zone earthquakes: A link between slip, subsidence, and subduction erosion?, *Journal of Geophysical Research*, *108*(B10), doi:10.1029/2002JB002072.

Wells, R. E., R. J. Blakely, A. G. Wech, P. A. McCrory, and A. Michael (2017), Cascadia subduction tremor muted by crustal faults, *Geology*, *45*(6), 515–518, doi:10.1130/G38835.1.

Williams, M. C., A. M. Tréhu, and J. Braunmiller (2011), Seismicity at the Cascadia plate boundary beneath the Oregon continental shelf, *Bulletin of the Seismological Society of America*, *101*(3), 940–950, doi:10.1785/0120100198.

Wirth, E., A. Frankel, N. Marafi, J. Vidale, and W. Stephenson (2018), Broadband Synthetic Seismograms for Magnitude 9 Earthquakes on the Cascadia Megathrust Based on 3D Simulations and Stochastic Synthetics, Part 2: Rupture Parameters and Variability, *Bulletin of the Seismological Society of America*, *108*(5), 2370–2388, doi:10.1785/0120180034.

Wirth, E. A., and A. D. Frankel (2019), Impact of Down-Dip Rupture Limit and High-Stress Drop Subevents on Coseismic Land-Level Change during Cascadia Megathrust Earthquakes, *Bulletin of the Seismological Society of America*, *XX*(Xx), doi:10.1785/0120190043.

Wirth, E. A., A. Grant, N. A. Marafi, and A. D. Frankel (2020), Ensemble ShakeMaps for Magnitude 9 Earthquakes on the Cascadia Subduction Zone, *Seismological Research Letters*, *XX*, 1–13, doi:10.1785/0220200240.Introduction.

Wollherr, S., A.-A. Gabriel, and C. Uphoff (2018), Off-fault plasticity in three-dimensional dynamic rupture simulations using a modal Discontinuous Galerkin method on unstructured meshes: implementation, verification and application, *Geophysical Journal International*, *214*(3), 1556–1584, doi:10.1093/gji/ggy213.

Wollherr, S., A. A. Gabriel, and P. M. Mai (2019), Landers 1992 "Reloaded": Integrative Dynamic Earthquake Rupture Modeling, *Journal of Geophysical Research: Solid Earth*, doi:10.1029/2018JB016355.

Xu, X., D. T. Sandwell, and B. Smith-konter (2020), Coseismic Displacements and Surface Fractures from Sentinel-1 InSAR : 2019 Ridgecrest Earthquakes, *Seismological Research Letters*, doi:10.1785/0220190275.Introduction.

Yang, H., S. Yao, B. He, A. Newman, and H. Weng (2019a), Deriving rupture scenarios from interseismic locking distributions along the subduction megathrust, *Journal of Geophysical Research: Solid Earth*, p. 2019JB017541, doi:10.1029/2019JB017541.

Yang, H., S. Yao, B. He, and A. V. Newman (2019b), Earthquake rupture dependence on hypocentral location along the Nicoya Peninsula subduction megathrust, *Earth and Planetary Science Letters*, *520*, 10–17, doi:10.1016/j.epsl.2019.05.030.

Yang, W., and E. Hauksson (2013), The tectonic crustal stress field and style of faulting along the Pacific North America plate boundary in southern California, *Geophysical Journal International*, *194*(1), 100–117, doi:10.1093/gji/ggt113.

Yao, S., and H. Yang (2020), Rupture Dynamics of the 2012 Nicoya Mw 7.6 Earthquake: Evidence for Low Strength on the Megathrust, *Geophysical Research Letters*, *47*(13), 1–11, doi:10.1029/2020GL087508.

Yousefi, M., G. Milne, S. Li, K. Wang, and A. Bartholet (2020), Constraining Interseismic Deformation of the Cascadia Subduction Zone: New Insights From Estimates of Vertical Land Motion Over Different Timescales, *Journal of Geophysical Research: Solid Earth*, *125*(3), 1–18, doi:10.1029/2019JB018248.

Zhang, Y., X. Zheng, Q. Chen, X. Liu, X. Huang, Y. Yang, and Q. Xu (2020), Automatic Inversion of Rupture Processes of the Foreshock and Mainshock and Correlation of the Seismicity during the 2019 Ridgecrest Earthquake Sequence, *Seismological Research Letters*, *XX*, 1–11, doi:10.1785/0220190343.Supplemental.